Autoignition and flame stabilisation processes in turbulent non-premixed hot coflow flames

Proefschrift

ter verkrijging van de graad van doctor
aan de Technische Universiteit Delft,
op gezag van de Rector Magnificus Prof. ir. K.Ch.A.M. Luyben,
voorzitter van het College voor Promoties,
in het openbaar te verdedigen
op dinsdag 20 maart 2012 om 10.00 uur.

door

Ernst OLDENHOF

civiel ingenieur
geboren te Rotterdam

Dit proefschrift is goedgekeurd door de promotor:
Prof. dr. D.J.E.M Roekaerts

Copromotor: Dr. ir. M.J. Tummers

Samenstelling promotiecommissie:

Rector Magnificus	voorzitter
Prof. dr. D.J.E.M. Roekaerts	Technische Universiteit Delft, promotor
Dr. ir. M.J. Tummers	Technische Universiteit Delft, copromotor
Prof. dr. rer. nat. A. Dreizler	Technische Universität Darmstadt
Prof. dr. H.J.J. Jonker	Technische Universiteit Delft
Prof. dr. ir. T.H. van der Meer	Universiteit Twente
Prof. dr. F. Scarano	Technische Universiteit Delft
Dr. ir. L.M.T. Somers	Technische Universiteit Eindhoven
Prof. dr. ir. C. Kleijn	Technische Universiteit Delft, reservelid

Printed by: Proefschriftmaken.nl || Printyourthesis.com
Published by: Uitgeverij BOXPress, Oisterwijk

ISBN 978-90-8891-397-6

SUMMARY

Autoignition and flame stabilisation processes of turbulent non-premixed hot coflow flames

This dissertation examines stabilisation processes in turbulent non-premixed jet flames, created by injecting gaseous fuel into a co-flowing stream of hot, low-oxygen combustion products. Being able to predict whether and how a flame achieves stable and reliable combustion is a matter of great practical relevance, and a challenging scientific problem. Several theories have been developed to describe the flame stabilisation of conventional non-premixed flames, i.e., flames where cold gaseous fuel is injected in cold air or oxygen. There is however no theory that specifically describes how a non-premixed flame is stabilised when the oxidiser stream is pre-heated, such that autoignition might be a dominant factor in the stabilisation process. A substantial part of this work is devoted to examining how flame stabilisation works under these circumstances and how different parameters impact this process.

The experimental studies that form the basis of this work are carried out on the Delft jet-in-hot-coflow (DJHC) burner. The coflow of this burner is operated at a maximum temperature between approximately 1390 K to 1540 K, and at a typical oxygen mass fraction ranging from 7.6% to 10.9%. This experimental setup was developed with the aim of mimicking some aspects of flameless combustion, a combustion technique that combines high efficiencies with low pollutant emissions. The design of the DJHC burner is based on the Adelaide jet-in-hot-coflow burner, modified to allow for the addition of seeding particles for velocity measurements. The fuels used in the jet are Dutch natural gas and synthetic mixtures that approximate Dutch natural gas.

The first study (Chapter 2) is concerned with the lift-off height of a range of flames, varying in coflow temperature, fuel composition and jet mass flow rate. Diagnostic tools include intensified high-speed imaging, Laser Doppler Anemometry (LDA) and Coherent Anti-Stokes Raman Spectroscopy (CARS). By analysing the statistics of the growth of ignition kernels, conditioned on the moment of their first appearance, the flame stabilisation mechanism is captured. This stabilisation mechanism is very different from that of conventional lifted flames. Instead of an instantaneously sharp interface that propagates against the mean flow, a continuous supply of small autoignition kernels that consequently grow into larger flame pockets is observed. Eventually, these flame pockets merge downstream, such that a steady fuel conversion is assured. The lift-off height can be expressed as a function of three quantities: the axial height at which autoignition events start to occur, the autoignition frequency density and the flame transfer probability. With this division, the different

cases can be compared rigorously. All DJHC flames display an unusual behaviour: the lift-off height initially decreases as a function of the jet velocity. This phenomenon is linked to a decrease in the axial height of first autoignition. The dominance of autoignition in the flame stabilisation process is also expressed by the drastic decrease in lift-off height resulting from the addition of relatively small amounts (in the percent range) of higher alkanes (ethane and propane) to the methane-based fuels. The impact of this addition on conventional lifted flames is significantly smaller.

In Chapter 3, the decreasing lift-off trend as a function of the jet velocity is shown to be caused by the positive radial temperature gradient in the coflow. The increase in entrainment rate when the jet velocity is increased brings the hotter coflow from larger radii inward earlier. The faster mixing of fuel with the hotter coflow leads to earlier autoignition. This chapter also provides more detailed experimental data on several cases from CARS and LDA measurements, and from Planar Laser-induced Fluorescence of the OH radical (OH-PLIF). From the LDA data it is concluded that the velocity field (mean velocity and turbulent stresses) is very comparable between cases with different coflow temperatures, which implies that it is hardly affected by chemical reactions. In DJHC-I flame an increase of the peak temperature is observed between an axial height of 90 mm to 120 mm. Within this distance, the peak temperature increases to a value close to the calculated adiabatic flame temperature. This seems to indicate a slow evolution of the chemistry towards its equilibrium state.

The ignition behaviour of impulsively started jets is studied in Chapter 4. This transient phenomenon is relevant for combustion applications where regenerators are used to feed back heat to the system, thereby improving fuel efficiency. An electronic timing system has been developed to operate the fuel injection system and to couple it to the various measurement systems. This way, the data from the various measurements (LDA, OH-PLIF and time-resolved Particle Image Velocimetry) can be mutually compared, and the sequence that leads to jet instabilities, break-up and eventually ignition can be mapped out. A salient feature is that ignition takes place long after the jet has adopted its steady turbulent state. The injection of virtual Lagrangian particles in the coflow region of the PIV fields clearly visualises that, although the vector field (visualised by streamlines) adapts quickly to the turbulent flow field, the transport process itself (visualised by the particles) needs a time in the order of the integral convective time scale of the coflow. Together with the presence of the radial temperature gradient in the coflow, this introduces a significant ignition delay.

Three different DJHC flames are subjected to a detailed study in Chapter 5, where OH-PLIF and PIV are simultaneously applied to reveal the flow field in the neighbourhood of flame structures. Two different conditioning methods are used: a purely statistical conditioning on the presence or absence of flame structures, and a conditioning on locally introduced coordinate systems. The statistical conditioning shows that the presence of flame structures correlates with the presence of low-turbulence flow. This fact is not to be interpreted as a preference of the reaction zone for low-turbulence regions. Instead,

the conditioning on local coordinate systems shows that the instantaneous velocity field is sharply divided into a turbulent and a non-turbulent part, the division running at the fuel rich side of the flame. This is characteristic for a unity Schmidt number fluid flow: the vorticity (or absence thereof) at the low stoichiometric mixture fraction originates from the quasi-laminar coflow, and not from the turbulent jet. The flame thus resides at a location in the flow which is characterised by strong intermittency.

Chapter 6 discusses two different mechanisms of flame stabilisation that could be encountered in jet-in-hot-coflow flames. Such a flame could be stabilised purely by successive autoignition, flame propagation can however in certain circumstances strongly aid the stabilisation process. The randomness in autoignition is introduced by spatial fluctuations in the temperature field. The central question in the analysis is which circumstances (statistical properties of the temperature field, flame propagation speed) favour which mechanism. Both a stationary, statistically homogeneous space and a convective interface are considered, the latter standing model for the interface of a jet flame. In the stationary space, the criteria that determine which mechanism dominates are the ratio of an autoignition time scale and a flame propagation time scale, and the wideness of the probability density function of the normalised ignition delay time. In other words, when the temperature field fluctuates strongly, over short distances, the flame propagation process will radically shorten the ignition time. The analysis for the convective interface yields a similar result, with the additional conclusion that an abrupt increase in the mean temperature (or an abrupt decrease in the flow time scale) will favour the pure autoignition mechanism. A simplified criterion for autoignition was used to keep the analysis manageable. A more realistic criterion and the inclusion of the effect of fluctuating flow time scales would be necessary to cover the entire range of possible stabilisation mechanisms.

Finally, the effect of a radial gradient in the coflow temperature on the lift-off behaviour is analysed. It is shown that the presence of a positive radial temperature gradient (in circumstances where the temperature is conserved along streamlines in the coflow, that is, a low (turbulent) diffusivity and no thermal radiation), the lift-off height as a function of jet velocity has an initially decreasing, and then increasing trend. This is in line with the experimental findings of Chapter 2.

The data from Chapters 2, 3 and 6 form a comprehensive data set, containing single-point velocity and temperature statistics, statistics on ignition, lift-off and flame propagation and detailed conditional velocity statistics. This allows for rigorous validation of numerical models, not only on the basis of mean quantities, but also on the basis of occurring physical phenomena. It is of great importance that this is done with the specifics of the flames in mind, in particular the strong intermittency of the flow at the mean location of the flame.

SAMENVATTING

Zelfontbrandings- en stabilisatieprocessen van turbulente niet-voorgemengde vlammen in een hete omgevingsstroom

In dit proefschrift worden stabilisatieprocessen van turbulente, niet-voorgemengde straalvlammen in een meestromende warme en zuurstofarme omgeving behandeld. Het kunnen voorspellen of een verbrandingsproces stabiel verloopt is van groot praktisch belang, en daarnaast ook een wetenschappelijk uitdagend probleem. Uiteenlopende theorieën zijn in het verleden ontwikkeld om de vlamstabilisatie van conventionele niet-voorgemengde vlammen (d.w.z. vlammen waarvan zowel de brandstofstroom en de oxidatorstroom niet voorverhit zijn) te beschrijven. Een specifieke theorie voor vlammen met een voorverhitte luchtstroom, dus waarbij zelfontbranding een grote rol zou kunnen spelen, bestaat echter niet. Een belangrijk deel van dit proefschrift is gewijd aan hoe vlamstabilisatie onder zulke omstandigheden plaats kan vinden, en welke parameters van invloed zijn. De experimenten waar op dit werk gebaseerd is zijn uitgevoerd met de "Delft jet-in-hot coflow" (DJHC) brander. De meestromende oxidatorstroom ("coflow") heeft een maximum temperatuur van ongeveer 1390 K tot 1540 K, en een typische zuurstof-massafractie tussen 7.6% en 10.9%. De opstelling is ontwikkeld met het doel om inzicht te krijgen in de interactie tussen turbulentie en chemie in omstandigheden zoals die zich voordoen bij "vlamloze verbranding". Deze verbrandingstechniek combineert hoge efficientie met een geringe uitstoot van schadelijke stoffen. Het ontwerp is gebaseerd op dat van de "Adelaide jet-in-hot coflow" brander, met enkele aanpassingen die het mogelijk maken zogenaamde seedingdeeltjes toe te voegen aan de stroming, om snelheidsmetingen te kunnen uitvoeren. De gebruikte brandstoffen voor de brandstofstraal zijn Nederlands aardgas en mengsels die de compositie van Nederlands aardgas benaderen.

De eerste experimentele studie (Hoofdstuk 2) onderzoekt de hoogte waarop de brandstof begint te reageren (de lift-off hoogte) voor een uitgebreide reeks van vlammen, variërend in coflowtemperatuur, brandstofsamenstelling en massastroom van de brandstofstraal. De diagnostische methoden omvatten lichtversterkte hogesnelheidsopnamen, Laser Doppler Anemometrie (LDA) en Coherente Anti-Stokes Raman Spectroscopie (CARS). Het stabilisatiemechanisme van alle vlammen wordt in kaart gebracht door het analyseren van de ontwikkeling van vlamstructuren, conditioneel op hun eerste verschijnen. Dit mechanisme verschilt sterk van dat waargenomen in conventionele vlammen. In plaats van een scherp gedefinieerde grens tussen het reagerende en niet-reagerende deel van de vlam, worden afzonderlijke zelfontbrandingskernen waargenomen. Deze verschijnen zeer frequent,

en groeien uit tot grotere vlamstructuren die uiteindelijk samensmelten, en zorgen dat op een zekere afstand van het injectiepunt brandstof continu wordt omgezet. De lift-off hoogte kan uitgedrukt worden als functie van drie grootheden: de hoogte waar zelfontbrandingskernen eerst gevormd worden, de frequentiedichtheid waarmee deze gevormd worden, en de waarschijnlijkheid dat een zelfontbrandingskern resulteert in een vlam, op een later tijdstip en een andere plaats. Deze driedeling maakt een gedegen analyse mogelijk. Alle DJHC vlammen worden gekenmerkt door een ongebruikelijke tendens: de lift-off hoogte neemt aanvankelijk af als functie van de snelheid van de jet. Dit fenomeen wordt veroorzaakt door een afname in de hoogte waar zelfontbrandingskernen eerst gevormd worden. Het grote belang van zelfontbranding voor het vlamstabilisatieproces komt ook tot uitdrukking in de sterke afname van de lift-off hoogte door de toevoeging van kleine hoeveelheden hogere alkanen (ethaan en propaan) aan de brandstofstraal. Dit heeft in conventionele vlammen een veel zwakkere invloed.

In Hoofdstuk 3 wordt de dalende lift-off trend nader onderzocht, en wordt aangetoond dat de positieve radiale temperatuurgradient in de coflow de oorzaak is. Het proces waarbij de omringende vloeistof in de turbulente straal wordt opgenomen (de "entrainment") verloopt sneller bij hogere straalsnelheden. Als gevolg hiervan bereikt het warmere deel van de coflow, dat wat meer naar buiten ligt, sneller de turbulente straal om daar te mengen met de brandstof. De snellere inmenging van hetere coflow resulteert in eerdere zelfontbranding. In dit hoofdstuk worden ook gedetailleerde experimentele data besproken voor een aantal vlammen, die het resultaat zijn van CARS, LDA en Planar Laser-induced Fluorescence metingen aan het OH-molecuul (OH-PLIF). Een van de resultaten is dat het snelheidsveld nauwelijks verandert onder invloed van verbranding. In de vlam DJHC-I wordt een toename in de piektemperatuur waargenomen tussen een hoogte van 90 mm en 120 mm, tot een waarde die dicht bij de adiabatische vlamtemperatuur ligt. Dit lijkt te duiden op een langzame ontwikkeling van de chemie naar de evenwichtstoestand.

De ontbranding van impulsief geïnjecteerde brandstofstralen wordt onderzocht in Hoofdstuk 4. Dit probleem is relevant voor verbrandingssystemen waar regeneratoren worden ingezet om de efficiëntie te verhogen. Een elektronisch systeem is ontwikkeld om de tijdstippen relatief tot de injectie in alle ingezette meettechnieken, te weten Particle Image Velocimetry (PIV), LDA, lichtversterkte hogesnelheidsopnamen en OH-PLIF, te verkrijgen. De combinatie van deze meettechnieken levert een compleet beeld op van de achtereenvolgende processen: het instabiel worden van de initieel laminaire straal, het opbreken van de straal tot zijn turbulente staat en uiteindelijk de ontbranding. Een opvallend kenmerk van het proces is dat ontbranding veel later plaats vindt dan het tijdstip waarop de straal zijn stationaire turbulente toestand bereikt. Door het toevoegen van virtuele lagrangiaanse deeltjes aan het coflowgebied in de PIV-velden wordt visueel duidelijk gemaakt, dat het vectorveld zich vrijwel direct aanpast, terwijl het transport van de vloeistof zelf zich aanpast op een tijdschaal in de ordegrootte van de integrale convectie. In combinatie met de aanwezigheid van de temperatuurgradient in de coflow resulteert dit in een significante ontbrandingsvertraging.

Drie verschillende DJHC vlammen worden onderworpen aan een studie op gedetailleerde schaal in Hoodfstuk 5. Gelijktijdige OH-PLIF en PIV metingen zijn hiervoor uitgevoerd, met het doel het snelheidsveld in de buurt van vlamstructuren te onderzoeken. De aldus verkregen data is geconditioneerd op twee verschillende manieren: een tweedeling van de data in het globale assenstelsel op basis van de aan- of afwezigheid van vlamstructuren en een conditionering op lokaal ingevoerde assenstelsels. De eerste methode maakt duidelijk dat de aanwezigheid van vlamstructuren correleert met de aanwezigheid van een laag-turbulente stroming. Dit is geen gevolg van een voorkeur van verbrandingsreacties voor gebieden met een lage turbulentiegraad. Het snelheidsveld is instantaan scherp verdeeld in een turbulent en een niet-turbulent gebied, en de scheidslijn loopt aan de brandstofrijke kant van de vlam. Dit is een mengselfractie-effect: de lage vorticiteit in de buurt van de stoichiometrische mengselfractie heeft zijn oorsprong in de quasi-laminaire coflow, en niet in de turbulente straal. “Intermittency” speelt dus een grote rol in de vlam.

Hoofdstuk 6 behandelt twee verschillende stabilisatiemechanismen die een rol kunnen spelen in vlammen in een hete coflow. Een mogelijkheid is dat vlamstabilisatie uitsluitend het gevolg is van achtereenvolgende zelfontbranding, aan de andere kant kan vlamvoortplanting onder bepaalde omstandigheden het stabilisatieproces sterk versnellen. De statistische willekeurigheid wordt verondersteld veroorzaakt te worden door ruimtelijke fluctuaties in het temperatuursveld. De centrale vraag is welke omstandigheden (statistische eigenschappen van het temperatuursveld, vlamvoortplantingssnelheid) welk mechanisme ten gunste komen. Twee verschillende situaties worden bekeken, te weten een statistisch-homogene ruimte en een convectief grensvlak, dat model staat voor het grensvlak van een straalvlam. In de statistisch-homogene ruimte zijn de criteria die bepalen welk mechanisme het meest van toepassing is, de verhouding van een zelfontbrandingstijdschaal en een vlamvoortplantingstijdschaal en de breedte van de kansdichtheidsfunctie van de genormaliseerde ontbrandingsvertraging. Concreet gezegd, wanneer het temperatuursveld sterk fluctueert over korte afstanden, zal vlamvoortplanting de ontbrandingstijd sterk verkorten. De analyse van het convectieve grensvlak resulteert in een soortgelijk resultaat, met daarnaast de conclusie dat een abrupte toename in de temperatuur (of een afname in de stromingstijdschaal) het pure zelfontbrandingsmechanisme ten gunste komt. Hierbij moet echter opgemerkt worden, dat een sterk vereenvoudigd ontbrandingscriterium gehandhaaft is om de analyse enigszins behapbaar te houden. Een geavanceerder ontbrandingscriterium, en de beschouwing van de invloed van wisselende stromingstijdschalen, is nodig om het hele gebied af te dekken. Een numerieke onderzoeking zou hier zeker behulpzaam zijn. De tweede theoretische analyse in dit hoofdstuk betreft de invloed van een radiale gradient in de coflowtemperatuur. Hierin wordt aangetoond dat de aanwezigheid van een positieve radiale temperatuurgradient (wanneer de temperatuur slechts een weinig verandert langs de stroomlijnen in de coflow) een negatieve relatie tussen de lift-off hoogte en de straalsnelheid teweegbrengt. Dit sluit aan bij de experimentele bevindingen van Hoofdstuk 2.

De data van Hoofdstukken 2, 3 en 6 vormen samen een omvangrijke dataset, van snelheid- en temperatuurstatistieken, statistieken van ontbranding en vlamvoortplantings-

snelheden en details over het conditionele snelheidsveld. Deze data kunnen goed dienen ter validatie van numerieke modellen, niet alleen op basis van gemiddelde grootheden, maar ook op basis van fysische processen. Het is van groot belang dat dit gebeurt met de specifieke eigenschappen van de vlammen in gedachten, met name de sterke "intermittency" van de stroming op de plaats waar de vlamstructuren zich bevinden.

CONTENTS

Summary **iii**

Samenvatting **vii**

1 Introduction **1**
1.1 Energy in the 21st century . . . 1
1.2 Flameless combustion . . . 2
1.3 The DJHC setup . . . 3
1.4 Flame stabilisation . . . 4
1.5 Laboratory-scale flames and model validation . . . 5
1.6 Outline of this thesis . . . 6

2 Ignition kernel formation and lift-off behaviour **9**
2.1 Introduction . . . 9
2.2 Experimental setup . . . 11
2.2.1 DJHC burner . . . 11
2.2.2 Case description . . . 12
2.2.3 Optical setup and image processing . . . 13
2.2.4 LDA system . . . 14
2.2.5 CARS system . . . 14
2.3 Results and discussion . . . 14
2.3.1 Details of the coflow . . . 14
2.3.2 Visual observations . . . 16
2.3.3 Definition of lift-off height . . . 18
2.3.4 Axial location of first occurrence of autoignition kernels . . . 23
2.3.5 Transport of flame pockets . . . 24
2.3.6 Flame transfer probability . . . 27
2.3.7 Ignition frequencies . . . 30
2.3.8 Evaluation and implications on lift-off height . . . 33
2.4 Conclusions . . . 34

3 Role of entrainment in the flame stabilisation **37**
3.1 Introduction . . . 37
3.2 Experimental setup . . . 39
3.2.1 DJHC-burner . . . 39
3.2.2 LDA system . . . 39
3.2.3 CARS system . . . 40
3.2.4 OH-PLIF imaging system . . . 41

3.2.5 Flue gas measurements . . . 41
3.3 Case Description . . . 42
3.4 Visual and OH-LIF observations . . . 46
3.5 Flow field . . . 49
3.5.1 Mean velocities and Reynolds stresses . . . 49
3.5.2 Turbulence length scales . . . 51
3.6 Temperature field . . . 53
3.7 Entrainment . . . 57
3.8 Conclusions . . . 61

4 Ignition of impulsively started fuel jets 63
4.1 Introduction . . . 63
4.2 Experimental setup . . . 65
4.2.1 Burner and fuel injection mechanism . . . 65
4.2.2 Solenoid controller and counter . . . 65
4.2.3 Laser Doppler anemometry . . . 66
4.2.4 CARS temperature measurements . . . 66
4.2.5 Particle image velocimetry . . . 67
4.2.6 Planar laser-induced OH fluorescence . . . 68
4.2.7 Simultaneous PIV and OH-PLIF measurements . . . 68
4.2.8 Case description . . . 69
4.3 The velocity field . . . 71
4.3.1 Axial velocity at the jet exit . . . 71
4.3.2 Development of the jet . . . 73
4.4 Ignition sequence . . . 76
4.5 Transition to turbulent entrainment . . . 80
4.6 Conclusions . . . 83

5 Conditional flow field statistics 85
5.1 Introduction . . . 85
5.2 Experimental setup . . . 86
5.2.1 DJHC burner . . . 86
5.2.2 Case description . . . 87
5.2.3 PIV system and data processing . . . 90
5.2.4 OH-PLIF system and data processing . . . 92
5.3 Flowfield and length scales . . . 92
5.3.1 Velocity profiles . . . 92
5.3.2 Length scales . . . 93
5.4 Conditional velocity statistics . . . 96
5.4.1 OH-PLIF signal strength as flame indicator . . . 96
5.4.2 Visual and OH-PLIF observations . . . 97

5.4.3 Conditional and unconditional flow field . . . 99
5.5 Conditioned velocity field . . . 100
5.5.1 Methodology . . . 100
5.5.2 Interface statistics . . . 103
5.5.3 Local velocities . . . 104
5.5.4 Vorticity and enstrophy . . . 104
5.5.5 Strain rates . . . 105
5.5.6 Evaluation and discussion of the results . . . 109
5.6 Implication for scaled flameless combustion experiments . . . 111
5.7 Conclusions . . . 112

6 Stabilisation mechanisms of non-premixed, autoigniting flames 115
6.1 Autoignition and flame propagation . . . 115
6.1.1 Autoignition delay time statistics . . . 115
6.1.2 Ignition in a space with a fluctuating initial temperature field . . . 116
6.1.3 Ignition on a convective interface . . . 119
6.2 The effect of a mean temperature gradient in the coflow . . . 125
6.2.1 Evaluation of lift-off height trends . . . 129

7 Conclusions and recommendations 131
7.1 Conclusions . . . 131
7.1.1 Characteristics of the studied flames . . . 131
7.1.2 Insights of general interest . . . 133
7.1.3 A reflection on laboratory-scale flameless combustion setups for model validation . . . 133
7.2 Recommendations . . . 134

A Corrected jet Reynolds numbers 137

B Density weighted nature of transit-time corrected LDA data 139

C Probability that a random variable exceeds a value within an interval 141

Bibliography 143

Dankwoord 153

List of Journal Publications 155

About the author 156

CHAPTER 1

Introduction

1.1 Energy in the 21st century

This century, mankind will find itself confronted with a formidable challenge. While the world population continues to grow, with a growing fraction of this population participating in the energy-intensive modern standard of living, fossil fuel supplies will become more and more scarce.

For a long time, the readily available supplies of fossil fuel have enabled a growth of exponential nature. In the last century, the world population has increased fourfold and the average life expectancy doubled while in the same period, the per capita gross domestic product increased sevenfold in Western Europe [1].

Until halfway into the twentieth century, coal was the dominant fossil energy source. In the 1950's, the share of petroleum in the total U.S. energy supply first exceeded that of coal, whereas natural gas energy consumption equalled that of coal several years later [2]. Despite the advent of nuclear energy and renewables, fossil fuels are still by far the dominant energy source. It is estimated that in 2007 coal, petroleum and natural gas together amounted for 85% of the world's energy consumption, of which petroleum constitutes the largest share [3].

As huge as natural reserves of fossil fuels may be, they are not endless. It is estimated that "conventional" petroleum reserves will be depleted in the 2040's, whereas coal reserves are expected to last for at least a century [4, 5]. In this projection, a steady demand growth rate is taken into account. Note that not doing so will result in much longer, but unrealistic, depletion times [6]. The size and profitability of "unconventional" fossil fuel reserves is a complex topic. Harvesting unconventional sources (shale gas, tar sands) is at any rate a short-term solution, and substantially more energy intensive than conventional mining. From an economic standpoint alone it is therefore desirable to develop sustainable energy sources on a serious scale, sooner rather than later.

There are other motives for developing sustainable energy. The contribution of CO_2 ("carbonic acid", in the name convention of that time) in the atmosphere to the earth's greenhouse effect was first quantified by Arrhenius in 1896 [7]. The idea that the increase in CO_2 levels due to human activities could lead to a significant increase in radiative forcing and thus in global surface temperature was put forward in 1979 [8]. A doubling in atmospheric CO_2 levels was estimated to lead to an increase of 3 °C. Almost thirty years later, the 2007 IPCC report states that "Warming of the climate system is unequivocal" and that "Most of the observed increase in global average temperatures since the mid-20th

century is very likely due to the observed increase in anthropogenic greenhouse gas concentrations" [9]. In other words, global warming is occurring, and is for the largest part caused by human activity. The energy sector (i.e., the burning of fossil fuels) represents a very large share of total human greenhouse emissions, at an estimated 81% in developed countries [10].

The efforts it would take to transform an industrialised country from being fossil fuel-based to being sustainable in its energy supply are not to be underestimated. As calculated by MacKay [6], to achieve a sustainable energy production on the level of the typical current Western energy consumption (for the U.K. this is estimated at 125 kWh per day per person), will require devoting very large areas ("country-sized") of land and water to wind energy, solar energy, biofuels and other renewable sources. It would therefore be wise to use the resources of fossil fuels economically, as long as energy demands cannot yet be fulfilled by renewables alone. This requires the development and implementation of more efficient combustion techniques that convert fuel to useful heat and/or work.

1.2 Flameless combustion

A straightforward method to achieve higher efficiencies in combustion systems is to feed back heat to the system that would otherwise have been lost to the environment. This can be achieved by adding heat exchangers that transfer heat from the flue gas stream to the fresh air stream. A notable combustion technique in which heat regeneration helps to achieve higher efficiencies is flameless combustion. Flameless combustion has a very wide field of application, ranging from steel and glass furnaces to gas turbines, hydrogen reformers and cogeneration [11, 12]. A major difference with conventional combustion is that the (preheated) air and fuel streams do not react directly with each other, but first mix in with reaction products. This is achieved by forcing a strong recirculation inside the furnace. The resulting flame is not strongly luminous and hardly visible, hence the name "flameless". The single most important property of flameless combustion is that high peaks in temperature (both temporal and spatial) are absent. Thus, the increased efficiency due to preheating of (one or both) reactants does not come with the penalty of an increase in NO_x emission [11, 13].

The absence of spatial and temporal peaks in temperature is attributed to the strong mixing of the reactants and products before reaction sets in. That stronger mixing leads to lower peak temperatures is not a trivial consequence. It even seems to be contradictory with the more diffuse reaction zones as observed in flameless combustion [14, 15], since the low gradients (low scalar dissipation rate) should result in chemistry that is close to equilibrium. The low oxygen content is often made central to the analysis [16], but oxygen content alone does not determine the equilibrium temperature. The enthalpy loss of the oxidant stream forms the most basic explanation for the low combustion temperatures. The strong recirculation brings a large mass flow of cooled-down products back, and thereby lowers the enthalpy of the reactants at stoichiometry, reducing the equilibrium temperature. Of

course, the lower the oxygen content, the more enthalpy loss the products can carry. This explanation does not require taking into account reaction kinetics. Reaction kinetics are however also mentioned as a cause for lower temperatures, along with enhanced radiative losses at the reaction zone due to high CO_2 and H_2O contents [17].

Although flameless combustion has outgrown the research stage, and already has a large number of real-life applications, there is a potential for more widespread implementation of this and other efficiency-increasing techniques. Numerical predictions enable a-priori analyses of different designs and help to avoid the risk of building facilities that do not work as envisaged. Therefore, the capability of computer models to predict the performance of a new technology correctly is important if it is to be adopted in favour of a proven, existing technology.

Combustion models that have proven their value in conventional furnaces, will not necessarily work well for flameless combustion since the characteristics of the combustion process are very different. For instance, whereas flame stabilisation is determined by flame propagation when reactants are injected at low temperature, it could be governed by autoignition when one of the reactants is preheated. Furthermore, chemistry time scales are expected to be larger compared to flow time scales, potentially leading to an entirely different combustion regime. To develop models that can deal with the specifics of flameless combustion, accurate experimental data and physical insights on the relevant phenomena are needed.

1.3 The DJHC setup

Measurement techniques that provide the detail that is needed to investigate combustion processes on a fundamental level generally require laser-optical access, which is not provided by large industrial devices. Open laboratory scale experiments, such as Delft jet-in-hot-coflow (DJHC) burner, on the other hand allow full access for laser-optical techniques. The DJHC setup is relatively small (coflow diameter 0.09 m, typical power consumption $\sim$ 20 kW) and features a central fuel jet (inner diameter 4.5 mm) that enters an oxidant stream with a high temperature (with a maximum temperature between 1390 K and 1540 K) and a low oxygen mass fraction (typically between 7.6% and 10.9%). The oxidant stream is generated by an internal, secondary burner. Due to radiative and convective heat transport, the coflow has lost a substantial amount of sensible enthalpy to the surroundings before it mixes with the fuel stream. Thus, an autoigniting jet flame with low peak temperatures is generated. However, when compared to the design of for instance the FLOX® [18] burner of WS Wärmeprozesstechnik GmbH, there are crucial differences. The FLOX® burner has high-momentum, preheated air jets surrounding the central fuel jet. Additional processes therefore take place in realistic burners, processes that may be very significant. For this reason, the DJHC burner should be viewed as a generic test case of a turbulent non-premixed jet flame in preheated surroundings, rather than a model version of a realistic setup. It fits in a family of hot coflow burners, some of which are discussed here briefly.

The Adelaide jet-in-hot-coflow burner [19] predates the DJHC burner, in fact, it formed the basis of the design for the DJHC burner. Many of its features where adopted, although the secondary burner of the DJHC is constructed differently so as to allow seeding particles to be added to the flow for velocity measurements. On the other hand, the Adelaide burner can operate at lower oxygen levels in the coflow (with a mass fraction as low as 3%).

The Cabra burner [20] has a large diameter (0.21 m) coflow generated by 2200 premixed jet flames. With this design, a very homogeneous temperature field is achieved. It is typically operated at somewhat higher oxygen levels, with an oxygen mole fraction of around 12% to 15% (oxygen mass fractions from 15.6% to 18.5%) and at high jet Reynolds numbers, 25,000 or more.

The CHTC setup at Cambridge [21] was explicitly designed to study autoignition processes. The oxidiser stream consists of electrically heated air, with temperatures between 800 K and 1000 K. A marked difference with all previously mentioned setups is that the jet velocity is of equal magnitude as the coflow stream velocity, at 10-30 m/s. The mixing region is thus not affected by a strong mean shear as in the other cases.

1.4 Flame stabilisation

Many research papers and practical combustion books are devoted to the subject of flame stabilisation. In a conventional combustion system where reactants are injected at a relatively low temperature, and the heat of combustion is relatively large, two distinctly different solutions exist: a nearly frozen state (almost no fuel conversion) and a reacting state (almost complete fuel conversion). Which one of these solutions the system adopts, depends not just on its parameters, but also on its history, for instance, whether the system was ignited or not. The system is thus subject to a strong hysteresis. The ignition and extinction behaviour, and the multiplicity of solutions, is described by the classical "S-curve" ([22], pg. 314). For a practical combustion facility, flame stabilisation thus means ensuring that the system exists only in the upper, reacting branch. For large reactant inlet speeds, this can be achieved by the addition of pilot flames, the creation of recirculation zones or by strongly preheating one of the reactants to ensure autoignition ([23], pg. 291). In laboratory combustion setups, the word flame stabilisation is used mainly in connection with the lift-off height, which in conventional flames is a sharply defined region in space where fuel conversion begins.

At high preheat temperatures and strong reactant dilution (resulting in a relatively low difference in temperature of the frozen and the reacting state), the usually folded S-curve stretches, which leads to the disappearance of the turning points and of the two different branches [22, 24]. In this case, combustion will be inherently stable and complete when residence times are sufficiently long [11]. Flame stabilisation in flameless combustion setups is thus distinctly different from that in a conventional combustion system.

As will be shown in Chapter 2, the flame stabilisation of the DJHC flames is also different from that of conventional lifted non-premixed flames. In contrast to these flames,

there is no sharply defined lift-off height. Nevertheless, the distinction between reacting and non-reacting fluid can be made instantaneously using (laser-)optical techniques. For the DJHC burner, flame stabilisation processes are defined as those processes, that assure that at a certain distance the conversion from reactants to products takes place continuously.

1.5 Laboratory-scale flames and model validation

A common approach in modern-day combustion research is to do both experimental and numerical studies on a single setup. An advantage of this approach is that both techniques offer different perspectives, which aids in gaining understanding of the system. Another reason for doing so is that the experimental data can be used for the development and validation of mathematical (sub-) models.

The efforts to develop more accurate models stem from the desire to be able to design and optimise systems such as turbine engines, internal engines or furnaces with computer calculations. Studying many different configurations experimentally is costly and time intensive, whereas calculations can be done quickly and relatively cheaply. Of course, numerical studies only make sense if numerical predictions can reproduce reality. This is notoriously difficult when turbulence is involved.

The wide range of time- and length scales found in turbulence forbids a direct numerical solution of realistic systems (with Reynolds numbers exceeding ten to the power of five or so), as the computational effort is simply too big, even for modern supercomputers. Therefore, one typically tries to solve only for some mean quantities, which is the so-called RANS (Reynolds-averaged Navier Stokes) approach. In recent years Large Eddy Simulation (LES), providing a transient simulation of the large scales of the flow, while mode ling the small scales, has become an affordable alternative for RANS. Both approaches always involve introducing empirical closures for higher-order statistics.

When chemical reactions are added, the picture becomes even more complex. Fluctuating species concentrations and temperatures all enter the strongly non-linear Arrhenius equations, and a moment-based approach is not viable [23]. Turbulence therefore frustrates the calculation of mean source terms in a RANS approach, as the needed information on the simultaneous presence of species and the temperature level (the joint probability density function, or pdf) is not available when only mean quantities are solved for. In a combusting flow, the chemistry influences the flow actively through the density of the mixture, which in ideal gases has an inverse relation with temperature. It can thus be stated that understanding the *turbulence-chemistry interaction* in flames is a huge scientific challenge which deserves dedicated investigation.

To decouple this interaction as much as possible from other complications (for instance, geometry-specific flow phenomena, radiation, buoyancy effects) and to be able to study the flow in detail, research is often conducted on laboratory setups. These are typically open (and therefore optically accessible), of small scale (thereby easily probed), and have a simple geometry. Model development or optimisation is then done based on experimental

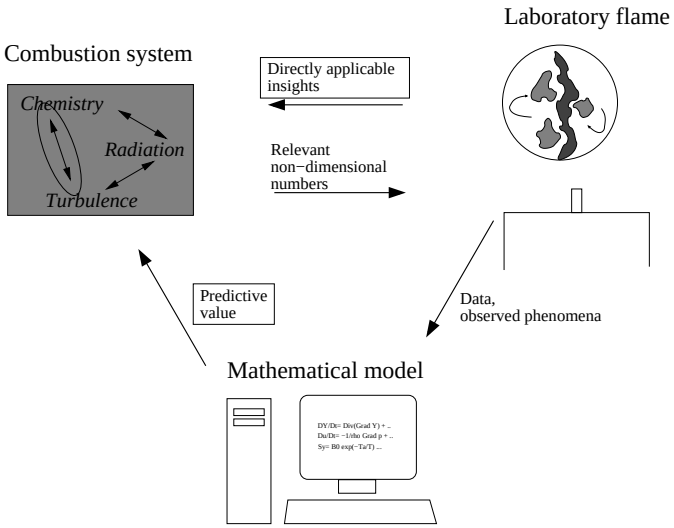

Figure 1.1: Model validation and development through the use of laboratory combustion setups

results of a laboratory setup, with improved modelling capabilities for realistic, industrial cases in mind.

The situation is outlined in Fig. 1.1. The industrial combustion system, shown in the upper left corner, is the actual subject of the study. As its size, optical inaccessibility and additional complexities prohibit detailed investigation, a laboratory flame is examined instead. Phenomena are observed and quantities are measured, based on which mathematical models are tested and/or developed. The boxed text shows the "deliverables" of the entire process. These are the improved predictive value of the numerical model, and possibly some insights that can be directly applied. The improved predictive value could be realised by fine tuning of a parameter, or the inclusion of a new term or submodel to account for an observed process.

To actually achieve the desired model performance for an industrial-scaled device, two requirements need to be met. Firstly, the laboratory setup has to be representative for some aspect of the industrial device. This means that some selected non-dimensional quantities, relevant to the process intended to be studied, have to match. Secondly, the model validation or optimisation has to be performed with a critical eye, paying attention to the physical processes that are relevant. A discussion on this topic is provided at the end of Chapter 5 and in Section 7.1.3.

1.6 Outline of this thesis

This thesis is for a large part (Chapters 2 to 5) a compilation of published or submitted papers. Subjects such as the experimental and measurement setups are therefore addressed

more than once, albeit briefly. For this reason, they are not treated in a separate chapter. For a detailed description of the measurement setup, the reader is advised to consult sections 2.2.1 and 3.2.1. For an overview of the boundary conditions of most of the studied cases, the reader is referred to section 3.3.

In Chapter 2, the processes underlying flame stabilisation are discussed, and a model is introduced that describes the flame stabilisation, combining autoignition and flame propagation. In Chapter 3, the entrainment of coflow fluid is investigated, and how it –together with the radial temperature gradient of the coflow– influences the lift-off height. It thereby offers an explanation for the remarkable result from the previous chapter, namely that the lift-off height *decreases* when the jet velocity is increased. Chapter 4 describes the ignition sequence of an abruptly started fuel jet in the DJHC burner, that is shown to be largely dependent on a time scale associated with large-scale transport. In Chapter 5, conditional statistics of the DJHC flames are detailed. Here, an important characteristic of the DJHC burner is revealed which might severely limit the applicability of this setup (and possibly several other setups) to industrial cases. In Chapter 6, two different modes of flame stabilisation by autoignition (i.e., purely autoignition, or flame propagation originating from autoignition events) are studied theoretically. Furthermore, a simplified model is introduced that explains the unconventional lift-off trends from Chapter 2 by accounting for changes in the autoignition time scale due to entrainment of an inhomogeneous surroundings. Chapter 7 ends with conclusions and recommendations for future research(ers).

CHAPTER 2

Ignition kernel formation and lift-off behaviour

The stabilisation region of turbulent non-premixed flames of natural gas mixtures burning in a hot and diluted coflow is studied by recording the flame luminescence with an intensified high-speed camera. The flame base is found to behave fundamentally differently from that of a conventional lifted jet flame in a cold air coflow. Whereas the latter flame has a sharp interface that moves up and down, ignition kernels are continuously being formed in the jet-in-hot-coflow flames, growing in size while being convected downstream. To study the lift-off height effectively given these highly variable flame structures, a new definition of lift-off height is introduced. An important parameter determining lift-off height is the mean ignition frequency density in the flame stabilisation region. An increase in coflow temperature and the addition of small quantities of higher alkanes both increase ignition frequencies, and decrease the distance between the jet exit and the location where the first ignition kernels appear. Both mechanisms lower the lift-off height. An increase in jet Reynolds number initially leads to a significant decrease of the location where ignition first occurs. Higher jet Reynolds numbers (above 5000) do not strongly alter the location of first ignition but hamper the growth of flame pockets and reduce ignition frequencies in flames with lower coflow temperatures, leading to larger lift-off heights.

2.1 Introduction

Turbulent non-premixed jet flames burning in a hot oxidiser stream containing combustion products (jet-in-hot-coflow flames) are relevant to clean combustion techniques such as Flameless Combustion, High-Temperature Air Combustion (HiTAC), Excess Enthalpy Combustion and Mild Combustion [11, 13, 25]. These techniques are strongly related in the sense that they all recover exhaust gas heat (for instance using regenerators or recuperators) and rely on high recirculation ratios to ensure proper mixing of one or both reactant streams with the flue gases (carrying an enthalpy deficit) before any reaction takes place. The benefits of these combustion techniques are the inherent flame stabilisation due to the high oxidiser temperature and the flat temperature profiles void of peaks, leading to low NO_x emissions. Furthermore, efficiencies are high due to the exhaust gas heat recovery.

Published in *Combust. Flame* 157(6):1167-1178, June 2010.

The industrial and environmental relevance, combined with the scientific challenge of modelling these flames is the reason for the amount of attention this type of combustion has recently received in both detailed experimental [20, 19, 26, 27, 28] and numerical [29, 30, 31, 32, 33, 34] studies on laboratory-scale setups.

An important parameter in turbulent non-premixed flames is the lift-off height. In conventional jet flames, the lift-off height, or flame stabilisation point, is the average axial height of the sharp flame interface. For jet-in-hot-coflow flames, different criteria to determine lift-off height are found in literature. Usually, a certain threshold level for an averaged quantity is defined, for instance temperature [35], OH concentration [20, 36] or luminescence [37]. As gradients of average quantities in jet-in-hot-coflow flames are generally weak, specific choices of their threshold values can have great impact on the resulting value for the lift-off height. Moreover, determining the lift-off height from time-averaged fields does not reflect the complex dynamics of the lifted flame.

Several theories have been developed to explain the physical mechanisms governing lift-off for turbulent jet flames. An extensive review by Lyons [38] divides these theories and concepts in five different groups. Summarising, several theories rely on an equilibrium between flame speed and flow velocity, the flame speed being that of a laminar [39] or a turbulent [40] premixed flame, or that of a more complex 2-D flame structure [41], while other theories emphasise the competition between chemical and flow time scales [42], or the role of large-scale flow structures in transporting flame leading-edges [43]. This list does not include any theory that is specific to flameless combustion. In the recent study of lift-off heights that specifically included flameless combustion [35], a generic model relating flow and chemistry time scales was used. However, it has been pointed out in several studies [26, 28, 21, 44] that the physics of jet-in-hot-coflow flames is rather different from that of a conventional lifted jet flame. For example, Gordon et al. [28] showed by means of joint temperature, OH and CH_2O imaging the distinctly different stages of flame formation in methane jet flames in a vitiated coflow. The identified sequence started with the formation of CH_2O-rich regions, followed by the formation of small (sub-millimeter) OH-rich kernels that grow in size, rise in temperature and eventually lead to flame structures. The presence of ignition kernels has been demonstrated in other experiments, for instance in [21]. In the recent review by Mastorakos [45] an overview is given of both numerical and experimental work in the field of autoigniting flames. The combined role of chemistry and turbulence is discussed, with particular attention to the role of strain rates at mixture fraction levels most prone to autoignition, the so-called most reactive mixture fraction.

In view of these results, there appears to be a gap between experimental findings on the physical processes that are responsible for flame stabilisation in jet-in-hot-coflow flames and the conventional theories regarding lift-off height in non-premixed turbulent flames. Therefore, in this paper an attempt will be made to lay a theoretical foundation relating the lift-off height in jet-in-hot-coflow flames to the observed autoignition and convection processes. An accurate definition of lift-off height will be formulated first, and this definition will be used to compare the lift-off height of flames in the Delft Jet-in-Hot-Coflow

(DJHC) burner for a range of parameters, including coflow temperature, jet fuel composition and jet Reynolds number. Secondly, the effect of these parameters on the statistics of the autoignition process will be studied in detail. The relation between the statistics and the lift-off height is then used to explain the found trends for lift-off height.

2.2 Experimental setup

2.2.1 DJHC burner

Fig. 2.1 shows a sketch of the upper part of the DJHC burner. This burner is designed to deliver a flame that mimics the important characteristics of flameless combustion. It creates a turbulent diffusion flame of a gaseous fuel in a coflowing oxidiser stream of high temperature carrying little oxygen. A fuel jet, emerging from a long (approximately 200 diameters) tube with an inner diameter d of 4.5 mm, develops in a coflow of hot and diluted air. This coflow is generated by a secondary burner inside an annulus with a diameter of 82.8 mm. The coflow mixture fraction can be varied, influencing both the coflow temperature and oxygen level. Due to the enthalpy deficit of the coflow (the coflow loses heat to the surroundings through radiation and convective heat transfer) the flame burns in circumstances resembling those in a furnace in flameless combustion conditions, with peak temperatures in the flame lower than those of a natural gas jet flame in normal air. The design is similar to the Adelaide JHC burner [19]. The important difference is that the secondary burner is not fully but partially premixed, which allows for seeding of the various gas flows with micron size particles that act as flow tracers in particle image

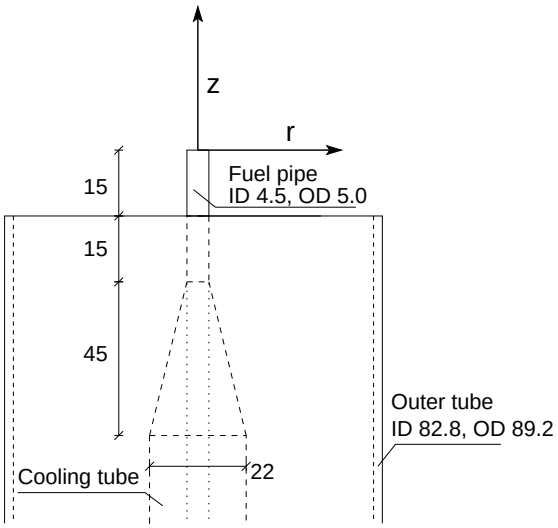

Figure 2.1: Relevant dimensions of the upper part of the DJHC burner. Dimensions are in millimeters.

velocimetry and/or laser Doppler anemometry. In this paper a z, r-coordinate system will be used with its origin at the centre of the fuel pipe exit. The z-coordinate is measured vertically upward.

2.2.2 Case description

Both cold coflow flames (so-called conventional lifted flames) and hot coflow flames have been studied. The cold coflow air has a temperature of 293 K, and a maximum mean velocity $v_{\mathrm{max;co}}$ of 0.5 m/s. Table 2.1 lists the characteristics of the two different hot coflows that were considered in this study. $\mathrm{T_{max;co}}$ represents the maximum temperature in the coflow, see section 2.3.1 for further details. The coflow temperature in the DJHC-I flame is about 80 K higher than that of the DJHC-V flame. The average O_2 mass fraction in the coflow is 8.4 % in the case of DJHC-I and 9.5 % in the case of DJHC-V. Three different fuels were used in the central jet: Dutch natural gas and two synthetic gases resembling Dutch natural gas, either a mixture of methane and nitrogen (fuel I) or a mixture of methane, ethane and nitrogen (fuel II), see table 2.2. The jet Reynolds number was varied between 3000 and 9500, and is based on the centerline velocity in the fuel tube and the dynamic viscosity of natural gas at 300 K for the cold coflow flames (1.14×10^{-5} Pa s) and that at 450 K for the hot coflow flames (1.60×10^{-5} Pa s)[1]. Unlike the cold coflow flames, the hot coflow flames do not have to be lit externally.

	fuel [nl/min]	air [nl/min]	$\mathrm{T_{max;co}}$ [K]	$v_{\mathrm{max;co}}$ [m/s]	$\mathrm{Y_{O2;co}}$ -
DJHC-I	16.1	224	1540	4.6	8.4%
DJHC-V	15.3	231	1460	4.3	9.5%

Table 2.1: Secondary burner flows and resulting maximum coflow velocity (measured with LDA) and maximum coflow temperature (measured with CARS) of the studied DJHC flames.

[mole %]	fuel I	fuel II	Dutch nat. gas
N_2	15.0	15.0	14.4
CH_4	85.0	81.0	81.3
C_2H_6	-	4.0	3.7
rest	-	-	0.6

Table 2.2: Compositions of the three fuels used in this study.

[1] In Appendix A, Reynolds numbers are given based on bulk velocities and corrected for the actual jet temperature.

2.2.3 Optical setup and image processing

The flame structure between z=0 mm (corresponding to the fuel jet exit) and z=160 mm was studied with an intensified high-speed camera (Lambert Instruments HI-CAM CR). This camera has a fibre-optically coupled two-stage intensifier with a sensitivity exceeding 50 mA/W for wavelengths between 200 nm and 550 nm. It was operated at a gate time of 400 μs. The CMOS sensor has 1280×1024 pixels, but only a quarter (1280×256) was used to achieve higher frame rates. A Nikkor UV 1:4.5, f=105 mm lens was used, with a spectral transmission level exceeding 70 % between 220 nm and 900 nm. The resolution of the resulting image is approximately 7 pixels mm^{-1}. The field of view was wide enough to capture the width of the flame up to $z \approx$130 mm. For the jet-in-hot-coflow flames, 10,000 frames were acquired at a frame rate of 2000 fps for each case. An identical frame rate and gate time, albeit at a lower intensifier gain, was used to study the dynamics of the cold coflow flames. To determine the lift-off heights of the cold coflow flames, 5000 frames were taken at 200 fps, to have a larger averaging time accounting for the longer time scales involved. A background image was subtracted from each image. This background image was constructed by averaging over 1000 frames with identical exposure time, frame rate and intensification, but without the presence of a flame.

To process the images, an averaging "disk" with a radius of 8 pixels was applied after subtraction of the background image to reduce the influence of noise. Then the flame boundaries were determined based on a threshold intensity level of 8 (255 being the maximum value), making use of the built-in Matlab routine `bwboundaries.m`. The dependence of the resulting lift-off height on chosen threshold values is small: within the margin of reasonable values for the threshold (flame pockets are detected as such, but noise is rejected) the difference in resulting lift-off is 3 mm.

The instantaneous leading- and trailing edge speeds of flame pockets v_{back} and v_{front} are determined from the boundary data by matching the locations of the projected edges in sequential images taken at t_n and t_{n+1}. The algorithm that determines these matches first finds candidates for the front edges at t_{n+1} from those at t_n, and selects the one with the smallest positive increment. If a front edge at t_n has multiple matches to t_{n+1}, the one with the smallest increment is selected. A front edge with no forward match has merged with the next (downstream) trailing edge, and this trailing edge is therefore also excluded as a candidate for a match with trailing edges at t_{n+1}. Front edges at t_{n+1} that have no backward match are recognised as being formed by an ignition event, and both the front edge and the trailing edge of this kernel are excluded as candidates for a match with edges at t_n. The remaining trailing edges at t_n and t_{n+1} are now matched in order of their axial location. As a result, trailing edges can have both positive and negative speeds, whereas front edge speeds are assumed to have positive speeds always. The accuracy of extracting speeds from the increments is limited by the precision with which the location of the flame boundary can be determined. This aspect has been investigated experimentally, by projecting a light dot moving on a screen, recording it with identical gain, gate time and frequency and

processing the resulting images with the boundary detection routine. The resulting mean speed was found to be unbiased, as it approximates the true speed within 1 %. The 95 % error interval of individual measurements is estimated at $\pm$ 1.1 m/s, independent of the light dot speed. It should be realised that growth speeds of ignition kernels at the moment of formation are inherently ill defined, because of the sudden increase of flame luminescence over their extents.

2.2.4 LDA system

LDA measurements were performed with a two-component, dual beam TSI-system. The green line (514.5 nm) and blue line (488 nm) of a 10 W Continuum Argon-ion laser were used to measure the axial and radial velocity components directly. Two of the incident beams (one of each colour) were frequency pre-shifted over 40 MHz by a Bragg cell to enable the detection of instantaneous flow reversals. The length and diameter of the measurement volume were 1.7 mm and 0.12 mm, respectively. Scattered light was collected in back-scatter mode. The photomultiplier output signals were electronically down-mixed, and subsequently collected by a FSA-3000 signal processor. All statistics were computed as transit-time weighted results to eliminate the effects of the velocity bias. Autocorrelation functions of the axial velocity component were constructed from time series with 4×10^5 velocity samples that were acquired at a mean data rate of approximately 500 Hz by using the slotting method with local normalisation [46].

2.2.5 CARS system

Temperatures were determined with a CARS system that has been described in detail in [47]. In a planar-boxcars phase-matching configuration, a probe volume of 700 μm length and 35 μm diameter is obtained. The single-shot imprecision of the system (one standard deviation) is 1% - 4% over a range from 2000 K to 300 K. The inaccuracy (the systematic error) is estimated to be 20 K. For each position in space, mean temperatures were determined from the results of 1000 single-shot CARS spectra.

2.3 Results and discussion

2.3.1 Details of the coflow

Fig. 2.2 shows the mean temperature field at z=3 mm of the two coflows DJHC-I and DJHC-V. The coflow temperature is not constant, but depends on the radial location r.

The velocity fields of the DJHC-I and DJHC-V flames at z=3 mm are presented in Fig. 2.3. The larger mass flow of the DJHC-V coflow is compensated by its lower temperature and, consequently, higher density to yield nearly identical velocities.

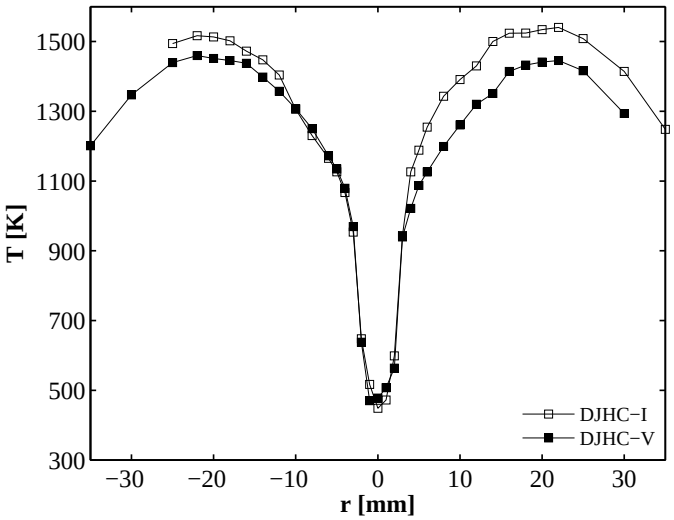

Figure 2.2: Mean temperature in the DJHC-I and DJHC-V flames at z= 3 mm, obtained with coherent anti-Stokes Raman spectroscopy (CARS). The RMS of the coflow temperature is typically 120 K. Dutch natural gas was used in the jet stream, with a jet Reynolds number of 4500.

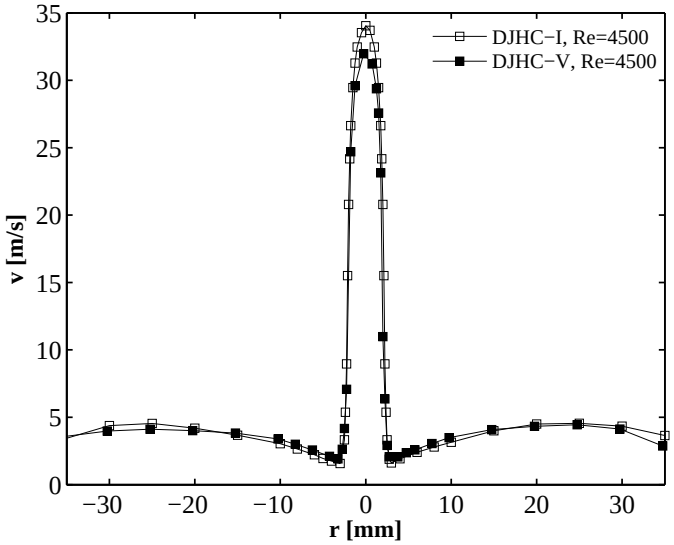

Figure 2.3: Mean axial velocity in the DJHC-I and DJHC-V at z=3 mm, obtained with laser Doppler anemometry. Dutch natural gas was used in the jet stream, with a jet Reynolds number of 4500.

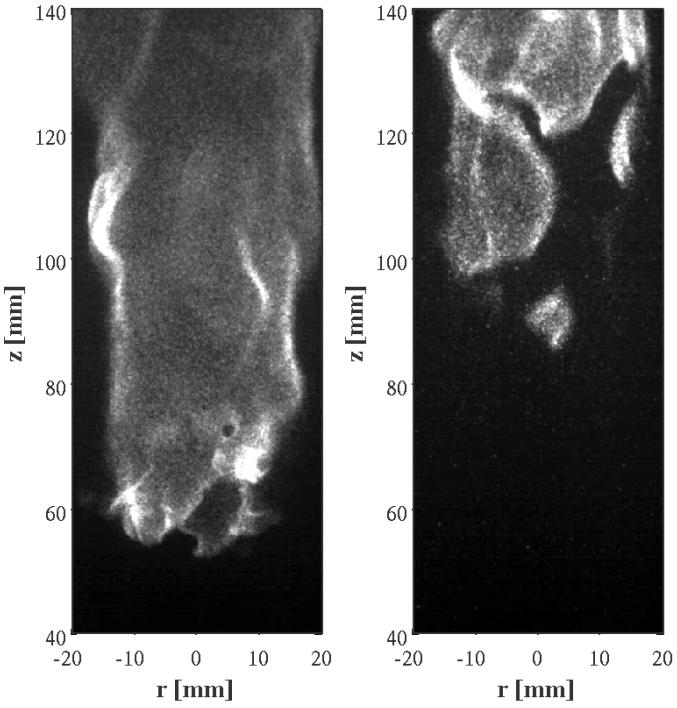

Figure 2.4: Images of the flame base of a conventional lifted flame of Dutch natural gas at $\mathrm{Re_{jet}}$=4500 (left) and of the jet-in-hot-coflow flame DJHC-V (Dutch natural gas at $\mathrm{Re_{jet}}$=4500, right).

2.3.2 Visual observations

Fig. 2.4 shows two images of the flame base of a conventional lifted jet flame (left) and the DJHC-V (right). In both cases the fuel is Dutch natural gas and $\mathrm{Re_{jet}}$=4500. Qualitative differences between the conventional lifted flame and the jet-in-hot-coflow flame are evident. The conventional lifted flame has a sharp, connected interface with mild indentations. The jet-in-hot-coflow flame shows large spatial and temporal variations in flame interface height. Isolated flame pockets develop for $z > 80$ mm. These grow while being convected downstream where they merge thus forming a more-or-less continuous flame zone at $z \approx 120$ mm.

To study the time evolution of the pockets, the boundary detection routine mentioned earlier will be used. As an example, Fig. 2.5 shows three sequential luminescence images (DJHC-V, fuel II, $\mathrm{Re_{jet}}$=7000) with the green contours indicating the boundaries of detected flame pockets. In the following, regions in space displaying enough luminescence to be recognised by the boundary detection routine as burning will be referred to as flame pockets. Flame pockets at their first instant of detection will be referred to as ignition ker-

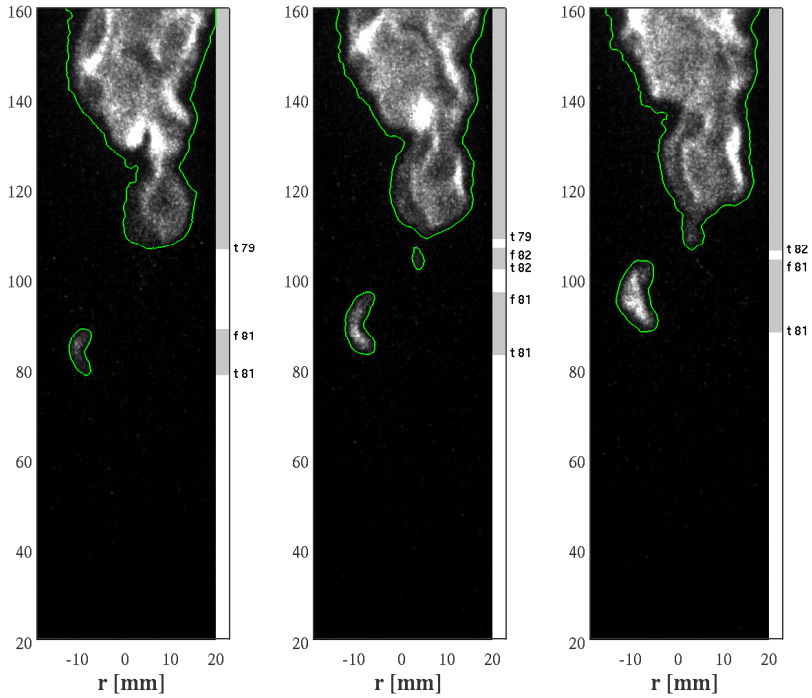

Figure 2.5: Three sequential images from the case DJHC-V, fuel II, $\mathrm{Re_{jet}}$=7000, showing the evolution in time of the detected flame boundaries (with a 1 ms time separation, intermediate frames are removed). The bar on the right shows whether a flame pocket is present on the axial location (grey) or not (white), and the numbers indicate which trailing edges (numbers preceded by a "t") and front edges are matched by the algorithm that determines the increments, from which the projected flame speeds v_{back} and v_{front} are calculated. The new number "82" in the middle picture shows that an ignition event was recognised.

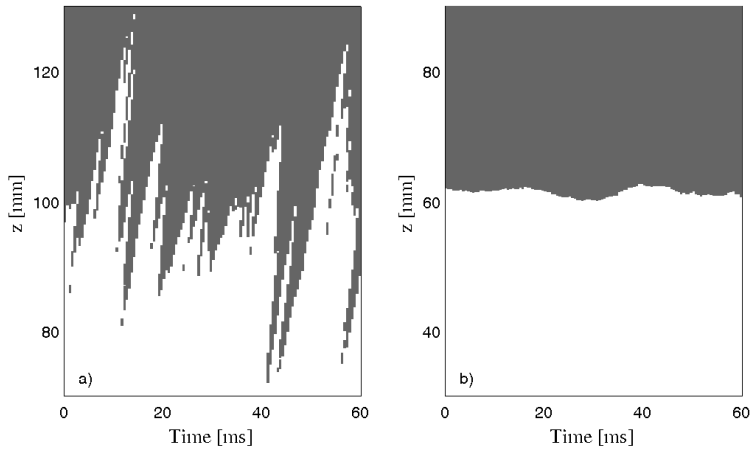

Figure 2.6: The time evolution of the axial location of flame pockets $b_2(z,t)$. a): DJHC-V, fuel II, $\mathrm{Re_{jet}}$=5000 b): a lifted flame in cold coflow, Dutch natural gas, $\mathrm{Re_{jet}}$=4500.

nels. The grey bars on the right of each image in Fig. 2.5 represent the projection of the flame pockets on the vertical coordinate axis. This one-dimensional function, referred to as $b_2(z,t)$ has logical values (zero if no flame pocket is present and one if a flame pocket is present). Most of this paper will be related to the statistics of this function in time. Although the projection on the axis leads to a loss of information, there are good reasons to study b_2 and not the two-dimensional boundary information. Most importantly, due to the axisymmetry of the flame, the relevant ignition statistics are a function of z only. As a consequence, $b_2(z,t)$ contains all information needed to get the desired information on ignition statistics. Line-of-sight effects makes the distinction between apparently overlapping pockets impossible, as both the front and the back side of the flame are observed. However, statistics on speeds of trailing and leading edges can be acquired from $b_2(z,t)$, when edges of flame pockets occur axially separated from other flame pockets. Therefore, the essential features of the observed process, namely the formation of ignition kernels and the growth of the resulting flame pockets, can be retrieved by studying $b_2(z,t)$ alone.

The two plots in Fig. 2.6 show a small fraction of $b_2(z,t)$ for a jet-in-hot-coflow flame and a conventional lifted flame (cold-coflow flame). The hot-coflow flame is seen to behave very differently from the ordinary jet diffusion flame, in which a single sharp interface moves up and down. The flame pocket behaviour in the jet-in-hot-coflow flames bears the characteristics of a process of random ignition kernel formation, growth and convection.

2.3.3 Definition of lift-off height

The lift-off height is related to the probability of the presence of flame pockets. Two different flame probabilities are defined, P_{b1} and P_{b2}. $P_{b1}(z)$ is the probability of finding

a flame pocket anywhere on a radial line stretching outward from the burner axis, as a function of axial height. It could be determined from a planar imaging technique, such as planar laser-induced fluorescence (PLIF) by observing a radial cross-section that stretches outward from the centre and calculating the fraction of time a burning interface is found as a function of z. P_{b1} can not be determined directly in this experimental setup, since the luminescence images result from a line-integration. However, by assuming axi-symmetry of the flame and statistical independence of the "front" and "back" of the flame, it can be reconstructed from the flame boundary observations on the centreline of the image:

$$P_{b1}(z) = 1 - (1 - P_{b1;cl}(z))^{1/2} \ , \tag{2.1}$$

where $P_{b1;cl}(z)$ is the fraction of time a pixel at height z on the centreline contains a burning pocket. The second probability $P_{b2}(z)$ is that of finding a flame pocket at a certain axial height, and is the expectation of the function $b_2(z,t)$ that was discussed in the previous section. This quantity is best visualised by drawing a horizontal line in one of the graphs in Fig. 2.6. P_{b2} is the fraction of the line that is in the grey region, as a function of z.

The function b_2 is equal to one whenever $b_1(\phi, z, t)$ is equal to one for an azimuthal angle ϕ, and it is as such not an azimuthally averaged property. However, studying its time evolution has a clear advantage over studying the time evolution of b_1 since it is not affected by "in-plane" transport. This enables a more rigorous analysis of the ignition and transport processes and for this reason, the focus will be primarily on b_2. In this respect, the used technique has an advantage over a planar diagnostic technique, where one cannot with certainty distinguish between true flame islands and filament-like structures being convected through the measurement plane [48], and simultaneous measurement of the velocity component into the plane is needed to interpret planar images of radicals [49].

Both probabilities P_{b1} and P_{b2} are shown in Fig. 2.7 for the two flames DJHC-I and DJHC-V. The lift-off height h_1 is now defined as the axial location where P_{b1} equals 50 %. A second lift-off height h_2 based on P_{b2} will also be used in the analysis. The locations corresponding to these lift-off heights are shown together with average luminescence images in Fig. 2.8. As expected, h_1 is located at the height where the gradient in luminescence is high. Note that in the two flames at the bottom of the picture, there is a large margin for choosing a lift-off height based on time averaged visual observations.

Figs. 2.9 and 2.10 show the lift-off heights as a function of the jet Reynolds number for the different flames. Both definitions for lift-off height yield similar trends. The minimum lift-off height h_1=18 d is found in flame DJHC-I with natural gas as fuel and at a Reynolds number of 4500. In all cases, the value of h_1 (or h_2) has a minimum at a moderate Reynolds number of approximately 5000. The value of h_2 exceeds the field of view of the camera for the flame DJHC-V with fuel I at $\mathrm{Re_{jet}}$=9500. This happens in several more cases for h_1, most notably in flame DJHC-V with fuel I at all Reynolds numbers. The difference between h_2 and h_1 for identical cases increases with larger Reynolds numbers. This trend will be explained in section 2.3.8.

To place these results in some context, two reference cases should be mentioned. The

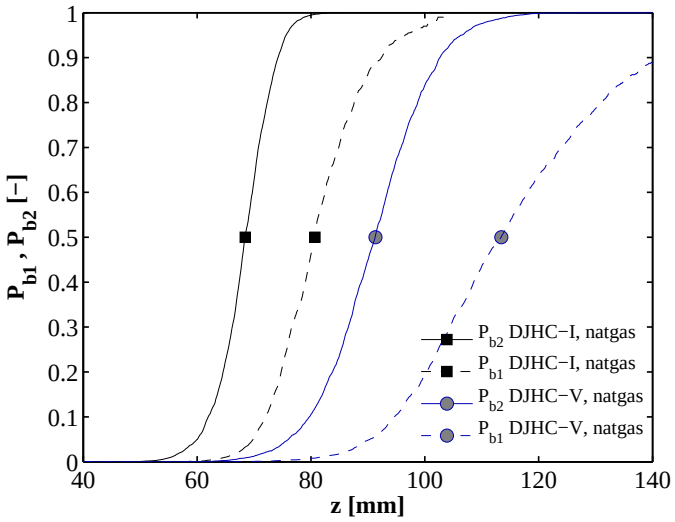

Figure 2.7: The probabilities of finding a flame at an axial height on any location (P_{b2}) and at an axial height on a radial line (P_{b1}), for the DJHC-I and DJHC-V flames with natural gas, $\mathrm{Re_{jet}}$=4500. The symbols indicate the location where the probabilities are 0.5.

lift-off height in the vitiated coflow burner as described in Cabra et al. [20] has been studied for a range of Reynolds numbers, with a CH_4/air fuel stream and T_{co} equal to 1350 K [37], and with an H_2/N_2 fuel stream and T_{co} equal to 1045 K [32]. The fuel jet has an inner diameter d of 4.57 mm, comparable to the 4.5 mm of the DJHC burner. In the first study, lift-off heights (based on average flame luminescence) at a coflow velocity of 4.2 m/s ranged between $h/d \approx 11$ to $h/d \approx 30$ for a jet Reynolds number ranging between 23000 and 72000 (v_{jet} from 80 m/s to 250 m/s), in a linear fashion. In the second study, lift-off heights ranged from $h/d \approx 3$ to $h/d \approx 20$ for a Reynolds number range of 11000 to 35000 (v_{jet} from 45 m/s to 160 m/s) with a coflow velocity equal to 3.5 m/s. A monotonically increasing trend was found again, with a steepening towards higher jet velocities. An initially decreasing trend as seen here has not been found in either case, the coflow temperature profile in these cases is however flat and the Reynolds numbers involved are higher.

Variation in fuel composition through the addition of higher alkanes (ethane in fuel II and propane and butane in Dutch natural gas) affects lift-off height strongly. This is in agreement with the strong influence of chemistry in jet-in-hot-coflow flames, which has been pointed out in previous numerical studies [30, 50]. The results are in line with the fact that higher alkanes tend to reduce the autoignition delay times of natural gas mixtures [51].

Figs. 2.9 and 2.10 also show the lift-off behaviour of conventional jet flames for the three different fuels. In this case, the dependence of lift-off height on fuel composition is very weak. The Reynolds number dependence as indicated with the thick dashed line fol-

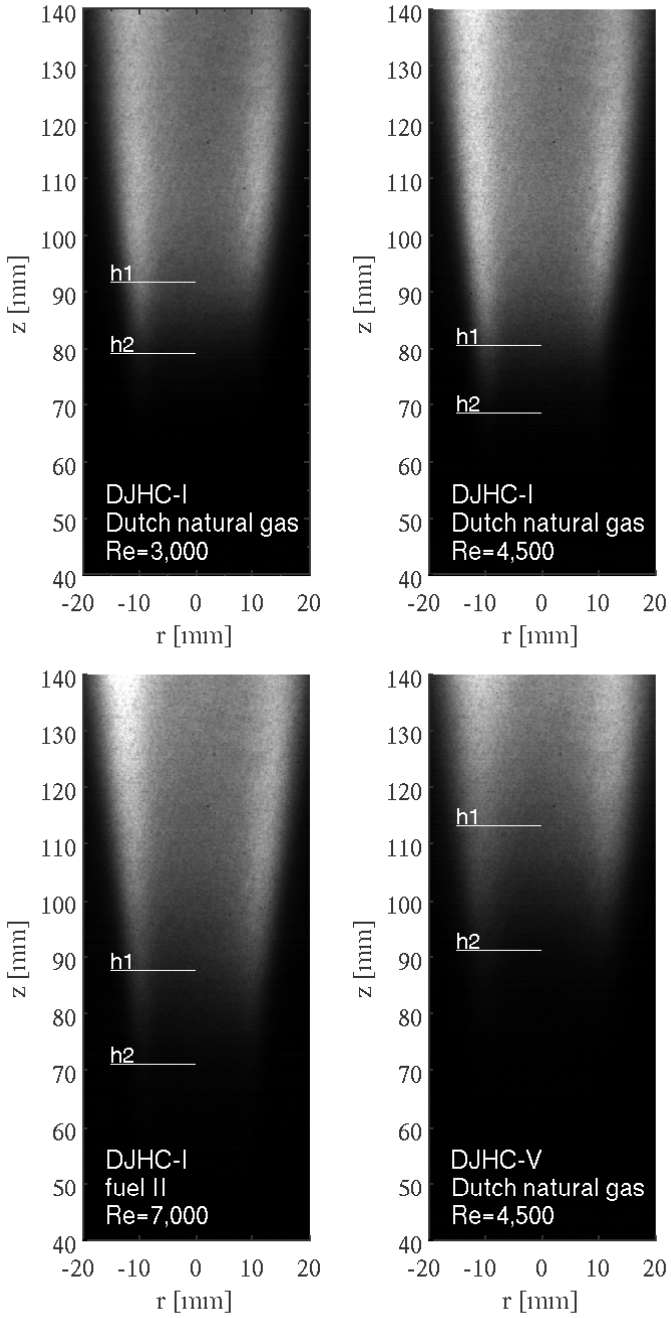

Figure 2.8: The locations of P_{b1}=50% (h_1) and of P_{b2}=50% (h_2) marked on averaged images of four flames.

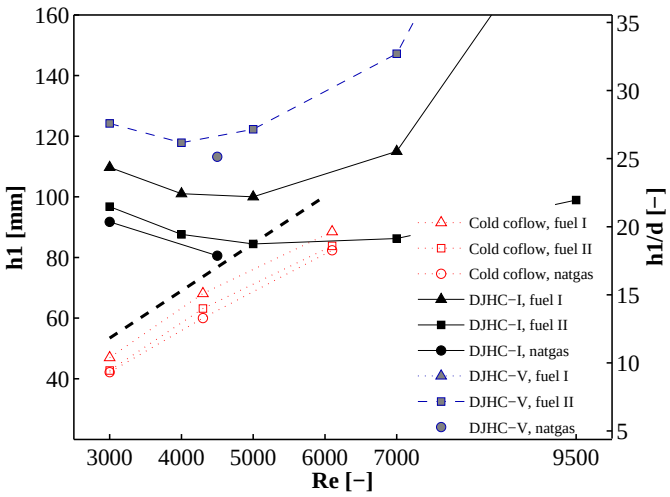

Figure 2.9: Lift-off heights based on P_{b1} against jet Reynolds number. Note that the lift-off height of case DJHC-V with fuel I exceeded 160 mm for each jet Reynolds number. The thick, dashed line represents the correlation for lift-off height by Kalghatgi [40].

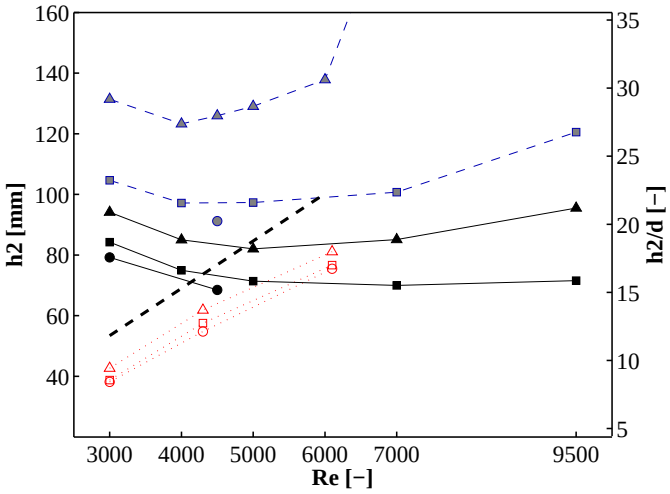

Figure 2.10: Lift-off heights based on P_{b2} against jet Reynolds number. See for the legend Fig. 2.9.

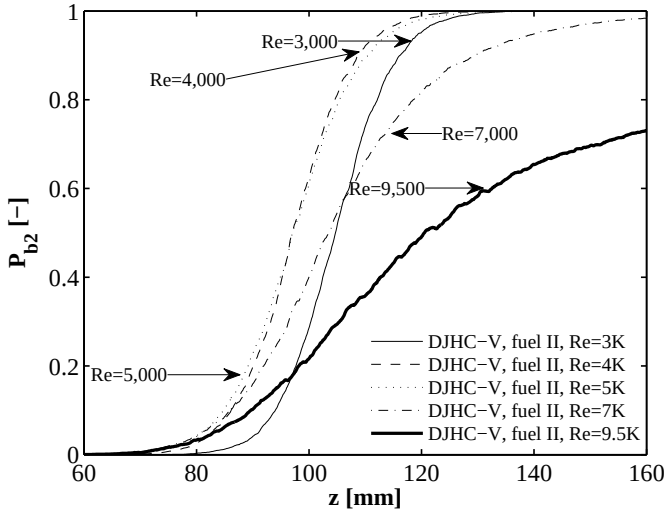

Figure 2.11: The curve of P_{b2} for a range of Reynolds numbers, DJHC-V fuel II.

lows the relation of Kalghatgi [40] qualitatively, being linearly dependent on the Reynolds number. The coflow velocity of 0.5 m/s is accounted for in this calculation through the effective velocity as proposed by Montgomery et al. [52].

The issue to be addressed now is what processes cause the strong differences in lift-off height for different fuels, Reynolds numbers and coflow temperatures. For this purpose, the probability function $P_{b2}(z)$ will be studied.

2.3.4 Axial location of first occurrence of autoignition kernels

Fig. 2.11 illustrates the influence of the jet Reynolds number on the probability P_{b2} and thus on the lift-off height h_2. It can be seen that the decrease of lift-off height for increasing Reynolds number up to $\mathrm{Re_{jet}}$=5000 is mainly due to a horizontal shift of the curve.

The location where ignition kernels first occur, $z_{\mathrm{b;min}}$ (arbitrarily defined as the location where P_{b2} equals 2.5×10^{-3}), shifts downward and so does the entire curve. For higher Reynolds numbers, $z_{\mathrm{b;min}}$ is hardly affected, but the gradient of the curve of P_{b2} decreases.

Fig. 2.12 illustrates the effect of coflow temperature, fuel composition and Reynolds number on $z_{\mathrm{b;min}}$. Replacing only 4% methane by ethane (fuel II vs. fuel I) strongly decreases $z_{\mathrm{b;min}}$, especially in DJHC-V where the coflow temperature is relatively low. The impact of increasing the jet Reynolds number is remarkable. Instead of transporting gas mixtures further away from the jet exit before autoignition due to the higher velocities, it causes $z_{\mathrm{b;min}}$ to decrease initially in all cases. In the flame DJHC-V, with fuel I, $z_{\mathrm{b;min}}$ rises again above $\mathrm{Re_{jet}}$=5000, indicative of hindered formation of ignition kernels. Simply translating the axial coordinate to the residence time of a fluid parcel leads to the conclusion that autoignition delay times are reduced under the influence of increasing jet Reynolds

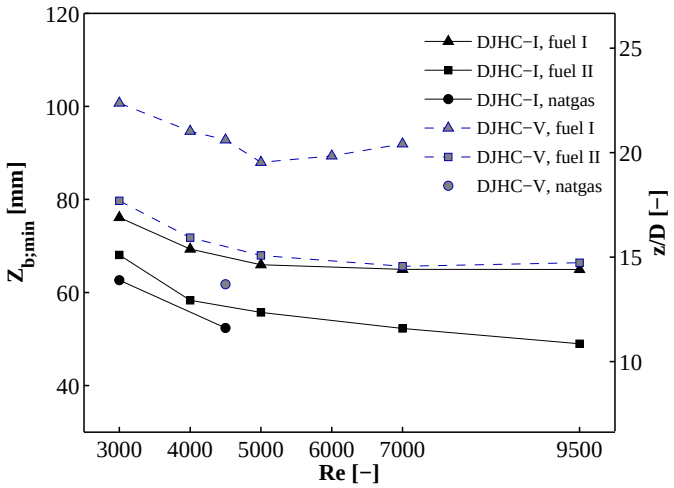

Figure 2.12: The location of first ignition events $z_{\mathrm{b;min}}$ against jet Reynolds number.

number. Under the condition that the ignition time is larger than the typical turbulence time, faster mixing will lead to earlier generation of well-mixed spots promoting autoignition, a possibility discussed in [45]. This conclusion can however not be drawn here, because turbulence will cause variation in fluid parcel residence times at a given location. Moreover, the faster entrainment of the hotter inner part of the coflow for increasing Reynolds number is expected to play a dominant role.

2.3.5 Transport of flame pockets

After a flame pocket has been formed, the pocket will grow while being convected downstream. Clearly, the axial velocity of the leading edge of the flame pocket v_{front} must be larger than the axial velocity of the trailing edge, v_{back}, for the axial extent of the flame pocket to increase. If flame stabilisation by flame propagation does not play a role, v_{back} should be larger than zero. The physical relevance of these velocities to the lift-off height can be demonstrated in a simple example where ignition events take place at a fixed location and at regular time intervals with frequency f_{ign}. At streamwise distances from the ignition location larger than

$$\Delta z = \left(\frac{1}{v_{\mathrm{back}}} - \frac{1}{v_{\mathrm{front}}} \right)^{-1} \frac{1}{f_{\mathrm{ign}}} \,, \tag{2.2}$$

there will be a flame at any instant in time. This illustrates that increasing v_{back} increases the lift-off height, while increasing the ignition frequency f_{ign} decreases the lift-off height.

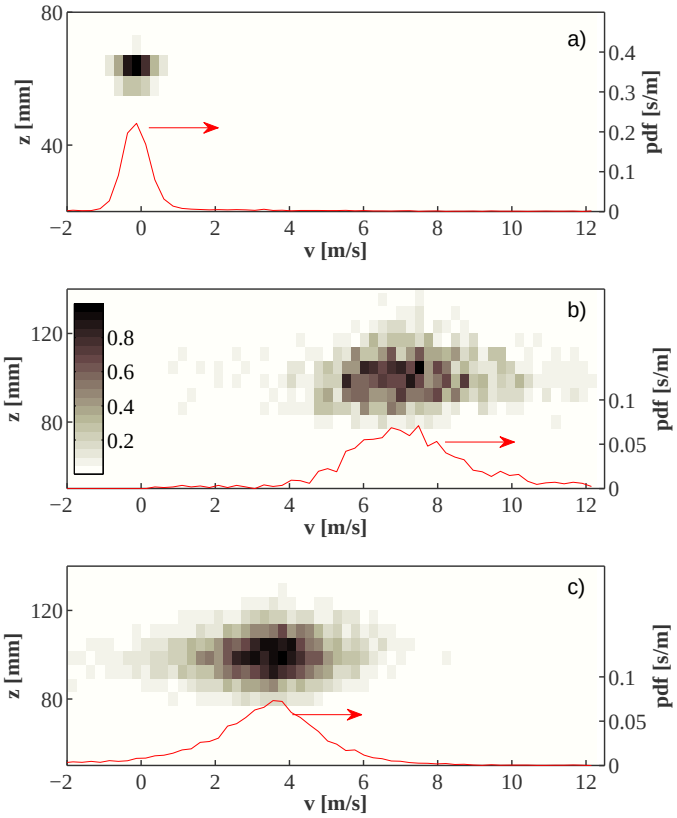

Figure 2.13: Normalised 2D histograms of velocity and location (greyscale plot) and pdfs of velocity (red line, right axis), of trailing edge in a conventional lifted flame (Dutch natural gas) (a), leading edges (b) and trailing edges (c) of flame pockets in flame DJHC-V, fuel II. The jet Reynolds number is 5000 in all cases. The 2D histogram is normalised such that the cell with the maximum number of counts for each case gets a value equal to one.

Histograms showing the measured values of v_{back} and v_{front} of a DJHC-V flame and the trailing edge speeds of a conventional lifted flame determined by the routine as described in section 2.2.3 are shown in Fig. 2.13. These flame speeds are not to be confused with the propagation speeds of flame structures such as studied in flat flame configurations: firstly the speed is not measured relative to its surrounding fluid, and secondly it is subject to horizontal projection. The correlation between these speeds and axial height z is very weak. As a consequence, the mean values of the pocket edge speeds can be treated to a first approximation as being independent of axial height z.

Attention will now be given to the influence of the different parameters on the mean axial flame speeds $\overline{v}_{\mathrm{front}}$ and $\overline{v}_{\mathrm{back}}$. The results for all cases are shown in Fig. 2.14. The effect of jet Reynolds number on $\overline{v}_{\mathrm{front}}$ is small, whereas $\overline{v}_{\mathrm{back}}$ clearly increases. This can be interpreted as a mild increase of the mean speed with which flame pockets are convected

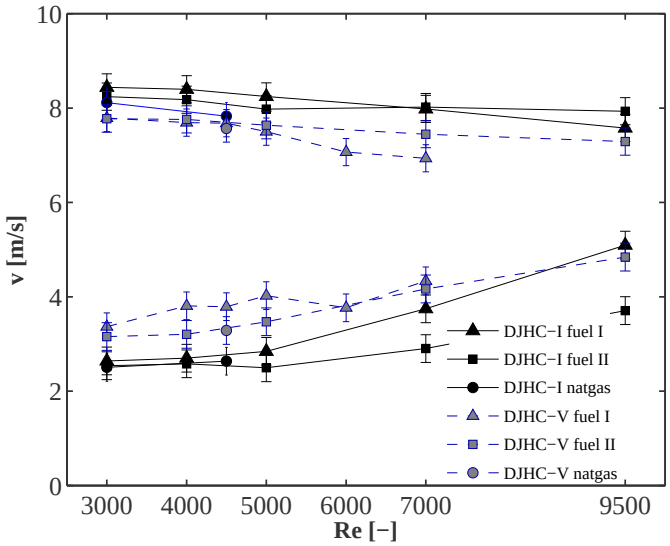

Figure 2.14: Observed front- and trailing edge speeds in axial direction at different jet Reynolds numbers. Both the $\overline{v}_{\mathrm{back}}$- and $\overline{v}_{\mathrm{front}}$ errorbars are based on the RMS value of differences between the values obtained from the first and last set of 5,000 images of their respective groups. Cases with insufficient statistics (less than 500 samples) were discarded.

v_0, (assumed to be the average of $\overline{v}_{\mathrm{back}}$ and $\overline{v}_{\mathrm{front}}$), combined with a stronger decrease in the mean projected flame propagation speed (the difference between $\overline{v}_{\mathrm{back}}$ and $\overline{v}_{\mathrm{front}}$ divided by two), for increasing jet velocity. The first trend is in agreement with the mean location of the reaction zone being near the outer edge of the jet.

CARS measurements indicate that the reaction zone at z=120 mm is located between r=13 mm and r=15 mm (case DJHC-I, $\mathrm{Re}_{\mathrm{jet}}$=4500 and Dutch natural gas as fuel). Here, the mean velocity is mainly set by the coflow and is thus only mildly dependent on the jet Reynolds number. For example, the measured mean velocity at z=120 mm and r=14 mm increases from 5.0 m/s at a jet Reynolds number of 3000 to 6.6 m/s at Re=9500, close to the values of v_0. The location of the reaction zone also explains the lack of correlation between axial height and flame speed, as the axial gradients of mean velocity in the coflow are small. The properties of the flow field in the flame region are shown in more detail in section 2.3.7. The DJHC-V flames have consistently lower projected flame propagation speeds, which might be caused by lower true flame propagation speeds or by an increase of curvature of the contours along which the flame propagates. The latter might be caused by the higher oxygen content in the coflow, increasing the stoichiometric mixture fraction and thereby moving the reaction zone closer to the shear layer of the jet.

2.3.6 Flame transfer probability

As explained in the previous section, the flame pocket growth is determined by leading and trailing edge speeds. The function that completely describes the convection, growth and possible extinction of newly formed ignition kernels is the flame transfer probability, $P_{\mathrm{tr}}(\Delta z, \Delta t)$. This function describes the probability that an ignition event $I(z,t)$ generates a burning flame at an axial distance Δz and time lapse Δt from this event. In the case of fixed flame speeds,

$$P_{tr;\mathrm{fixed}}(\Delta z, \Delta t) = \begin{cases} 1 & \text{if } \overline{v}_{\mathrm{back}} \leq \frac{\Delta z}{\Delta t} < \overline{v}_{\mathrm{front}} \\ 0 & \text{otherwise .} \end{cases} \tag{2.3}$$

This expression for P_{tr} ignores the possibility of velocity variations, or extinction, of a newly formed flame pocket. Therefore, a more refined method is needed, using $b_2(z,t)$ directly to obtain the flame transfer probability.

To demonstrate the relation between b_2 and P_{tr}, consider a single realisation of $b_2(z+\Delta z, t+\Delta t)$, conditional on an ignition event $I(z,t)$. The resulting field of $b_2(z+\Delta z, t+\Delta t)$ is the union of the field in absence of this ignition with the flame evolution of this specific ignition event, $tr(\Delta z, \Delta t)$. The expectation of b_2 (the arguments are omitted for brevity) conditional on the ignition event I follows from

$$\begin{aligned} \mathbb{E}\left\{b_2 \mid \mathrm{I}\right\} &= \mathbb{E}\left\{tr\right\} + \left(1 - \mathbb{E}\left\{tr\right\}\right) \mathbb{E}\left\{b2\right\} \\ &= P_{\mathrm{tr}} + \left(1 - P_{\mathrm{tr}}\right) P_{\mathrm{b2}}, \end{aligned} \tag{2.4}$$

using statistical independence of the individual ignition events. Note that $\mathbb{E}$ is the "expected value" operator and "$\mid$" denotes that a conditional expectation is considered. Rewriting Eq. (2.4) leads to the following equation (written out fully):

$$P_{\mathrm{tr}}(\Delta z, \Delta t) = \frac{\mathbb{E}\left\{b_2(z+\Delta z, t+\Delta t) \mid \mathrm{I}(z,t)\right\} - P_{b2}(z+\Delta z)}{1 - P_{b2}(z+\Delta z)} \,. \tag{2.5}$$

In practice this means extracting samples of $b_2(z,t)$ (see Fig. 2.6) around a large number of ignition events accounting each time for the locally expected value of b_2 which is $P_{b2}(z+\Delta z)$. This approach works well, provided that the value of P_{b2} is not too large, and ignition events can be identified accurately. Both requirements are fulfilled by considering only ignition events at locations of low flame probability, say $P_{b2} < 0.03$. The resulting statistics consist typically of around 200 samples, with a minimum of 123 samples for the case DJHC-V with fuel I at a jet Reynolds number of 7000. Fig. 2.15 shows the flame transfer probability $P_{\mathrm{tr}}(\Delta z, \Delta t)$ for four Reynolds numbers in DJHC-V flames with fuel II. These figures clearly show the mean downstream convection and growth of newly created flame pockets. The dotted blue lines according to Eq. (2.3) correspond well to the found flame transfer probability functions. For the highest Reynolds numbers, the effects of inhibited

growth of ignition kernels and even extinction become important, as can be observed by the decrease of the transfer probability in the region between the blue dotted lines for increasing values of Δz and Δt.

The function P_{tr} acts as a convolution kernel on the ignition frequency density $f_{\mathrm{ign};2}(z)$ (the frequency of formation of ignition kernels per unit axial length in absence of a flame) to yield the flame probability P_{b2} (with the introduction of the dummy variables z' and t'):

$$P_{b2}(z,t) = \overline{b_2} = 1 - \exp\left[-f_{\mathrm{ign};2}(z',t') * P_{tr}(\Delta z, \Delta t)\right], \tag{2.6}$$

where "$*$" is the convolution operator. Therefore, the results in Fig. 2.15 enable the quantification of the growth of kernels and to relate ignition frequencies to the flame probability P_{b2}.

Using the time invariance of the ignition frequency, and the ansatz

$$\int P_{tr}\left(\Delta z, \Delta t\right) \mathrm{d}t = \Phi \Delta z, \tag{2.7}$$

Eq. (2.6) can be rewritten as a simple integral over the axial height z :

$$P_{\mathrm{b};2}(z) = 1 - \exp\left[-\Phi \int f_{\mathrm{ign};2}(z')\left(z - z'\right)\ \mathrm{d}z'\right]. \tag{2.8}$$

The parameter Φ is the derivative of the expected residence time of a projected flame pocket pertaining to an ignition event (the time between arrival of the front edge and arrival of the trailing edge) with respect to z. Note that $\Phi = 0$ implies no flame growth and hence no flame stabilisation whilst $\Phi \rightarrow \infty$ corresponds to stabilisation by flame propagation. Fig. 2.16 shows the time integral of P_{tr} for a range of distances from the ignition event, Δz. The assumption of linearity in Δz appears to be appropriate. The values for lower Reynolds numbers are comparable to those calculated assuming fixed flame speeds, in which case Φ simply follows from:

$$\Phi_{\mathrm{fixed}} = \frac{1}{\overline{v}_{\mathrm{back}}} - \frac{1}{\overline{v}_{\mathrm{front}}}\,. \tag{2.9}$$

A characteristic of all curves is that they do not intersect the origin. This is caused by the fact that ignition kernels already have a certain size at the moment they are detected by the image processing routine. They appear as vague "streaks" of a certain size one or two frames before fully igniting and being accurately detectable. The average kernel length in axial direction upon detection is between 3 and 5 mm. This is comparable to the radius of the averaging disk (1mm) and the convective displacement during the 400 μs exposure time (2.4 mm). Quantification of the true size of kernels at the moment of detection is therefore not undertaken here.

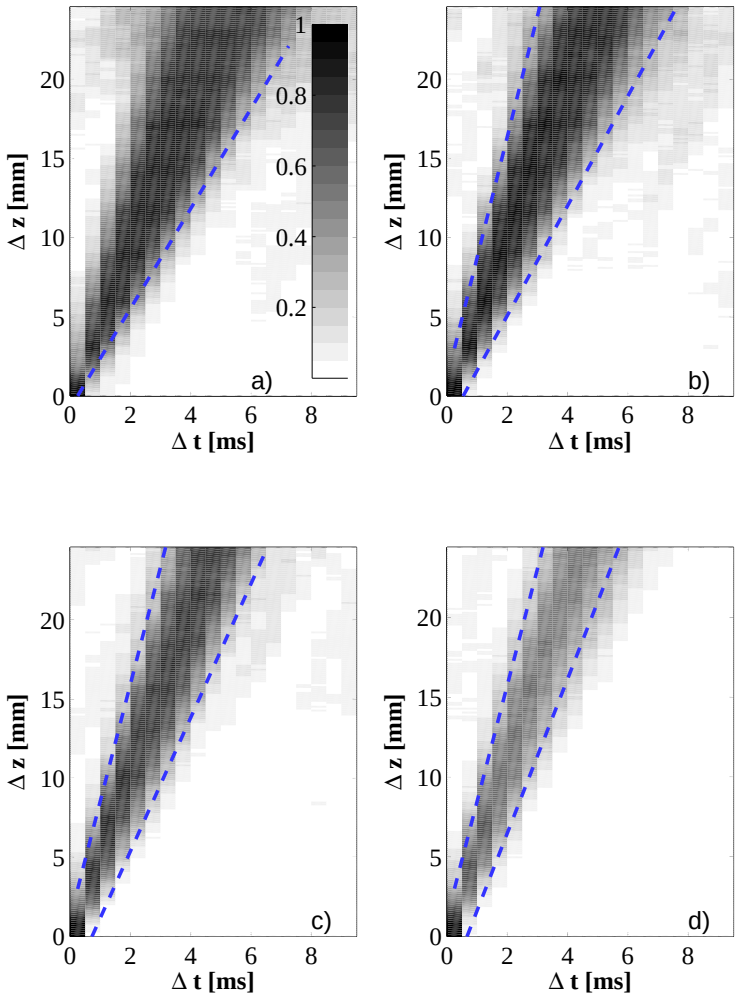

Figure 2.15: The flame transfer probability P_{tr}, for flame DJHC-V, fuel II, with Reynolds number 3000 (a), 5000 (b), 7000 (c) and 9500 (d). It denotes the ensemble-averaged evolution of a flame kernel starting from its creation at $\Delta t = 0$. Each plot consists of approximately 200 of these samples. Note that at the highest Reynolds number, P_{tr} becomes more sparse, which is caused by occasional extinction events. The dotted blue lines show the pocket evolution corresponding to the values of $\overline{v}_{\text{front}}$ (steepest curve) and $\overline{v}_{\text{back}}$, as determined in section 2.3.5.

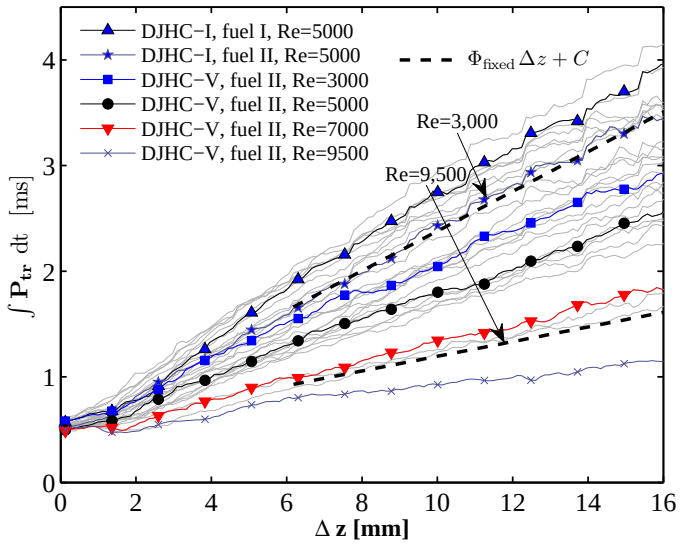

Figure 2.16: The value of the time integral over P_{tr} as function of Δz, for several cases. The thick dashed black lines denote the slope based on Eqs. (2.7) and (2.9) and the flame speeds $\overline{v}_{\text{front}}$ and $\overline{v}_{\text{back}}$, of flame DJHC-V with fuel II for a jet Reynolds number of 3000 (top line) and 9500 (bottom line). The thin grey lines represent the values of all hot coflow cases, to give an impression of the amount of scatter between cases.

2.3.7 Ignition frequencies

The ignition frequency may be determined from the flame boundary data. However, validation of the used ignition kernel detection routine against Monte Carlo simulations showed that it was unreliable in regions where P_{b2} has a significant value, say $P_{b2} > 0.3$, and at higher ignition frequency densities. Another shortcoming of the detection routine is that it is unable to recognise ignition events in rapid succession over small distances. An exact expression for $f_{\text{ign};2}(z)$ derived from Eq. (2.8) involves the second spatial derivative of P_{b2}, which results in very noisy data. The following measure for the mean ignition frequency is therefore used instead, based on the more robust quantity $\mathrm{d}P_{b2}/\mathrm{d}z$. Differentiating Eq. (2.8) gives

$$\left.\frac{\mathrm{d}P_{b2}}{\mathrm{d}z}\right|_{P_{b2}=1/2} = \frac{\Phi}{2}\int_0^{z(P_{b2}=1/2)} f_{\text{ign};2}\,\mathrm{d}z = \frac{\Phi}{2}\,(h_2 - z_{\text{b;min}})\,\langle f_{\text{ign};2}\rangle\,. \tag{2.10}$$

Renaming the length-scale $(h_2 - z_{\text{b;min}})$ to $L_{1/2}$ gives:

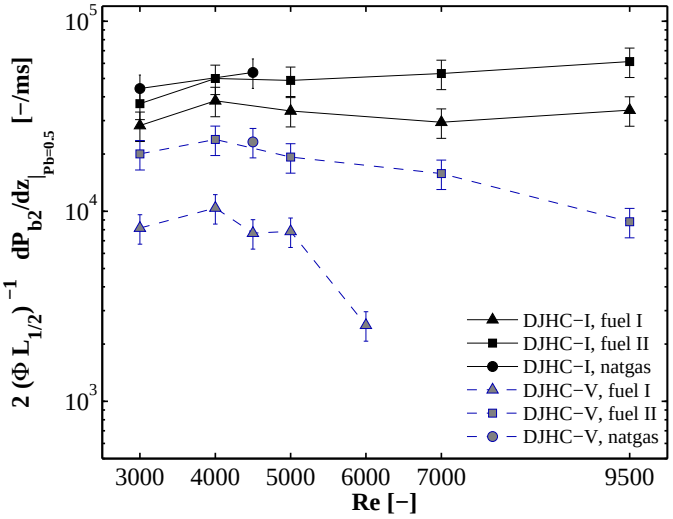

Figure 2.17: Mean ignition frequency densities $\langle f_{\mathrm{ign};2} \rangle$ as determined with Eq. (2.11) against jet Reynolds number, presented on a semi-log scale.

$$\langle f_{\mathrm{ign};2} \rangle = \frac{2}{\Phi\ L_{1/2}} \left. \frac{\mathrm{d}P_{b2}}{\mathrm{d}z} \right|_{P_{b2}=1/2} . \tag{2.11}$$

Fig. 2.17 shows the mean ignition frequency $\langle f_{\mathrm{ign};2} \rangle$ as a function of jet Reynolds number for several flames. The value of $\langle f_{\mathrm{ign};2} \rangle$ has been determined with Eq. (2.11) using linear fits to the curves of $P_{b2}(z)$ and those in Fig. 2.16 to obtain their derivatives. The ignition frequencies thus found range between 2×10^3 m^{-1}s^{-1} and 6×10^4 m^{-1}s^{-1}. The average ignition frequency density calculated by the image processing routine reproduces the trends and figures for the DJHC-V flames, but the higher values are not reproduced, which is due to the shortcomings mentioned earlier. The mean ignition frequency densities of flames DJHC-I are at least two times larger than those in flames DJHC-V, and fuels with higher alkanes yield consistently higher values. The jet Reynolds number hardly has any influence on the ignition frequencies in flame DJHC-I, whereas flame DJHC-V is more sensitive to the Reynolds number, especially for fuel I.

The diminished frequency of ignition events (in DJHC-V) and increased probability of kernel extinction and limited flame pocket growth (in all cases) is expected to originate from the larger strains in the turbulent field at higher Reynolds numbers. The large role of strains on autoignition has been pointed out in previous DNS-studies [53, 54, 55]. Echekki et al. [55] showed the evolution of ignition kernels in 2-D DNS calculations with detailed hydrogen-air chemistry. A species-specific Damköhler number was introduced, and observed extinction events were related to excessive heat and species dissipation. Very recently, experimental evidence has been obtained showing that ignition kernels with super-

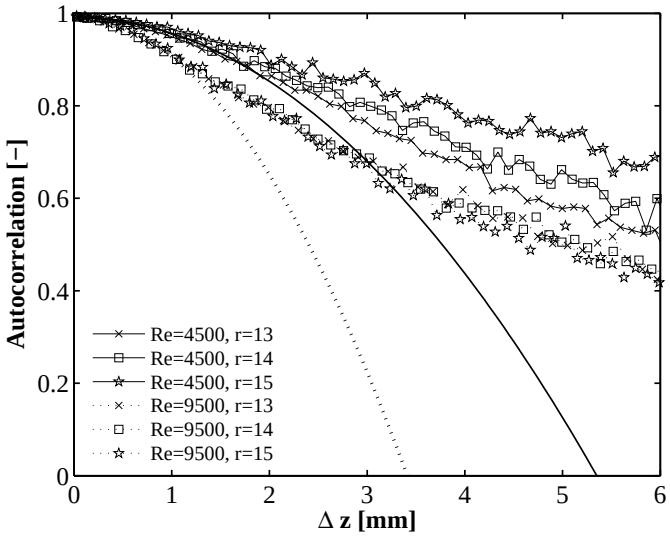

Figure 2.18: Autocorrelation functions, DJHC-I, $\mathrm{Re_{jet}}$=4500 and $\mathrm{Re_{jet}}$=9500. The connected and dotted line represent the parabolic fit through the autocorrelation function at Δz=0 for $\mathrm{Re_{jet}}$=4500 (r=14 mm) and $\mathrm{Re_{jet}}$=9500 (r=15 mm), respectively. These are the locations where the flame resides on average.

equilibrium OH-levels strongly favour locations with low temperature gradients [56]. In order to verify that the lower ignition frequencies indeed originate from higher levels of scalar dissipation, detailed statistics on the history of the scalar field that ignition kernels experience prior to ignition would be needed, an experimental effort not undertaken in this study. However, some insight on the influence of the jet Reynolds number on the turbulent field in the reaction zone would be useful. Therefore, the quantity $\overline{(\partial u_z'/\partial z)^2}$ was determined from LDA measurements by first computing the autocorrelation function (acf) of the axial velocity fluctuations and then invoking Taylor's hypothesis to convert time delay into spatial separation [57]. The resulting acfs that were measured at several radial locations in the DJHC-I flame at z=120 mm for $\mathrm{Re_{jet}}$=4500 and $\mathrm{Re_{jet}}$=9500 are shown in Fig. 2.18.

The intercept of the parabola with the Δz-axis represents the Taylor length scale λ which is related to the strain rate as in

$$\overline{\left(\frac{\partial u'}{\partial z}\right)^2} = \frac{\overline{u'^2}}{\lambda^2}. \tag{2.12}$$

The resulting values for the Taylor length scale are listed in table 2.3. The Taylor length scale decreases (and the variance of the velocity fluctuations increases) with increasing Reynolds number. This is clear evidence that the mean strain rate in the vicinity of the reaction zone is much larger at the higher jet Reynolds number. Both the impact of jet Reynolds numbers on ignition frequency densities in the DJHC-V flames as shown in Fig. 2.17 and

	Re_{jet}=4500			Re_{jet}=9500		
r [mm]	13	14	15	13	14	15
$\overline{u}$ [ms^{-1}]	5.95	5.42	5.31	7.65	6.57	5.99
$\sqrt{\overline{u'^2}}/\overline{u}$ [-]	18.6 %	14.8 %	12.7 %	31.3 %	30.6 %	26.4 %
λ [mm]	$4.8[\pm0.2]$	$5.4[\pm0.3]$	$5.9[\pm0.3]$	$(3.8[\pm0.2])$	$(3.4[\pm0.2])$	$3.4[\pm0.2]$

Table 2.3: Flow characteristics in DJHC-I flames at three radial locations for Re_{jet}=4500 (Dutch natural gas) and Re_{jet}=9500 (fuel II).The Taylor length scales between parentheses should be addressed with some care because of the high turbulent intensity (above 30%).

the hindered kernel growth as was evident in Fig. 2.15 can therefore be linked to changes in the turbulent flow field.

2.3.8 Evaluation and implications on lift-off height

In the analysis of the mechanisms governing lift-off, the function $b_2(z,t)$ was considered to be the result of a simple stochastic process, namely that of randomly occurring local events generating infinitesimal ignition kernels with an expected flame growth that is linear in time, determined from the flame transfer probability function P_{tr}. This probability P_{tr} was assumed to be independent of the axial location z in the stabilisation region. Several deviations from the idealised process can be witnessed however. Ignition kernels do not appear as points, but as small regions in space, with a fast, but not instantaneous, transition from a non-burning to a burning state. Ignition events are unlikely to be statistically independent, as occasionally successive ignition events are witnessed in a certain region.

Although these deviations will certainly have an influence, the essential features of the flames (for instance as shown in Fig. 2.15) strongly resemble those of the proposed process. Stabilisation by flame propagation, which forms the basis of most theories on lift-off in turbulent non-premixed flames, as the dominant mechanism is out of the question, because the flame speed at the trailing edges is insufficient to maintain the flame base at a fixed point (see Fig. 2.14). This is not to say that the flame speed is irrelevant, since it affects the growth of flame pockets and thereby the lift-off height.

Until this point, the function b_2 was used to extract information on the ignition and growth statistics. The reverse direction is now taken, showing how h_2 and h_1 depend on those statistics. Starting from Eq. (2.10), and taking the inverse of the gradient of P_{b2} at h_2 proportional to $L_{1/2}$, the following expression is obtained:

$$h_2 = z_{\mathrm{b;min}} + k_2 \left[\Phi \left\langle f_{\mathrm{ign;2}} \right\rangle\right]^{-1/2} , \tag{2.13}$$

with k_2 a non-dimensional prefactor. To derive an expression for h_1, not the expected number of ignition events per time per axial length is needed, but those per time per surface

area (presumably the iso-surface of the most reactive mixture fraction), because the flame propagates on a surface (the iso-surface of stoichiometry). This frequency density per surface area $f_{ign;1}$ scales as $f_{\mathrm{ign};2} r^{-1}$, with r the characteristic radius of the axisymmetric flame surface. As the convolution is now performed over a surface and over time (instead of over a length and over time, as in Eq. (2.6)), the relation between h_1 and the ignition and transport properties becomes more complex. An additional non-dimensional parameter should be introduced, for instance $\frac{v_{\mathrm{front}}}{v_{\mathrm{back}}}$. On dimensional grounds we therefore expect:

$$h_1 = z_{\mathrm{b;min}} + k_1 \left[\Phi \left\langle f_{\mathrm{ign};1} \right\rangle\right]^{-1/3} f\left(\frac{v_{\mathrm{front}}}{v_{\mathrm{back}}}\right) , \tag{2.14}$$

with k_1 a non-dimensional prefactor. Note that, as the values of $P_{b1}(z)$ can never exceed those of $P_{b2}(z)$, h_1 must always exceed h_2. This imposes limits on the validity of Eq. (2.14), related to the ratio of the axial height of the considered region and the circumference of the considered flame surface. Solving the exact equation of P_{b1} for pockets growing with fixed speeds on a cylindrical surface shows that the function $f\left(\frac{v_{\mathrm{front}}}{v_{\mathrm{back}}}\right)$ is strictly decreasing in the part of its domain exceeding one. The trends of h_1 and h_2 as a function of jet Reynolds number -initially, both decrease by similar degree whereas at higher jet Reynolds numbers h_1 increases much stronger than h_2- can now be understood through these arguments, as at low jet Reynolds number mainly $z_{\mathrm{b;min}}$ is affected whereas at higher Reynolds numbers the different scalings cause h_1 and h_2 to diverge.

2.4 Conclusions

By analysing high-speed recordings of luminescence in the visible and near UV-part of the spectrum, the lift-off behaviour of flames burning in a hot and diluted coflow was studied. Analysis of the luminescence images showed that the physical mechanisms governing the lift-off process in jet-in-hot-coflow flames and conventional lifted flames are very different. This difference is reflected in the trends for lift-off height as a function of jet Reynolds number, which are completely dissimilar. Instead of flame propagation, ignition kernel generation by autoignition followed by convection and growth are responsible for flame stabilisation. In order to quantify the findings, the ignition process was reduced to two parameters: the axial location where ignitions first occur $z_{\mathrm{b;min}}$ and a mean ignition frequency density in the stabilisation region $\left\langle f_{\mathrm{ign};2} \right\rangle$. The axial flame growth could be described by a single parameter Φ. Based on observations and dimensional reasoning, the lift-off height follows a scaling rule as described by Eq. (2.14).

Addition of higher alkanes and increasing the coflow temperature have a similar effect. Both reduce the chemical timescale, leading to a lower $z_{\mathrm{b;min}}$ and higher ignition frequencies $\left\langle f_{\mathrm{ign};2} \right\rangle$, reducing lift-off height. The influence of fuel composition or coflow temperature on flame pocket speeds is relatively small. The effects of jet Reynolds number on the parameters are more intricate. An increase in Reynolds number from 3000 to 5000

lowers in all cases the location of first ignition $z_{\mathrm{b;min}}$. This is likely related to the faster entrainment of the hotter part of the coflow for increasing Reynolds numbers. An increase in jet Reynolds number leads to significantly higher mean strains of the axial velocity component at the location of the reaction zone, as shown by the decrease in the Taylor length scale. At jet Reynolds numbers exceeding 5000, this is accompanied by diminishing ignition frequencies in the flames burning in the colder coflow, while in all flames the growth of newly formed ignition kernels is hindered. Extinction of ignition kernels is occasionally witnessed at the highest Reynolds numbers. A trend seen in both $z_{\mathrm{b;min}}$ and $\langle f_{\mathrm{ign;2}} \rangle$, and consequently in the lift-off height, versus the jet Reynolds number is that increased levels of turbulence hinder the autoignition process more strongly in flames with slower chemistry.

CHAPTER 3

Role of entrainment in the flame stabilisation

The aim of the research on the Delft-jet-in-hot-coflow (DJHC) burner is to gain understanding in the interplay of turbulence and chemistry in conditions as encountered in devices operating in flameless combustion mode, and to test the validity of numerical models when applied to these flameless combustion conditions. Datasets on velocities, temperatures and qualitative OH data of several Dutch natural gas flames in the DJHC burner have been obtained and are discussed in this paper. It was found that the mean velocity and turbulent stresses are not significantly affected by the chemical reactions, which is in line with the very moderate increase of mean temperatures in the flames. Even at heights where flame structures are present, peak temperatures do not always approach the adiabatic flame temperature. With both flame luminescence and OH-PLIF measurements, it is seen that chemical reactions begin to occur at a lower location when the jet velocity (and thereby the jet Reynolds number) is increased. By analysing the velocity and temperature data in the near-nozzle region, the entrainment of coflow fluid into the turbulent jet has been quantified. The increased entrainment of the higher Reynolds number jet, in combination with the positive temperature gradient in radial direction in the near field of the jet, is shown to be responsible for the decrease of the height where reactions start to occur.

3.1 Introduction

By operating furnaces and boilers [11] and also gas turbines [58] in flameless (or MILD) combustion mode, high efficiencies can be combined with very low NO_x emissions. Flameless combustion therefore offers attractive characteristics, from both an environmental and an economic point of view, even more so in the light of the increasingly strict regulations on CO_2 and NO_x [59] emissions. However, large scale implementation of this technique is hampered by the risks associated with adopting a relatively unknown new technique.

The ability to predict (turbulent) flames by computer models can speed up the development and implementation of more advanced combustion techniques [60]. A general insight in the specific demands of numerical models to accurately predict the characteristics (for instance, heat fluxes and emissions) of flameless combustion would therefore be beneficial to its implementation. Several computational studies have been carried out on (semi-)

Published in *Combust. Flame* 158(8) 1553 - 1563, August 2011

industrial-scale setups operating in flameless mode [61, 62, 63, 64]. However, dealing with the complex turbulence-chemistry interaction in this combustion mode accurately and computationally efficiently remains a challenge. Moreover, the reasons for success or failure of particular models are still unclear. This is, at least partially, caused by the limited (optical) access provided by these setups, hindering detailed studies on for instance the statistics of the turbulent flow and temperature field throughout the domain. As a result, there are not many quantities to be used for validation. Given the large number of physical processes occuring in a furnace environment, this makes the isolation and investigation of a single aspect troublesome.

To study the interplay of turbulence and chemistry in more detail, it is therefore advantageous to simplify the geometry, while retaining the physical processes of interest, and to make the setup optically accessible. Research on such prototypical laboratory-scale flames with the level of detail offered by modern laser-diagnostics has resulted in progress in the area of turbulent combustion, by providing data for model-validation and/or by the information contained in the experimental data itself [60, 65].

In this light, studying flameless combustion in an open, unconfined setup might give valuable insights, provided that the circumstances resemble those found locally in a furnace. Several laboratory scale jet flames with a vitiated coflow have been developed, most notably the Cabra et al. burner [20], and the Adelaide burner [19].

The Cabra burner was designed to capture the features of recirculation burners. Its most striking feature is the large diameter of its coflow, providing homogeneous boundary conditions over a large range, such that it can be considered a two-stream problem. This burner was not aimed specifically at investigating flameless combustion, and it might be argued that the oxygen mole fraction in the coflow (X_{O2} of 0.15 or 0.12, for the H_2-N_2 and CH_4/air jet flames respectively [37]) is rather high for that purpose. Multiple detailed measurement campaigns have been carried out, providing a comprehensive dataset of single-point scalar statistics [66, 67] and information on velocities [27]. Furthermore, joint temperature, OH, and H_2CO measurements have been performed [28].

The Adelaide burner was designed to study flameless combustion, with low oxygen mass fractions in the coflow (typically 3 to 9%) and a small temperature increase in the reaction zone as a result. Detailed species measurements [19] and also joint temperature, OH, and H_2CO measurements [26] on flames with CH_4-H_2 in the fuel jet have been carried out.

In this paper the detailed results of temperature and velocity measurements in the Delft jet-in-hot-coflow burner are reported, for three different coflow cases (different temperatures and oxygen mass fractions) and jet Reynolds numbers ranging from 2,500 to 8,800. The results are analysed with the previous findings on the flame stabilisation in mind, namely, the flame is stabilised by randomly formed auto-ignition spots that grow while being convected downstream by the mean flow [68]. Datasets of the various flames, containing information on velocities, temperatures, OH-fields and the coflow-composition are available upon request.

3.2 Experimental setup

3.2.1 DJHC-burner

The design of the Delft jet-in-hot-coflow (DJHC) burner is based on that of the Adelaide jet-in-hot-coflow burner. The main difference is that the latter uses addition of N_2 to cool down the coflow whereas the DJHC burner uses cooling of the coflow through radiative and convective heat losses along the burner pipe. Another difference is found in the design of the secondary burner, which allows for the addition of seeding particles in the DJHC burner, to act as tracers in for instance LDA or PIV measurements. The schematic of the burner is shown in Fig. 3.1. The secondary burner, which generates the hot coflow, is a ring-burner. Its design was found to yield an axi-symmetric flame, and it is operated in partially premixed mode (by adding 24 nl/min of air to the fuel stream) to help it stabilise. The secondary burner creates a flame with a length of about 0.4 m. A grid is located 0.11 m upstream of the burner exit plane, to keep the fuel pipe centered and to help the coflow lose heat. The outer burner tube radiates most strongly at the height of the distribution grid, indicating that this cooling mechanism is effective. The central fuel pipe (with internal diameter 4.5 mm) is cooled by constantly flushing air through the concentric cooling air ducts, thus preventing excessive heating of the main fuel jet. The main flow of air passes through the air inlets at the bottom and it is this flow that carries the seeding particles. A z, r-coordinate system is used centered on the exit of the fuel pipe. The velocities corresponding to these directions are u and v, respectively.

3.2.2 LDA system

LDA measurements were performed with a two-component, dual beam TSI-system. The green line (514.5 nm) and blue line (488 nm) of a 10 W Continuum Argon-ion laser were used to measure the axial and radial velocity components directly. Two of the incident beams (one of each color) were frequency pre-shifted over 40 MHz by a Bragg cell to enable the detection of instantaneous flow reversals and stagnant flow. The focusing lens had a 82 mm aperture and a focal length of 250 mm. The length and diameter of the measurement volume were 1.7 mm and 0.12 mm, respectively. The fringe distances for the green and blue channel were 2.6 μm and 2.5 μm. Alumina (Al_2O_3) particles with an average size of about 1 μm were used as seeding particles. Two cyclone-type particle generators were used to seed the air and fuel separately. The generators have a provision that enables the control of the seed density in both the co-flow and in the fuel jet. This provision was used to equalise the seeding density in the both flows, thereby minimizing errors related to so-called conditional seeding. The data rate (number of bursts per second) was used as an indicator, as it is proportional to the fluid density, the velocity magnitude and the seeding density. This proportionality was therefore used to equalize the seeding densities: the ratio of the data rates of the unmixed fuel- and coflow streams was made approximately equal to the ratio of their products of axial velocity and fluid density. The light scattered

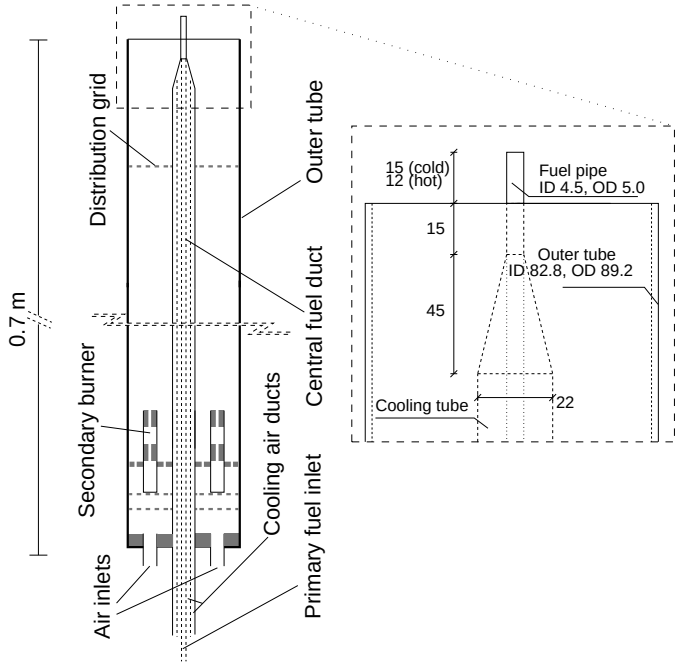

Figure 3.1: Schematic design of the Delft JHC burner, with relevant dimensions in the inset. Two dimensions are given for the vertical extent of the fuel tube above the outer tube, for the cold situation and the hot situation. The difference is due to the uneven thermal expansion of the fuel- and outer tube.

by the seeding particles was collected in back-scatter mode. The photomultiplier output signals were electronically down-mixed, and subsequently fed to a FSA-3000 signal processor to determine the instantaneous velocity of light-scattering particles. All statistics were computed as transit-time weighted results to eliminate the effects of the velocity bias. Autocorrelation functions of the axial velocity component were constructed from time series with 4×10^5 velocity samples that were acquired at a mean data rate of approximately 500 Hz by using the slotting method with local normalisation [46].

3.2.3 CARS system

Temperatures were determined with a CARS system that has been described in detail elsewhere [69]. It is based on an injection-seeded, frequency-doubled Nd:YAG laser (Spectron SL805 SLM), which yields 500 mJ per pulse at 532 nm with a pulse duration of 12 ns at 10 Hz repetition rate. About 80% of the radiation is used to pump a modeless Stokes dye laser (Mode-X ML-3), emitting a broadband profile around 607 nm for Rhodamine 640 in methanol. The remaining 20% of the pump laser travels along a delay line and is split into two beams with equal intensity. The Stokes beam and the two beams at 532 nm are focused by an aplanat lens with a focal length of 300 mm in a planar-boxcars phase-matching con-

figuration. With this configuration, a CARS probe volume of 700 μm length and 35 μm diameter is obtained. The generated CARS radiation is recollimated and combined with an attenuated sample of the Stokes beam on a dichroic beam splitter. The beams are focused onto the entrance of an echelle spectrometer, and their spectra are dispersed on a CCD detector with 1100×330 pixels. The spectra are contained in two strips of 1100 intensity values, which are digitized by an 18-bit AD converter and stored. With Dacapo software [69] the CARS spectrum is referenced to the simultaneously measured Stokes excitation profile and fitted to a library of theoretical, temperature-dependent spectra. The single-shot imprecision of the system is 1% - 4% over a range from 2000 K to 300 K. The inaccuracy is estimated to be 20 K. For each point in space, mean temperatures were determined from the results of 1000 single-shot CARS spectra.

3.2.4 OH-PLIF imaging system

A frequency-doubled, pulsed Nd:YAG laser (Spectra Physics PRO250-10) pumped a Syrah PrecisionScan dye laser using Rhodamine 590 in methanol. The second harmonic radiation from the dye laser was used to excite the $Q_1(6)$ line of the $A^2\Sigma^+$ - $X^2\Pi$ (1,0) transition at 282.927 nm. The UV energy was measured to be about 10 mJ/pulse. Three cylindrical lenses transformed the laser beam into a sheet with a height of approximately 80 mm and an approximate thickness of 200 μm. Fluorescence from the $A^2\Sigma^+$ - $X^2\Pi$ (0,0) and (1,1) transitions at 305-315 nm was collected through a Semrock narrowband filter and a UV-Nikkor 105 mm f/4.5 lens. The images were recorded by an intensified high-speed camera (Lambert Instruments HI-CAM CR) operating at the full resolution of 1280×1024 pixels. A mean off-resonance image was subtracted from the images to determine the mean fluorescence signal. Given a certain point in the flame, the mean OH fluorescence signal depends on the laser sheet intensity and the sensitivity of the camera. This aspect was investigated by traversing the flame vertically through the light-sheet keeping the camera position constant and determining the mean signal strength. It was found that the resulting mean signal strength for a given point in the flame (flame DJHC-I, at $z \approx 90$ mm) is within 30% of the value in the center of the light sheet over a height of 55 mm, which is considered acceptable for the purpose of flame visualisation. To obtain statistics of sufficient quality, 1000 images were recorded for each flame.

3.2.5 Flue gas measurements

Oxygen measurements were performed with a Testo 335 flue-gas analyser, with a specified inaccuracy of $\pm$ 0.20 %. The measured oxygen volume fractions in the coflow were converted to mass fractions using the results from equilibrium chemistry calculations with the species of the detailed Warnatz-mechanism that includes C-2 chemistry (see [70], pg. 333-339).

3.3 Case Description

Three different settings of the secondary burner, affecting mainly the coflow temperature, were used. The resulting coflow properties are summarised in Table 3.1. The coflow properties (velocity, temperature and oxygen mass fraction) vary over the cross-section. The table gives the maximum of the mean temperature profile measured at z=3 mm. The reported O_2 mass fraction is mass flux-averaged.

Under adiabatic and isobaric circumstances the total (sensible plus chemical) enthalpy is unaffected by chemical reaction, and as such it is a conserved quantity. The heat losses of the coflow bring about an enthalpy deficit: a difference between the adiabatic total enthalpy and the actual total enthalpy. As the enthalpy deficit of the coflow is carried to the flame zone, lower-than-adiabatic flame temperatures (of cold air with cold fuel) are expected. The enthalpy deficit of a stoichiometric mixture of fuel and an oxidiser that consists of flue gases can be expressed as a function of the mixture fraction of the flue gases ξ^O, the stoichiometric mixture fraction ξ_{st} (both mixture fractions based on the fresh fuel and air streams), and the enthalpy deficit of the oxidiser Δh^O:

$$\Delta h\left(\xi_{st}\right) = \frac{1-\xi_{st}}{1-\xi^O}\Delta h^O \ . \tag{3.1}$$

Because more heat is lost by radiation of the outer tube when the coflow is hotter, the adiabatic flame temperature is lowest in the DJHC-I case. The adiabatic flame temperatures reported in Table 3.1 are based on equilibrium chemistry calculations, using the measured coflow properties at r=20 mm.

The fuel used in the central jet was Dutch natural gas which has an approximate composition of 81% methane, 4% ethane, 14 % nitrogen and 1% higher alkanes, by volume. Its adiabatic flame temperature in ambient air is 2210 K. Different mass flows were used in the fuel jet, namely 10.7, 16.1 and 30.0 $\mathrm{nl/min}$ resulting in jet Reynolds numbers between 2,500 and 8,800, based on the bulk velocity of the fuel and the density and dynamic viscosity of Dutch natural gas at the estimated fuel temperature at the nozzle exit. These temperatures have been determined using mass conservation, by comparing the measured mass flow and the integrated volume flow at the nozzle exit, from which the density and thus the temperature follows. The reason for taking this approach rather than using the temperature data directly is the quality of the CARS signal obtained close to the fuel pipe exit. Here, the N_2-CARS spectrum is obscured by the strong non-resonant methane signal. In addition, vibrational CARS suffers from increasing imprecision at lower temperatures.

The jet Reynolds numbers are somewhat limited in magnitude. Though this is generally not advantageous for RANS calculations, it might on the other hand be attractive for LES studies. Measurements were done on a selection of the possible combinations of coflow

	Sec. fuel [nl/min]	Tot. air [nl/min]	T_{max} [K]	$Y_{O2;av}$ [-]	Δh^O_{20} [J/kg]	ξ^O_{20} [-]	$\xi'_{st;20}$ [-]	$T_{ad;20}$ [K]
DJHC-I	16.1	224	1540	7.6%	$-4.4(5) \times 10^5$	0.052(1)	0.019	1950
DJHC-V	15.3	231	1460	8.8%	$-4.0(5) \times 10^5$	0.048(1)	0.024	1980
DJHC-X	14.2	239	1395	10.9%	$-2.8(5) \times 10^5$	0.042(1)	0.029	2050

Table 3.1: Characteristics of the coflow stream of the studied DJHC flames. The amount of natural gas to generate the coflow and the total amount of air (premixed and non-premixed) are given in columns two and three. $T_{max;co}$ is the maximum coflow temperature, whereas $Y_{O2;av}$ is a mass flux weighted average between r=2.5 mm and r=35 mm, at z=3 mm. The subscript "20" denotes properties evaluated at r=20 mm. The mixture fraction ξ^O_{20} is based on the inlet streams of the burner (normal air and natural gas), whereas $\xi'_{st;20}$ is the rescaled stoichiometric mixture fraction, of a mixture with the coflow at r=20 mm as oxidiser and natural gas as fuel. The uncertainty of the last digit in the values for enthalpy loss and mixture fraction are given in parentheses.

$\dot{M}_{\mathrm{jet}}$ [nl/min]	10.7	16.1	30.0
DJHC-I	2500 (470 K) [1]	4100 (430 K)	8800 (360 K)
DJHC-V		4600 (380 K) [1]	
DJHC-X		4600 (380 K)	

Table 3.2: Jet Reynolds numbers with fuel temperatures between parentheses, of the combinations of different coflows and jet mass flows that have been fully studied, with both LDA and CARS. For Dutch natural gas, one normal liter corresponds to 0.833×10^{-3} kg. The relative uncertainty in the fuel temperature is estimated at $\pm 5\%$, the uncertainty in the Reynolds numbers is estimated at $\pm$ 200 for the Re=2,500 and 4,100 cases, and $\pm$300 K for the other cases. The default traverses are at z=3, 15, 30, 60, 90, 120 and 150 mm (radial traverses) and a centerline traverse. The cases superscripted with [1] have a reduced number of measurement locations with the traverses at z=15, 30 and 150 mm and the centerline traverse omitted.

cases with jet mass flows. The studied combinations are indicated in Table 3.2, along with their jet Reynolds numbers and fuel temperatures. The higher and lower values of the jet Reynolds number were only fully studied with LDA and CARS in the DJHC-I flames.

The profiles of mean axial velocity of the hot coflow and the fuel jet are shown in Fig. 3.2. The profiles of temperature and oxygen content are shown in Figs. 3.3 and 3.4. The jet Reynolds number does not influence the oxygen mass fraction nor the temperature significantly at z=3 mm. In both the temperature and oxygen mass fraction profiles, asymmetries are seen that exceed the inaccuracy of the measurements. The maximum difference between the oxygen mass fraction at the left and right side is 0.8%, whereas the left-right deviation of the peak temperature is between 20 and 40 K. With the current design, asymmetries of this magnitude cannot be avoided.

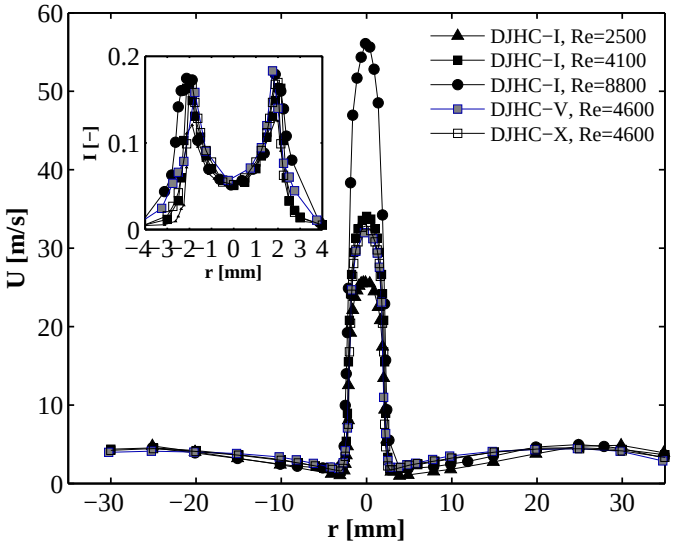

Figure 3.2: Axial velocities at z=3 mm, as measured with LDA. The inset shows the turbulence intensity, calculated as $I = \left(\overline{u'u'} + 2\overline{v'v'}\right)^{1/2} / U_0$, with U_0 the centerline velocity at the nozzle exit.

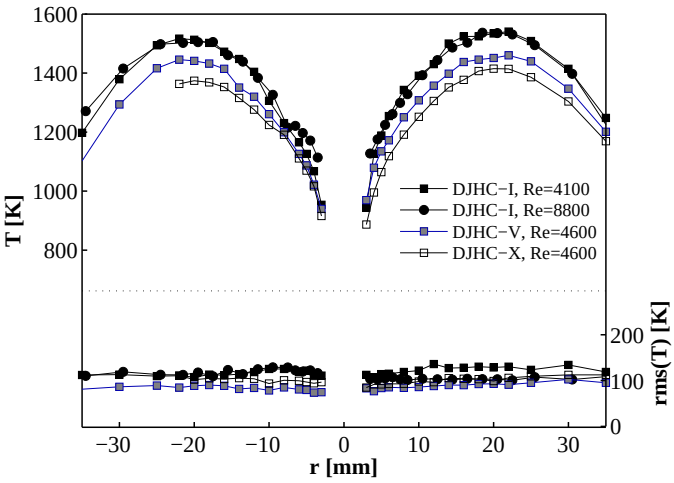

Figure 3.3: Mean and RMS of temperature at z=3 mm, measured with CARS.

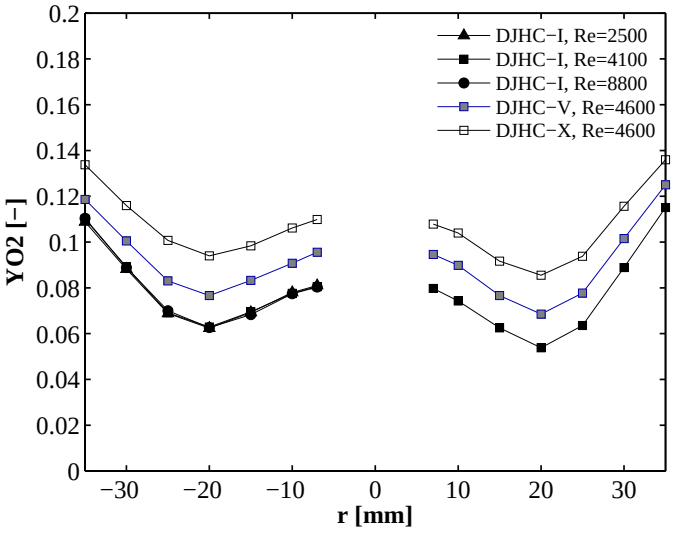

Figure 3.4: Oxygen mass fractions at z=3 mm, measured with a flue gas analyser.

3.4 Visual and OH-LIF observations

The visual appearance of several DJHC flames is shown in Fig. 3.5. As a reference, the bottom right image shows a conventional lifted flame with a jet Reynolds number of 5,000 and a coflow velocity of 0.5 m/s. All pictures were taken with identical exposure time, CCD sensitivity and aperture. The jet-in-hot-coflow flames have considerably weaker flame luminescence. In the DJHC-X flame, hardly any flame luminescence is seen below z=150 mm suggesting that little chemical reactions occur in this region. This is confirmed by OH-PLIF observations, and it makes this flame suitable as a comparison case to the reacting flames.

Figure 3.6 shows the lift-off heights based on chemiluminescence images obtained with the intensified high-speed camera, with the procedure outlined in [68]. The lift-off heights initially show a decreasing trend as function of the jet Reynolds number. A similar trend can be seen in the Adelaide JHC burner in the cases with 3% oxygen in the coflow [26]. It has been demonstrated that the decrease in lift-off height is related to the lower location of first occurence of ignition kernels, denoted with $z_{\mathrm{b;min}}$ [68]. Both the variation in lift-off height h_1 and $z_{\mathrm{b;min}}$ with the jet Reynolds number are shown in Fig. 3.6.

A striking fact is that the initial decrease for all cases is identical. Apparently, the mechanism responsible for lowering the lift-off heights has equal strength in all three coflow cases. It is therefore expected that changes in the flow field are responsible. This aspect will be investigated further in Section 3.7.

The OH-PLIF images in Fig. 3.7 were constructed by taking the root mean square (RMS) of the recorded intensities. By taking the RMS value of the OH-PLIF signal, rather than the mean, the occasional appearance of flame pockets at the base of the flame is

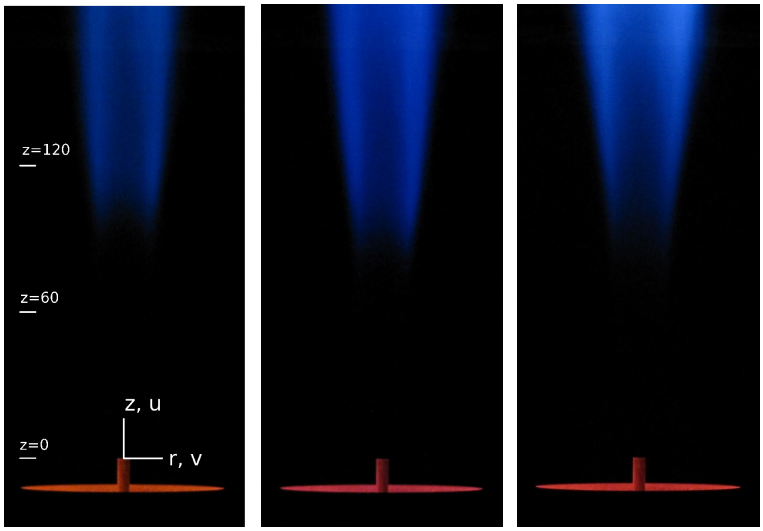

(a) DJHC-I Re 2.5K (b) DJHC-I Re 4.1K (c) DJHC-I Re 8.8K

(d) DJHC-V Re 4.6K (e) DJHC-X Re 4.6K (f) lifted Re 5K

Figure 3.5: Images of the DJHC-flames and a conventional lifted flame, all with 0.5 sec exposure time and identical aperture. The top of the photograph is in each case at around z=180 mm. The coordinate system is indicated in Fig. 3.5a.

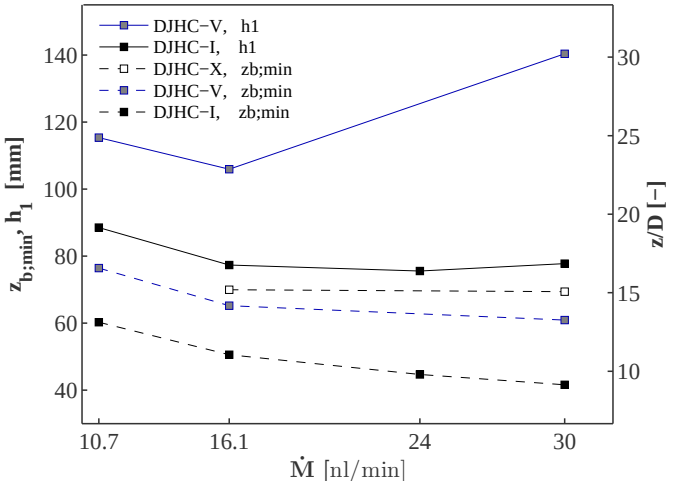

Figure 3.6: Lift-off heights (continuous lines) and location of first occurrence of ignition kernels (dotted lines) as a function of the jet mass flow (in nl/min). Note that the flame DJHC-X has a lift-off height exceeding 150 mm in all cases.

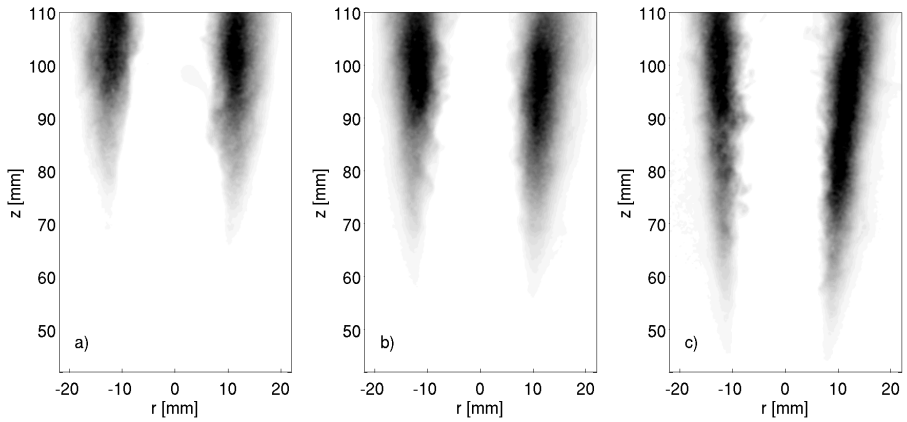

Figure 3.7: RMS values of the OH-fluorescence signal in the flame stabilisation region, DJHC-I, $\mathrm{Re_{jet}}$=2,500 (a), $\mathrm{Re_{jet}}$=4,100 (b) and $\mathrm{Re_{jet}}$=8,800 (c).

clearly highlighted. The axial location where flame structures begin to affect significantly the RMS value of the OH signal, decreases by approximately 20 mm from $\mathrm{Re_{jet}}$=2,500 to $\mathrm{Re_{jet}}$=8,800 in flame DJHC-I. This is consistent with the earlier observations based on flame luminescence regarding the influence of the jet Reynolds number on $z_{b;\mathrm{min}}$. The mean OH signal at z=90 mm peaks at a radius of approximately 13 mm for the lowest jet Reynolds number and at approximately 12 mm for the highest jet Reynolds number.

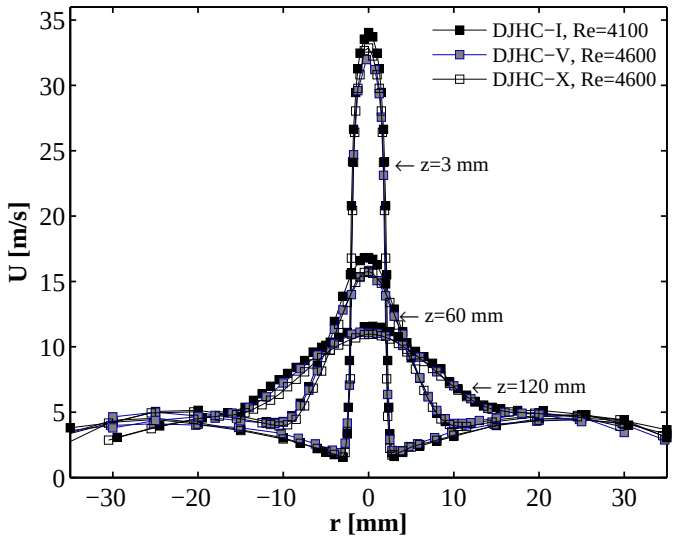

Figure 3.8: Mean axial velocities at z= 3, 60 and 120 mm for the three different coflow cases, at a jet Reynolds number of 4,100 (DJHC-I) and 4,600 (DJHC-V and DJHC-X).

3.5 Flow field

3.5.1 Mean velocities and Reynolds stresses

Figure 3.8 shows the mean axial velocity profiles for the three coflow cases with a jet mass flow of 16.1 nl/min at z=3 mm, 60 mm and 120 mm (z/d= 2/3, 13 1/3 and 26 2/3, respectively). Although flame DJHC-I has a lower lift-off height than flame DJHC-X (observed in both CARS measurements and visually), this is not reflected in a difference in the mean velocity profiles. From this it can be concluded that the effect of combustion on the mean flowfield in the lower portion of the flame is minimal.

In Fig. 3.9, the centerline decay of the mean axial velocity profile (normalised by the jet exit velocity U_0 for two coflow cases and different jet Reynolds numbers) are presented. Whereas the difference in velocity field between the coflow cases is small, there is a clear distinction between the low- and high jet Reynolds number case. The low Reynolds number case shows a weaker initial decay but catches up later, which is also seen in the normalised value of the Reynolds normal stress $\overline{u'u'}$.

The location of maximum shear stress $\overline{u'v'}$ is a useful indicator of the jet width. In the self-similar region of a jet, it peaks at a radius of roughly 0.7 times the jet half-width (the radius where the mean axial velocity is half that at the centerline) [57]. At z=60 mm and 120 mm, the width of the jet of different cases is very comparable, and the shear stress $\overline{u'v'}$ is of similar magnitude when normalised by the jet exit velocity squared (Fig. 3.10).

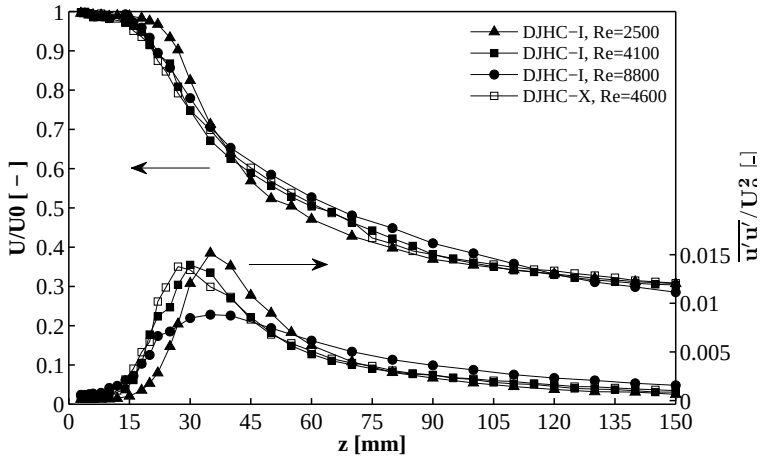

Figure 3.9: Centerline decay of the mean axial velocity, all cases.

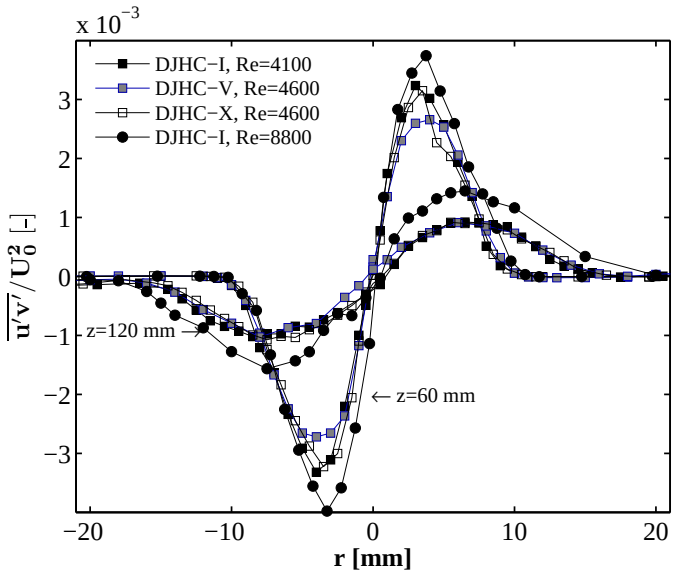

Figure 3.10: The normalised shear stress along radial traverses at z=60 and 120 mm, all cases.

3.5.2 Turbulence length scales

As turbulence dominates the transport of scalars, an adequate description of the turbulent flow field is important. The Eulerian velocity time scales can be determined from a stationary LDA probe by constructing autocorrelation functions of the velocity components. The turbulence intensity on the jet centerline is sufficiently low ($\sqrt{\overline{u'^2}}/U \approx 15\%$) to convert these time-scales to length-scales using Taylor's approximation, as the correction proposed by Lumley [71] on the Taylor length scale is smaller than 10 %. The single point LDA measurements can be used to determine, for instance, integral- and Taylor length scales. The Reynolds number based on the longitudinal Taylor length scale λ_f, $Re_T = \sqrt{\overline{u'^2}}\lambda_f/\nu$ (with ν the kinematic viscosity) forms a useful quantity to compare experimental and numerical data because it can be determined from numerical data as well (LES or DNS). The longitudinal Taylor length scale follows from the following expansion of the spatial autocorrelation function, as function of the axial separation Δz:

$$\rho\left(\Delta z\right) = 1 - \frac{\Delta z^2}{\lambda_f^2} + \mathcal{O}\left(\Delta z^4\right) \tag{3.2}$$

and the transversal Taylor length scale λ_g is defined similarly. These scales are related to the mean square derivatives

$$\overline{\left(\frac{\partial u'}{\partial z}\right)^2} = \frac{2\overline{u'^2}}{\lambda_f^2} \quad , \quad \overline{\left(\frac{\partial v'}{\partial z}\right)^2} = \frac{2\overline{v'^2}}{\lambda_g^2} \; . \tag{3.3}$$

To determine the Taylor-scale Reynolds number, the kinematic viscosity was determined based on equilibrium chemistry calculations (on the centerline, the mixture is still rich and the difference between reacting and non-reacting is minimal). The used kinematic viscosities at z=60 and 120 mm are 8×10^{-5} and 12×10^{-5} m^2/s, respectively. The integral longitudinal length scale was determined by integration of the longitudinal autocorrelation function.

The properties of the flowfield on the centerline at z=60 and z=120 mm are summarised in Table 3.3. The transverse Taylor length scale is smaller than the longitudinal length scale. Note that in isotropic turbulence $\lambda_f = \sqrt{2}\lambda_g$ (see [57], pg. 199). The Taylor length scale grows with increasing distance from the jet exit along with the integral length scale. The ratio between the Taylor and the integral length scales is not observed to decrease significantly with the jet Reynolds number. Scaling arguments (see for instance [57], pg. 200) and measurements (as reported for instance in [72]) suggest an inverse square root relation, but the difference in Reynolds numbers is too small here to be of significance.

To calculate the dissipation of turbulent kinetic energy in general non-isotropic turbulence, twelve different derivative correlations need to be measured, which is practically

Flame	Re	z	U	$\sqrt{\overline{u'^2}}$	$\sqrt{\overline{v'^2}}$	λ_f	λ_g	L	Re_λ	K_1	ϵ
	[-]	[mm]	[m/s]	[m/s]	[m/s]	[10^{-3} m]	[10^{-3} m]	[10^{-3} m]	[-]	[-]	[10^3 m^{2}s^{-3}]
DJHC-I	4,100	60	16.2	2.8	2.2	$1.9[\pm 0.3]$	$1.3[\pm 0.2]$	2.6	7×10^1	1.5	5
	4,100	120	10.9	1.5	1.3	$3.4[\pm 0.1]$	$2.3[\pm 0.1]$	5.0	5×10^1	1.3	0.7
	8,800	60	30.4	5.1	4.1	$1.4[\pm 0.1]$	$1.1[\pm 0.1]$	2.1	9×10^1	1.7	30
	8,800	120	20.1	3.2	2.7	$2.4[\pm 0.3]$	$1.6[\pm 0.1]$	3.9	7×10^1	1.2	6
Lifted	5,000	60	6.6	1.5	1.2	$1.3[\pm 0.4]$	$1.0[\pm 0.3]$	2.9		1.9	
	5,000	120	4.0	0.6	0.5	$2.8[\pm 0.1]$	$1.7[\pm 0.1]$	5.3		1.2	

Table 3.3: Turbulence properties on the centerline at two heights above the jet exit, determined with two-component LDA measurements.

impossible with single two-component LDA. The assumption of local axisymmetry leads to a relaxation of these demands, but derivatives in the radial directions are still needed [73]. As this direction is not aligned with the mean flow, these derivatives can still not be accessed with a stationary probe. Therefore, to get an estimate of the smallest scales, isotropy of the smallest scales will be assumed. As a measure of the anisotropy, K_1 is also given in Table 3.3. This quantity is defined as :

$$K_1 = 2\,\overline{\left(\frac{\partial u'}{\partial z}\right)^2} \Bigg/ \overline{\left(\frac{\partial v'}{\partial z}\right)^2} \tag{3.4}$$

and it is equal to one in isotropic conditions [73]. As can be seen in the table, the deviations from unity are not large at z=120 mm. An estimate of the dissipation rate of turbulent kinetic energy based on the expression for isotropic turbulence ($\epsilon = 30\,\nu\overline{u'^2}/\lambda_f^2$) is included in the final column. The Kolmogorov length-scale $\lambda_K = \left(\nu^3\epsilon^{-1}\right)^{1/4}$ is in the order of 1×10^{-4} m.

3.6 Temperature field

The high-speed intensified imaging reported in [68] described the probability of the presence of flame structures as a function of axial height, for various flames. This probability was expressed in the parameter denoted with P_{b1}. This parameter will be used in this Section for comparison, a discussion on its definition is provided in the aforementioned paper. The temperature measurements at z=60 mm (not shown) show no sign of any reactions. On the other hand, at z=90 mm a mild temperature increase can be observed in the DJHC-I flame, see Fig. 3.11.

This increase is hardly noticeable in the mean, but is visible in the temperature RMS, and, most notably, in the peak temperature T_{99}. This peak temperature is defined as the temperature where the cumulative density function exceeds 99% (it is the 99th percentile). Although flame structures are present during approximately 80 % of the time at z=90 mm ($P_{b1} \approx 80\%$), the peak temperature T_{99} does not exceed 1770 K, relatively far from the estimated adiabatic flame temperature of 1950 K. Comparing the locations of the peaks in T_{99} in Fig. 3.11 (at a radial location of around 12 mm, which is in agreement with the location of the flame as observed in the OH-PLIF measurements) with the measured shear stress profile at z=90 mm (which peaks at a radius of 5 mm), the reaction zone clearly resides outside the region of most intense turbulence. This can be understood from the value of the stoichiometric mixture fraction, being even lower than that of a flame of Dutch natural gas in air (around 0.02 instead of 0.07) due to the reduced oxygen content of the coflow.

At z=120 mm, the presence of the reaction zone of flame DJHC-I is visible in the mean temperature profile, whereas this is less clear in flame DJHC-V, see Fig. 3.12. An interesting feature is that T_{99} of flame DJHC-I increases by some 140 K from z=90 to z=120 mm,

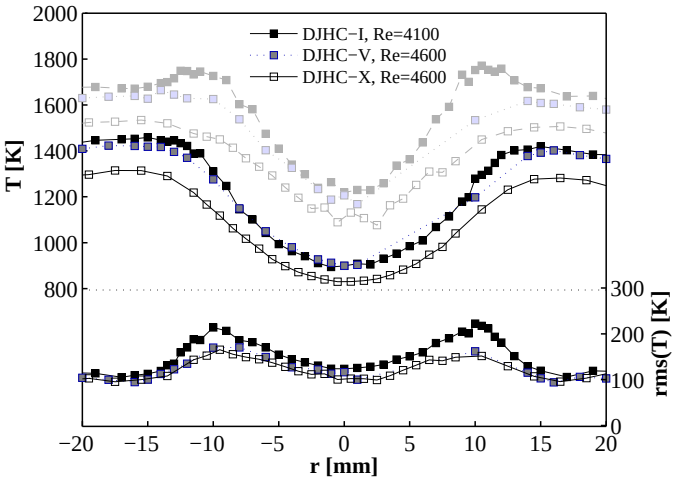

Figure 3.11: Mean and RMS of temperature in flames DJHC-I, DJHC-V and DJHC-X at z=90 mm. The fainter upper curves indicate T_{99}, the 99 percentile of temperature, to indicate measured peak temperatures.

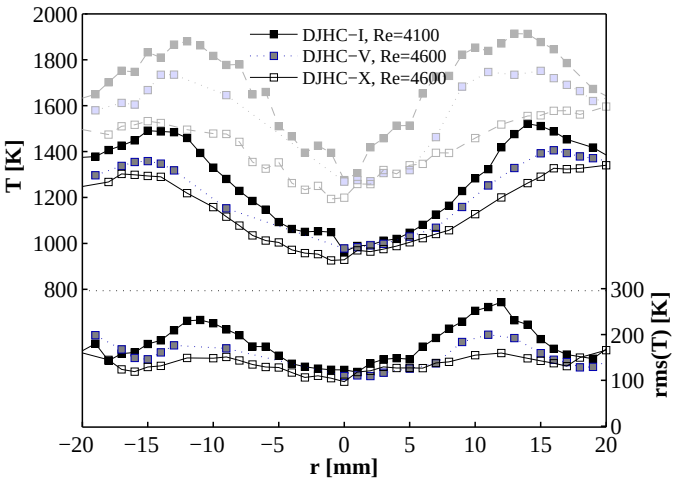

Figure 3.12: Mean and RMS of temperature in flames DJHC-I, DJHC-V and DJHC-X at z=120 mm. The fainter upper curves indicate T_{99}, the 99 percentile of temperature.

to around 1910 K. As the flame probability P_{b1} is already close to 100% at z=90 mm, this increase must be due to an evolution of the flame temperature. Taking into account the convective velocity of the flame pockets, which is roughly 5 m/s [68], the flame pockets have a lifetime that is around 6 ms longer at z=120 mm than at z=90 mm. Apparently, this time is needed for the flame pockets to reach temperatures close to equilibrium.

The DJHC-V flame does not, despite its higher adiabatic flame temperature, show higher mean or peak temperatures at z=120 than DJHC-I. Flame structures are also present

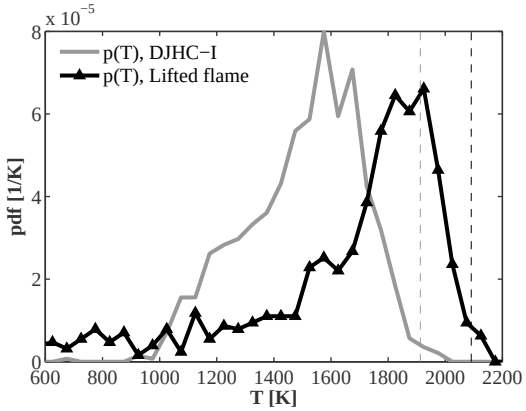

Figure 3.13: Pdf of temperature $p(T)$ (points lie on the center of the bins) for the DJHC-I flame ($\mathrm{Re}_{\mathrm{jet}}$=4,100, at z=120 mm, r=14 mm) and a lifted flame ($\mathrm{Re}_{\mathrm{jet}}$=5,000 at z=90 mm, r=15 mm), the vertical dashed lines denote the T_{99} values. The number of measurements is 951 (DJHC-I) and 772 (lifted flame).

regularly here ($P_{b1} \approx 65\%$), another indication that chemistry resides far from equilibrium.

As a reference, temperature statistics were also obtained for a conventional lifted flame with a jet Reynolds number of 5,000, at a height of z=90 mm (which is above the lift-off height) and at the radial location with the highest mean temperature (r=15 mm). The pdf of temperature of this flame is shown together with that of the DJHC-I flame in Fig. 3.13. The peak temperature T_{99} of the lifted flame (indicated with the right dotted line) is 2100 K. When rescaled between the mixing temperature and the adiabatic flame temperature, this is comparable to the T_{99} of DJHC-I at z=120 mm. The temperature distribution of the lifted flame is much wider, containing both colder samples as the reactants are injected at room temperature, and much hotter samples. Fig. 3.14 compares the temperatures at z=90 mm for varying jet Reynolds numbers. Only minor differences can be spotted. The mean temperatures vary insignificantly, the T_{99} values of the lowest jet Reynolds number case are slightly lower, in agreement with its higher lift-off. In the highest jet Reynolds number case, colder temperatures were occasionaly measured at r=-17 mm (2% of the samples were below 1000 K), originating from the ambient air. These are responsible for the increase in the RMS values.

The differences are more substantial at z=120 mm. Figure 3.15 shows that the mean temperatures as well as the peak temperatures are substantially lower in the higher Reynolds number case. The mean temperatures in this case are even lower than those at z=90 mm, which can only be explained by the entrainment of colder coflow air. A stronger departure from chemical equilibrium due to shorter residence time of flame pockets, and possibly the influence of larger strains could form an additional explanation for the fact that the peak temperatures do not exceed those at z=90 mm significantly, as they do in the lower Reynolds number cases. As the influence of ambient air (witnessed as outliers in the pdf's

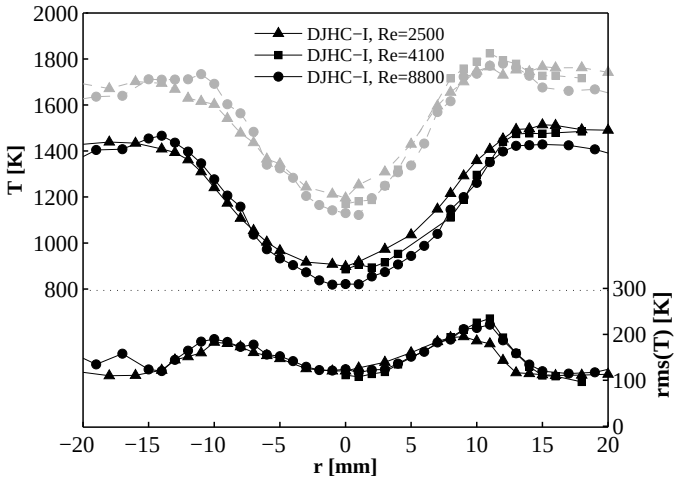

Figure 3.14: Mean and RMS of temperature for three jet Reynolds numbers in flame DJHC-I, z=90 mm. The fainter upper curves indicate T_{99}.

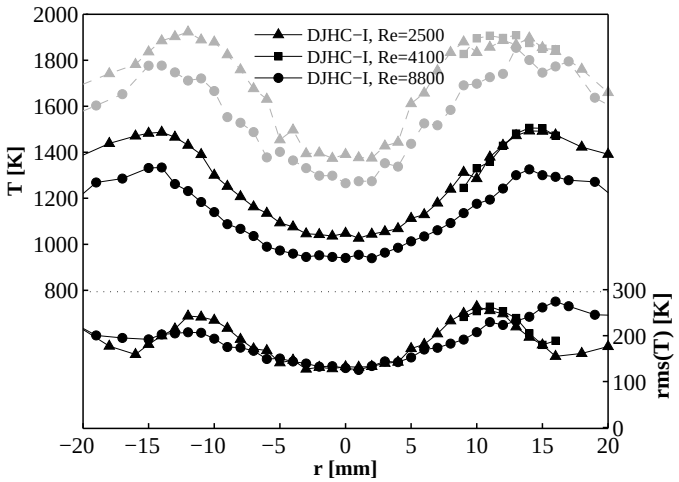

Figure 3.15: Mean and RMS of temperature for three jet Reynolds numbers in flame DJHC-I, z=120 mm. The fainter upper curves indicate again T_{99}.

of temperatures) is present from r=12 mm and up in the high jet Reynolds number case (in the other cases at r=20 mm and up), it is difficult to be conclusive regarding this point.

3.7 Entrainment

A remarkable feature of the studied flames is that ignition events are first observed at lower heights with increasing jet Reynolds number. An explanation for this phenomenon will be provided in this Section. Of interest to this problem are the properties in the mixing layer, located radially somewhere between the jet centerline and the pure coflow fluid outside the jet. Here, mixtures of fuel and coflow fluid with the optimum mixture fraction for fast ignition are formed (in general not equal to the stoichiometric mixture fraction, [74]). The total mass flow in the jet increases in the downstream direction, as more and more coflow fluid is drawn into the jet. Because of this continuous increase in mass flow, the coflow fluid that is entrained by the jet originates from progressively larger radii at $z = 0$ as one goes downstream. If the properties of the coflow are non-constant along the radial direction, the properties of the entrained coflow fluid will then also change in the downstream direction. For the DJHC flames, this means that the fuel stream initially mixes with the colder coflow fluid, originating from small radii at z=0. As more coflow fluid is consumed by the jet, the hotter coflow from larger radii will find its way into the mixing layer at larger heights. The temperature conditional on (the most reactive) mixture fraction will increase in the axial direction and ignition delay times will become sufficiently short for ignition kernels to form in the domain. In this analysis, it is assumed that the temperature of a parcel of coflow fluid as it is entrained is related to the temperature of that fluid parcel when it was at z=0. This is justified by a simple scaling argument: the convective heat flux is much stronger than the diffusive heat flux ($\widetilde{u\,T} \gg u''T''$), since turbulent fluctuations are relatively small in the coflow. Because the length scales for convection (length of streamline) and diffusion (radius of the burner tube) are of similar magnitude, the time scale for turbulent diffusion is much greater than the timescale for convection. As a consequence, temperatures are largely conserved along streamlines in the coflow.

Since the entrainment flux of turbulent jets is proportional to the centerline velocity (see [75], pg. 35), this transport of hotter coflow fluid from larger radii at z=0 toward the jet is augmented when the jet velocity is increased. In the presence of a positive radial temperature gradient of the coflow this results in a faster rise of temperatures conditional on mixture fraction in the axial direction, with ignition at lower axial locations as a result. Note that in this analysis, two important assumptions were made. First of all, details of the mixing process itself are not considered. This is not to say that these complexities (such as the influence of scalar gradients on the mixing and ignition process [45]) are not present, but rather that their influence is overshadowed by the effect of the temperature variations. Secondly, ignition delay times are transformed to ignition delay lengths using a constant velocity, independent of the jet velocity. This assumption is justified by the experimental

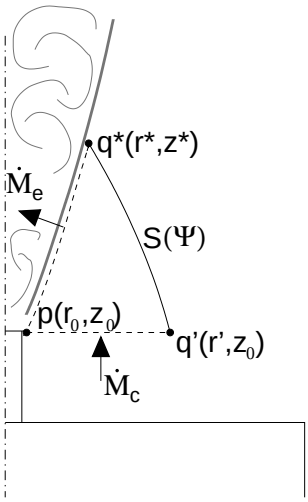

Figure 3.16: Sketch of the jet boundary (curved thick line) and the streamline S. In absence of circulation regions, points q' and q^* share the same streamline S, when the mass flow through the boundary $p-q^*$ (which is the total entrained coflow fluid by the jet between z_0 and z^*) equals the mass flow through the boundary $p-q'$. The thick grey line denotes the boundary between the jet region, where jet and coflow fluid mix, and the coflow region.

finding that the convective velocity of ignition kernels is not strongly affected by the jet velocity, but is mainly determined by the coflow velocity [68].

The transport of coflow fluid toward the mixing region in the jet can be studied quantitatively with the available temperature and velocity data. The task is to find the radial position r' at $z = z_0$ from which the streamline that is entrained at (r^*, z^*) originates, see Fig. 3.16. By definition the mass flow rate through any boundary that runs from a point p to any point q on a streamline S is constant, independent of the choice of q. If the value of the streamfunction Ψ is set to zero at (r_0, z_0), the streamline $S(\Psi)$ in Fig. 3.16 connects points q' and q^* for which $\dot{M}_c = \dot{M}_e = \Psi$.

Now, a criterion is needed to define the interface between the turbulent mixing layer and the coflow stream. This criterion is provided by the turbulent shear stress $\overline{u'v'}$. As demonstrated in Fig. 3.10, the value of this shear stress at z=60 mm quickly approaches zero at the jet edge, enabling the use of a stringent threshold level. The edge of the jet is defined as the radius r^* where $\overline{u'v'}$ is less than 1% of its peak value.

The value of the entrainment mass flow, $\dot{M}_e$, can be obtained by integration along the jet boundary, as was done by Han and Mungal [76]. This requires a careful determination of the angle of the jet boundary, and calculation of the mass flow perpendicular to this boundary. A different approach is taken here, using a control volume that runs from (r_0, z_0) via (r^*, z_0) to (r^*, z^*). The entrained mass flow between $z = z_0$ and $z = z^*$ is the sum of

two integrals, one in radial and one in axial direction:

$$\dot{M}_e(z^*) = 2\pi \left[\int_{r_0}^{r*} \overline{\rho u}\; r\; dr \Big|_{z_0} + \int_{z_0}^{z^*} -\overline{\rho v} r\;\; dz \Big|_{r*} \right] . \tag{3.5}$$

See Fig. 3.16 for a definition of the coordinates r_0, $r*$, z_0 and z^*. The mass flows in Eq. 3.5 are not measured directly. Whether and how these can be reconstructed from the CARS and LDA measurements, depends on the nature of the averages of these measurements. Since the timing of CARS measurements is controlled externally, and the data is gathered independently of processes in the flame, the temperature measurements can be considered to be unconditionally sampled. If temperature variations within the measurement volume can be neglected, the arithmetic mean of CARS measurements therefore corresponds to a Reynolds average. For LDA measurements the analysis is more complicated. In appendix B it is shown that LDA statistics obtained in a variable density flow with application of transit time weighting can be considered to be density weighted. Multiplication of this density weighted mean velocity by the mean density then gives the mean mass flux, as required to calculate Eq. 3.5, since by definition $\overline{\rho}\,\widetilde{u} = \overline{\rho u}$.

This point is not of critical importance, since the fluctuations of density are small. To illustrate this, consider the maximum value of the covariance given by the Cauchy-Schwarz inequality:

$$\left|\overline{\rho' v'}\right| \leq \left(\overline{\rho'^2}\;\overline{v'^2}\right)^{1/2} . \tag{3.6}$$

The density variance can be approximated from the temperature variance using a linearised relation between density and temperature around the mean temperature:

$$\overline{\rho'^2} \approx \left.\frac{d\rho}{dT}\right|_{\overline{\mathrm{T}}}^2 \overline{T'^2} . \tag{3.7}$$

If the measured velocities would in fact be Reynolds averaged, the uncertainty (as in principle, the correlation can have any value between one and minus one) is typically 10 % or smaller.

Approximating the functions in the integrals of Eq. 3.5 linearly between the measurement points, the total entrainment can be calculated. The totally entrained mass flow at several heights is shown in Fig. 3.17. The entrainment of cases DJHC-I and DJHC-X with a jet mass flow of 16.1 nl/min is identical. Furthermore, the higher velocity jet entrains more coflow fluid, as can be expected from a standard entrainment scaling [75]. The data shown in Fig. 3.17 can now be used to estimate the average temperature of the coflow entrained by the jet at different heights.

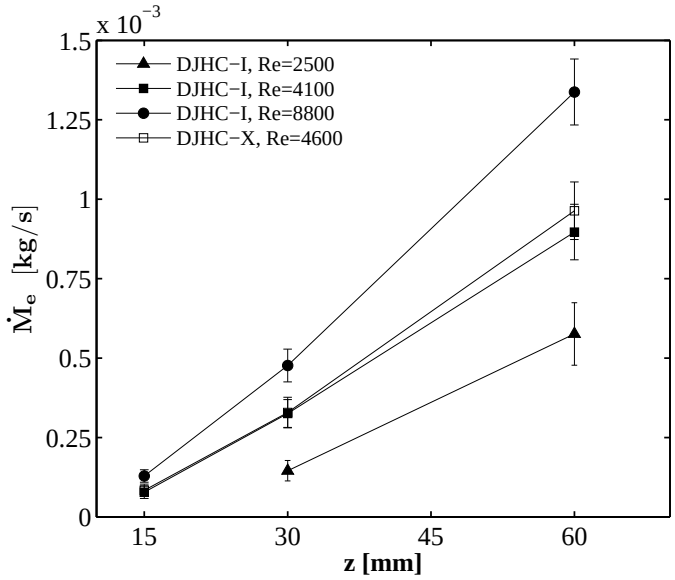

Figure 3.17: The total entrainment $\dot{M}_e$, determined by numerical evaluation of Eq. 3.5, as a function of height z, for four different cases. The errorbars indicate the maximum contribution of the density-velocity covariance calculated with Eq. 3.6.

The values of $T(r)$ as a function of $\Psi_0(r)$, where Ψ_0 is the value of $\dot{M}_c$ at z=3 mm, are plotted in Fig. 3.18. The coflow temperature levels off at around $\Psi_0 = 0.6 \times 10^{-3}$ kg/s, corresponding to $r \approx 15$ mm. The temperature profile is much flatter against Ψ than against r, because the majority of the coflow mass flows through the center and outer part of the annulus.

Comparing now Figs. 3.17 with 3.18, it can be seen that at z=30 mm, the highest jet Reynolds number case starts entraining the hottest part of the coflow (at around 1500 K), whereas this happens at around 20 mm further downstream for the lowest jet Reynolds number case. This magnitude is in agreement with that of the observed decrease in the height where ignition kernels are first formed. The combination of the dependence of the entrainment fluxes on the jet velocity with the positive radial temperature gradient of the coflow therefore forms a sound explanation for the observed initial decrease in lift-off height.

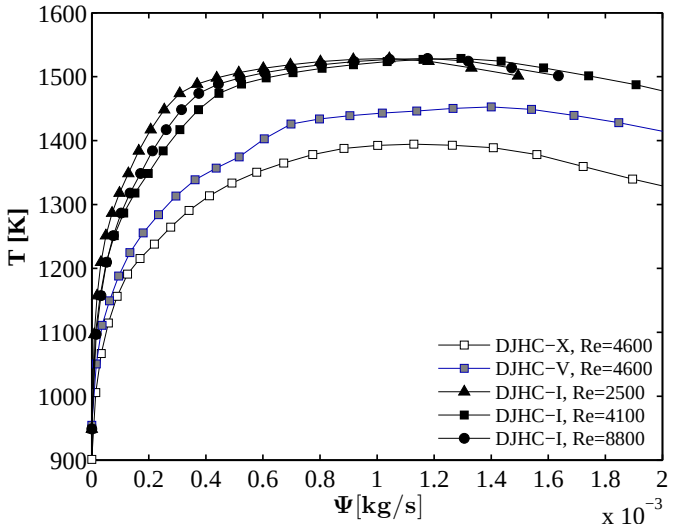

Figure 3.18: Mean temperature as a function of the streamfunction Ψ (set to zero at r=3 mm), at z=3 mm.

3.8 Conclusions

LDA, CARS and OH-PLIF measurements were performed in several jet-in-hot-coflow flames, differing in jet mass flow and coflow temperature. The chemical reactions occurring in these flames were found to have a very weak impact on the velocity field, as the mean velocities and turbulent stresses in the DJHC-I flame are comparable to those of the DJHC-X case, that has a lift-off height exceeding the measurement domain.

In the temperature field, first deviations between the reacting and non-reacting cases were seen at z=90 mm. These differences are not very pronounced in the mean, but are evident both in the RMS values (nearly doubling when reactions start to occur, case DJHC-I vs. DJHC-X), and in the 99 percentile of temperature, T_{99}. The peak temperatures in the DJHC-I, $\mathrm{Re_{jet}}$=4,100 case at z=90 mm are far away from the adiabatic peak temperature whereas those at 120 mm approach this temperature much closer. Considering the fact that flame structures are already present most of the time at a height of 90 mm, this is indicative of an evolution in temperature of flame pockets from the point where they are newly formed to where they have evolved longer in time (a difference in time of around 6 ms). In other flames (DJHC-I with $\mathrm{Re_{jet}}$=8,800 and the colder coflow flame DJHC-V with $\mathrm{Re_{jet}}$=4,600), peak temperatures stay remote from the adiabatic flame temperatures, also at z=120 mm.

It was observed with both high-speed flame luminescence and OH-PLIF measurements that the location of first chemical reactions decreases with increasing jet velocity. This is by no means a general characteristic of jet-in-hot-coflow flames, but is related to the positive radial temperature gradient in the coflow of the DJHC-burner. From a quantitative analysis of the entrainment in the near-nozzle region, it was concluded that the hottest part

of the coflow finds its way into the jet shear layer at an axial location that is around 20 mm lower going from the lowest to the highest jet values of the jet mass flow. This distance agrees with the observed decrease. The rate with which hot oxidizer fluid is transported towards the edge of the jet where mixing takes place is thus an important factor in the flame stabilisation of the flames considered. This result is in line with the dominant role of autoignition in the stabilisation of jet-in-hot-coflow flames and the known sensitivity of autoignition processes to temperature.

In the $\mathrm{Re}_{\mathrm{jet}}$=8,800 case, at z=120 mm, cold outer air is occasionally entrained in the location where the flame resides as seen by outliers in the temperature pdf's, highlighting the necessity of using a larger diameter coflow when larger jet Reynolds numbers or higher locations are to be studied.

CHAPTER 4

Ignition of impulsively started fuel jets

The ignition of impulsively started jets of natural gas in a hot coflow has been studied, with the aim of gaining insight into the processes that occur in a furnace equipped with regenerative burners. The development of the velocity field was measured in a time resolved manner with Laser Doppler Anemometry (LDA) and Particle Image Velocimetry (PIV) at 10 kHz. Furthermore, simultaneous PIV and Planar Laser Induced Fluorescence of the OH-radical (OH-PLIF) were employed in combination with high-speed recordings of flame luminescence to map the ignition sequence. A characteristic feature of the impulsively started jets was that the turbulent phase was preceded by a laminar phase, during which no significant amount of combustion took place. After the sudden transition towards a turbulent state, significant ignition delay times were observed. As demonstrated in earlier work [77], the radial temperature gradient of the coflow makes the entrainment of coflow fluid into the jet region very important to the jet stabilisation, influencing strongly the lift-off height. Using the time-resolved PIV data, the transport of fluid parcels in the coflow region was monitored during the transition towards the turbulent state. This transport is governed by the low velocities of the coflow and as a result, ignition delay times and the time until a steady state of combustion is attained are not solely related to jet time scales. It is thus concluded that in the presence of large-scale inhomogeneities, ignition delay times are several times greater than the time needed for the velocity field of the jet to reach its steady turbulent state.

4.1 Introduction

Recycling of flue gas heat is a prominent feature of flameless combustion. Rather than having the heat escape from the furnace along with the flue gases, the heat is used to preheat one or both reactant streams [13]. This preheating can be achieved by a recuperative system which operates by continuously exchanging heat between outgoing and ingoing flows. A more efficient solution is offered by a regenerative system, characterised by two alternating configurations [11]. During the first part of the regenerative cycle, one set of burners supplies reactants to the furnace and the other set of burners acts as flue gas exhausts. Regenerators in the exit burners (for instance ceramic honeycombs) extract heat

Published in *Combust. Flame* 159(2) 697 - 706, February 2012

from the exhaust gases, while regenerators in the supplying set of burners feed the previously extracted heat to the reactant stream. In the second part of the cycle, the roles are reversed. This complete cycle has a period of typically twenty seconds, introducing an inherent unsteadiness in the furnace. Since the flow field can change as frequent as once in every ten seconds, transient phenomena could be of significance for the combustion process as a whole.

Whereas experimental and numerical studies of transient processes in engines are common practise [78, 79], transient phenomena in regenerative furnaces in flameless mode have not yet been addressed in detail. The lack of optical accessibility of large setups prohibits the use of laser diagnostics and measured quantities are usually not well resolved in space or time. Detailed data on transient processes in a furnace are therefore simply unavailable. The simplified case of a transient jet in a hot, unconfined coflow is much easier to study experimentally. Nevertheless, studies on transient behaviour of such flames are also sparse in literature.

Non-reacting transient turbulent jets have been studied more extensively, a summary is provided by Joshi and Schreiber [80]. An important result is the square root dependence of the jet penetration with time [81]. Atassi et al. [82] showed that a sudden decrease in the exit velocity of a turbulent jet leads to disturbances on the centreline at large axial distances with a duration of the order of the local time scale (determined by the local jet diameter and centreline velocity). Cossali et al. [83] examined the evolution of the entrainment of an impulsively started turbulent jet in its near field ($z/D < 22$), with D the nozzle diameter. The centreline velocity was seen to evolve faster than the entrainment flux, which took about 7 ms to reach the steady state within the considered domain. When normalised, this corresponds to about 180 jet time scales (the nozzle diameter divided by the jet velocity).

In the context of ignition in Diesel-like conditions, Naber et al. [84] investigated the influence of fuel composition on ignition delays of autoignition and found that the presence of higher alkanes strongly influenced ignition delay times. More recently, Fast et al. [85] carried out a comprehensive study on ignition of dimethyl ether (DME) jets injected into a high-pressure vessel containing nearly stagnant heated air. The development of the mixture fraction field, the velocity at the nozzle exit and heat generation (by means of high-speed Schlieren imaging) was recorded, relative to time of injection. This phase-resolved data revealed a two-stage ignition sequence. The first stage was characterised by a moderate temperature increase over a large spatial extent, followed by a second stage of more intense heat release, after which a non-premixed flame was formed. Ignition delay times were found to be largely unaffected by variations in jet velocity, and mainly dependent on chemical kinetics.

In this work, the ignition behaviour of transient jets is studied in the Delft jet-in-hot-coflow (DJHC) burner. This setup was designed to study turbulence-chemistry interaction in circumstances resembling those found in flameless combustion. Two important characteristics of the flames produced by the DJHC-burner are the random ignition phenomena that stabilise the flame [68] and the role of entrainment of the non-homogeneous coflow

into the flame zone [77]. The main objective of the present study is to get insight into the processes that occur when the fuel jet is suddenly started, and their relation to the ignition delay.

4.2 Experimental setup

4.2.1 Burner and fuel injection mechanism

The DJHC burner consists of a partially premixed ring burner, enclosed in a stainless steel tube with an outer diameter of 89.2 mm, that generates a coflow of hot flue gases. This coflow surrounds a cooled fuel jet that emerges from a stainless steel tube of 4.5 mm inner diameter, as illustrated in the inset of Fig. 4.1. The burner was designed to mimic conditions found in flameless combustion. Due to the radiative and convective cooling of the outer burner tube, the flue gases carry a heat loss, reducing the adiabatic flame temperature. The design is based on that of the Adelaide jet-in-hot coflow burner [19]. More details on the geometry can be found in [77].

To generate reproducible transient jets, the burner was retrofitted with an electrically pulsed fuel injection system, connected to a digital timing system. The fuel used in the jet stream is a synthetic mixture of 80% methane, 5% ethane and 15% nitrogen, thus resembling Dutch natural gas. Special care was taken to design a system that generates a fast and highly reproducible injection of fuel. The system is outlined in Fig. 4.1. A solenoid valve was installed downstream of a buffer vessel with a volume of 4 litres, which serves to minimise pressure drop during the jet pulse. A gas bottle equipped with a pressure reducer supplies the fuel. The system was fine-tuned by adjusting a manual valve such that the pressure drop for a given flow rate (measured with a Bronkhorst low-ΔP mass flow meter) was equal. The measurements obtained during the transient are not considered, because the response of the flow meter is relatively slow. The fuel jet and the air stream of the secondary burner were individually seeded with Al_2O_3 particles (nominal diameter 1 μm), supplied by cyclone seeders.

4.2.2 Solenoid controller and counter

The solenoid valve was controlled by a digital system. A programmable processor (Atmel AVR Mega32) was clocked at a frequency of 10 kHz. Each injection cycle the solenoid counter receives a 24 V DC signal with a duration of approximately one second. The solenoid triggering ran independently of the timing of the PIV and PLIF systems. The cycle time was 3.211 seconds, such that it was not phase-locked with the combined PIV and OH-PLIF measurements that run at 10 Hz: after ten cycles, measurements are evenly spaced across the cycle-time domain. A 16 bit TTL signal was generated to provide the cycle-time to the measurement devices. This signal was either used directly (in the LDA measurements) or was used as input for a binary LED clock. This device was constructed

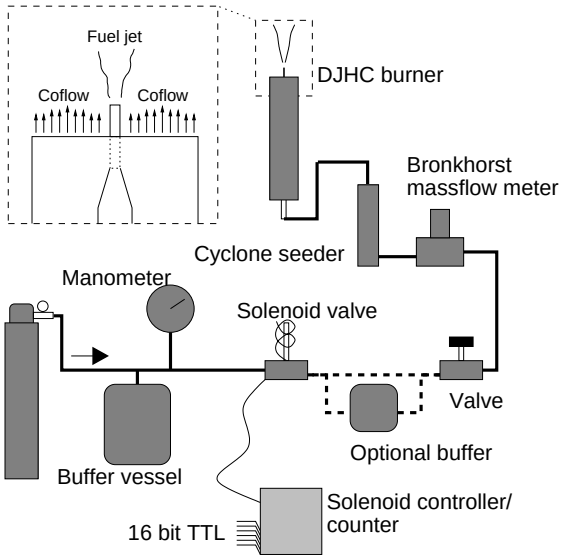

Figure 4.1: Fuel injection system. The fuel enters the system at the arrow at a fixed pressure (of either 0.4 bar or 1.0 bar). The 4 litre buffer vessel ensures that the pressure fluctuations due to the periodic opening of the solenoid valve are small. The solenoid valve is operated by a digital controller that also generates a 16-bit TTL timer signal to be used by the measurement devices. Before entering the DJHC-burner, the fuel flow is seeded by a cyclone seeder. Optionally, a small buffer can be used to decrease the rate of velocity increase of the jet (used for the "slow" case).

such that it could be run in continuous or triggered mode thus generating a well-defined time signal in case of longer exposure times of the PIV system.

4.2.3 Laser Doppler anemometry

A two-component LDA system (manufactured by TSI) was used to measure velocities. The setup is identical to that described in [77]. The external TTL signal of the solenoid controller was connected to the digital input of the TSI system, to obtain velocities measured in time relative to the solenoid pulse.

4.2.4 CARS temperature measurements

Temperatures were determined with Coherent anti-Stokes Raman Spectroscopy (CARS). The system has been described in detail in [69]. The inaccuracy of the system is estimated at 20 K, and the single-shot imprecision varies from 1% at 2000 K to 4% at 300 K. The weighted fitting procedure, described in [69],was applied to prevent any bias due to temperature gradients. Mean temperatures were determined from 1000 CARS spectra.

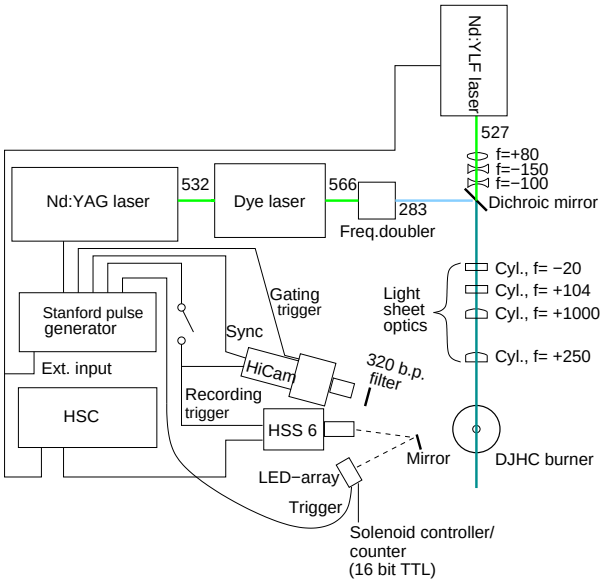

Figure 4.2: Schematic overview of the optical and electronic setup for the combined PIV and OH-PLIF measurements.

4.2.5 Particle image velocimetry

The measurement setup is outlined in Fig. 4.2. A high repetition rate Nd:YLF laser (Quantronix Darwin Duo 80-M) was used as a light source for the PIV measurements. The slightly diverging 527 nm beam generated by the laser passed through a positive and two negative lenses, a dichroic mirror (>90 % transparency at 527 nm) and through three cylindrical lenses, forming a light sheet of 60 mm height and 0.8 mm thickness. Light scattered by the Al_2O_3 particles was collected through a 200 mm Nikkor ED lens, and recorded by a Photron SA1 high-speed camera. The resulting resolution was around 13 pixels per mm. Both the laser and camera were controlled by a LaVision high-speed controller (HSC). LaVision's software package Davis (version 7.2) was used for the target calibration, data acquisition and the post-processing. Image pairs were captured at either 100 Hz (in conjunction with OH-PLIF measurements) or at 10 kHz. The time between the pulses was set to 20 μs. To determine the relatively low velocities of the coflow the 10 kHz measurements were used, matching the first frames of image pairs k and $k+2$, resulting in an effective time separation of 200 μs. Processing of the PIV images was done with multiple passes with decreasing interrogation area sizes. To resolve the jet, the interrogation area was 16×16 pixels, for the coflow it was 32×32 pixels. Vectors with peak correlation ratios smaller than 1.4 were rejected. A mirror was positioned at the edge of the field of view such that the binary LED clock could be observed. Cycle times were retrieved in a post-processing step.

4.2.6 Planar laser-induced OH fluorescence

A Spectra Physics PRO250-10 Nd:YAG laser produced 400 mJ pulses at a wavelength of 532 nm. This beam was used to pump a Syrah PrecisionScan dye laser operating with Rhodamine 590 in methanol. The $Q_1(6)$ line of the $A^2\Sigma^+$ - $X^2\Pi$ (1,0) transition of OH at 282.9 nm was excited, at an energy of 10 mJ/pulse and a repetition rate of 10 Hz. The output beam was transformed into a sheet with a height of 60 mm and a thickness of 0.6 mm, by the same optics as those of the PIV system. Overlapping of the LIF sheet with the PIV sheet was done with the dichroic mirror. The centre-to-centre misalignment of the two light sheets was measured to be less than 0.3 mm. The fluorescence signal was collected through a Semrock narrow pass filter (transmittance exceeding 70% between 300 nm and 320 nm) and a 105 mm Nikkor UV lens, and recorded by a Lambert Instruments HICAM CR camera, with a resulting resolution of 11 pixels per mm. The same configuration of lens and camera was also used for the high-speed flame luminescence measurements. Background correction was applied to both the OH-PLIF and the high-speed luminescence images. Additionally, spatial averaging with a disk with a radius of 9 pixels was applied to the high-speed luminescence recordings. Flame structures were recognised from the luminescence images by applying a threshold value of 9, out of a maximum of 255.

4.2.7 Simultaneous PIV and OH-PLIF measurements

The OH-PLIF measurements were done simultaneously with the PIV measurements. Temporal matching of the PIV and OH-PLIF images enabled timing of the OH-PLIF signal, as the PIV images contained the time data. The trigger pulse of the high-speed controller of the PIV system was used as external timing input for a Stanford DG535 pulse generator, which controlled the Nd:YAG laser and the timing of the intensified camera. The recording of both cameras was triggered with a single external TTL-signal to ensure identical timing. The view direction of the OH-PLIF camera is not perpendicular to the light sheet, but at an angle of 82°. To obtain correctly superimposed PIV and OH-PLIF images, accurate spatial calibrations of both systems are necessary. For the OH-PLIF system, a polynomial fit was calculated, using the pseudo-inverse based on nine reference points of the calibration target. As mentioned before, the calibration routine of the Davis software was used for the PIV images. Due to the high thermal load from the burner to the environment, the position of the optics changed slightly when the burner was operational, leading to deviations between the PIV and OH-PLIF images compared to the cold situation. Therefore, an additional hot-target calibration was performed. For this purpose a stainless steel target, fitting tightly in the fuel tube, was constructed. The target was marked at 10 mm height intervals. After insertion of the target, snapshots with the PIV and OH-PLIF cameras were made, providing the needed translation to match the approximate centre-coordinate, $(r, z) = (0, 80)$, of the images. The relative calibration inaccuracy for the superimposed PIV and OH-PLIF images is estimated (from the marks in the hot-calibration pictures) at approximately 0.2 mm in the region of interest (radially between -20 mm and 20 mm, axially between 60 mm and

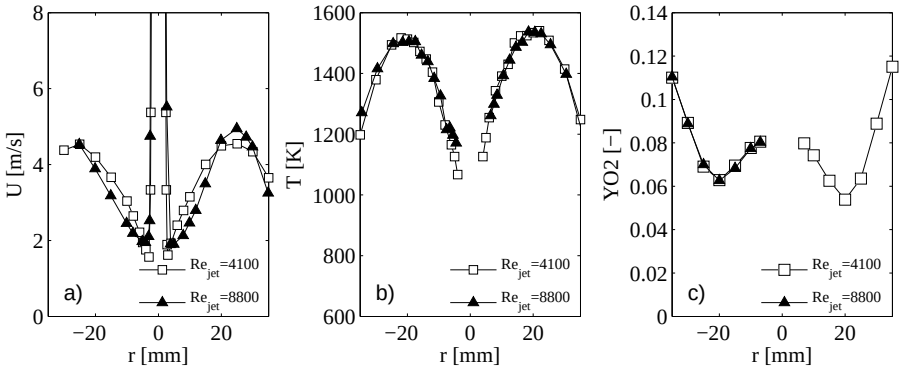

Figure 4.3: The boundary conditions at z=3 mm for two steady jet Reynolds numbers: the axial velocity determined with LDA (a), the mean temperature distribution as measured with CARS (b) and the mean oxygen mass fraction measured with a flue gas analyser (c).

100 mm).

4.2.8 Case description

The properties of the coflow are identical to those of the DJHC-I case, which has been described earlier in [77]. Its characteristics are summarised in Fig. 4.3. The peak coflow temperature of this case is 1540 K (with a standard deviation of 110 K at z=3 mm, r between 5 and 35 mm). The bulk velocity of the coflow is approximately 4 m/s.

The measured oxygen mass fraction (mass-flux averaged, between r=2.5 and r=35 mm) is 7.6%, with an inaccuracy of $\pm 0.2\%$. The oxygen volume fractions, measured with a flue gas analyser, were converted to mass fractions using the data from equilibrium chemistry calculations. The temperature field of the coflow without the central jet, which is the condition at the moment when fuel injection starts, is displayed in Fig. 4.4.

Because of the challenging nature of the experiments, only two cases were considered, between which the settings of the fuel injection system were varied. This resulted in different velocity histories at the fuel tube exit. The two cases are thus characterised by a fast and slower increase in velocity and a high and lower maximum velocity (with maximum Reynolds numbers of 8,800 and 4,100, respectively). These cases are termed “fast” and “slow” in the remainder of this paper. The difference between the cases was achieved by a variation in buffer vessel pressure (0.4 bar for the slow case and 1.0 bar for the fast case) and application of the additional buffer for the slower case, see Fig. 4.1.

The temperature of the fuel at the exit of the nozzle in its steady state has been determined to be around 430 K (slow case) and 360 K (fast case). Steady state fuel temperatures at the jet exit were obtained by comparing the mass flux of the fuel stream (known from the mass flow meters) with the volumetric flux obtained by spatially integrating the LDA data. This was done because of the insufficient quality of the CARS signal in the methane-rich,

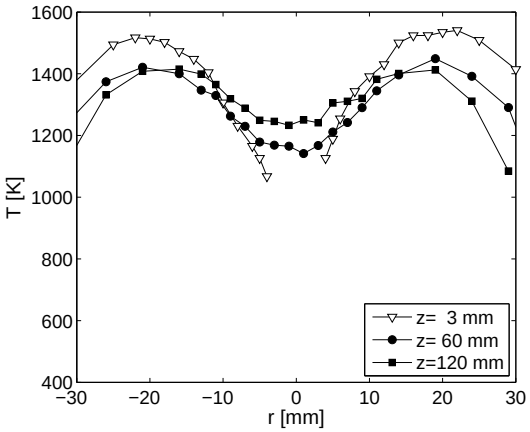

Figure 4.4: The mean temperature distribution imposed by the coflow (which forms the situation at t=0) at z=3 mm, 60 mm and 120 mm. The temperatures at z=60 mm and z=120 mm were measured with no jet present. The temperatures at z=3 mm were measured in the presence of the jet, the jet does however not strongly influence the coflow temperature at z=3 mm. In the latter traverse, the jet region is omitted from the figure.

cold environment just above the fuel tube exit. The relative accuracy of the temperature, based on inaccuracies of the mass flow meter, LDA statistics and the traversing system, is approximately 6%. The magnitude of the temperature fluctuations cannot be determined with this technique.

When modelling the transient problems described in this paper, the specification of appropriate boundary conditions is challenging. The availability of time-dependent boundary conditions or of boundary conditions at a location so far upstream that the boundary conditions are unaffected by the transient jet would be desirable. Measuring a full (species, temperature, velocity) and time-resolved data set of boundary conditions was not possible with the available techniques. The boundary conditions at z=3 mm are not completely unaffected by the jet velocity, as for instance the lateral velocity of the coflow increases by 0.3 m/s at r=15 mm at an axial height as low as z=3 mm. However, as the scalar properties do not change strongly at z=3 mm as a function of jet Reynolds number (as was shown in Fig. 4.3), application of the measured boundary conditions at z=3 mm as constant boundary conditions does not seem unreasonable. Alternatively, the boundary conditions might be specified somewhat more downstream (for instance at the burner tube exit at z=-12 mm) thereby allowing the lateral velocity to develop. Then, it should be checked that the conditions in the steady state at z=3 mm correspond to those measured.

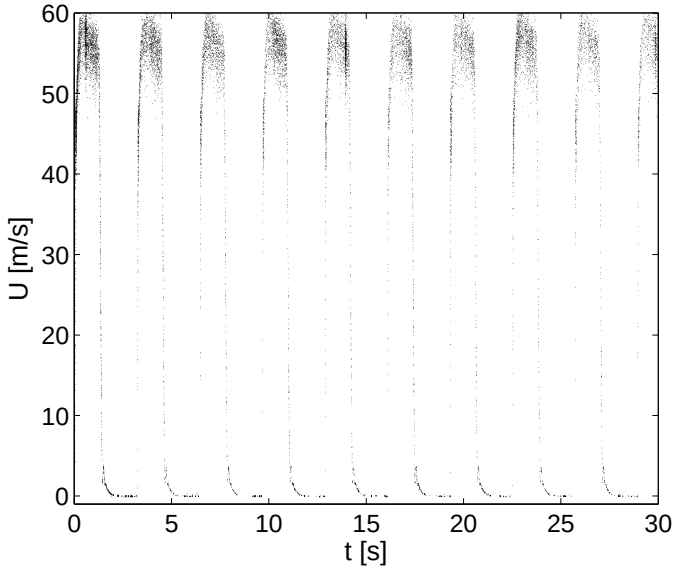

Figure 4.5: The axial velocity at r=0, z=3 mm during ten cycles, fast case.

4.3 The velocity field

4.3.1 Axial velocity at the jet exit

LDA was used to measure the axial velocity just above the exit of the fuel pipe (at r=0, z=3 mm). Fig. 4.5 shows the velocity for the fast case, over the course of ten cycles. In each cycle the jet velocity drops to zero during an interval of approximately 1.5 s. This amounts to approximately fifty times the coflow advection time (with a coflow velocity of 4 m/s and a height of 120 mm) which is sufficiently long for the velocity field to return to its stationary state without the jet.

Fig. 4.6 zooms in on the first 150 ms of the cycle, showing data from approximately 20 cycles. During the first 25 ms (fast case) or 41 ms (slow case), there is no response and the velocity remains zero. For both cases, this is followed by a sharp rise in velocity with very small scatter. The jet is still laminar during this phase. The reproducibility of the measurements is seen to be very good as the points lie on a thin line in this regime. The data from the time-resolved PIV measurements at 10 kHz are also shown in Fig. 4.6. These indicate good agreement between the two measurement techniques.

In the fast case, turbulence sets in suddenly, leading to a steep drop in velocity. The drop is not due to a sudden change in volume flux but due to a change in the shape of the velocity profile as illustrated in the inset of Fig. 4.6. In the case with slow start up, a more gradual transition is seen. Further evidence regarding this transition obtained from the planar PIV measurements is shown in Fig. 4.7. Given the dimensions of the pipe and the properties of the gas mixture at the inlet temperature, the bulk velocity at a critical Reynolds number of

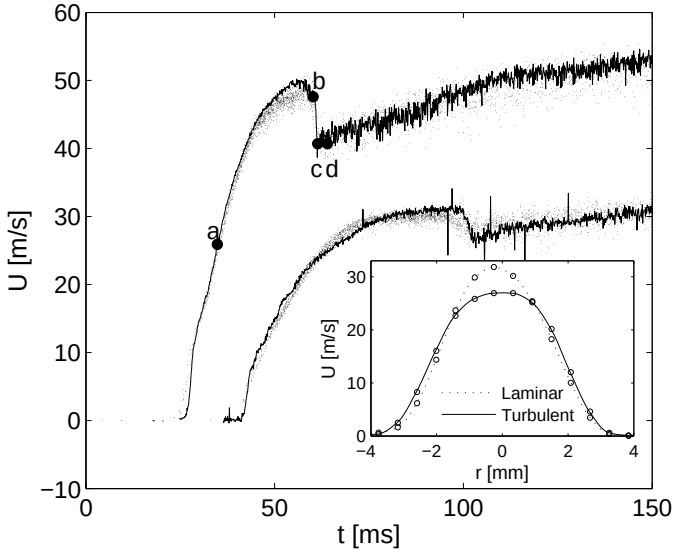

Figure 4.6: The axial velocity at z=3 mm from t=0 to 150 ms against cycle time, fast and slow case. The dots are velocities from LDA measurements, spanning twenty cycles. The grey lines are velocities from PIV measurements at 10 kHz. The inset shows average velocity profiles (averaged over 10 frames), 2 ms before ("Laminar") and 2 ms after ("Turbulent") the transition (slow case).

2,300 is approximately 7 m/s. However, as the fuel warms up in the tube as it travels up, its properties change. With fuel at a temperature of 430 K, the critical bulk velocity is roughly 14 m/s. For Poiseuille flow, this corresponds to a centreline velocity of 28 m/s. It is seen in Fig. 4.6, that the slow case undergoes the transition to turbulence close to that velocity, whereas the fast case has a strong overshoot. This overshoot is related to the stagnant phases in between the fuel injections. During these periods, the jet fuel is subjected to the higher temperatures inside the fuel tube. The heating up of this stagnant volume of fuel has a delaying effect on the laminar-turbulent transition, because of the further increase of kinematic viscosity with temperature. The temperature of the fuel tube in absence of fuel flow has been determined with thermocouple measurements to be approximately 500 K for the lower 0.6 m of its 0.7 m length, but it reaches 820 K in the upper 0.06 m, where the cooling air does not reach the fuel pipe. Considering the characteristic time for conduction of heat into the stagnant gas, r^2/α (with r the tube radius and α the thermal diffusivity of the fuel), of approximately 0.2 s, the fuel will have assumed a temperature close to that of the fuel tube in the stagnant phase. At a temperature of 500 K, the laminar centreline velocity at which the critical Reynolds number is achieved is 40 m/s.

Given the absence of the cooling effect of fuel flow in the stagnant phase, one might also expect the fuel tube to increase in temperature. The heat flux carried away from the fuel tube by the fuel during steady flow is however relatively small. Taking into account

its heat capacity, the fuel tube itself is estimated to warm up no more than 15 K in the time the fuel flow is absent. By time-integration of the velocity at the jet exit, it is seen that in both cases the total ejected volume until the moment of the transition approximates the stagnant volume. The transition is therefore expected to be not only caused by an increasing velocity, but also by a rapid change in kinematic viscosity, dropping by an estimated 45% (fast case) and 25% (slow case) to its steady value.

After the transition, the jet still accelerates slightly in both cases due to a gradual increase in pressure. This is caused by the volume present in the system downstream of the solenoid valve, mainly in the cyclone seeder. At t=300 ms, the jet exit velocity reaches its peak value, 33 m/s for the slow case and 58 m/s for the fast case.

4.3.2 Development of the jet

Rapid events in the flow field can be resolved in time when the PIV system is operated at 10 kHz. The succession of events that takes place after triggering the solenoid valve, and eventually leads to a developed turbulent jet, will be discussed in this section. The timing of these events has been indicated in Fig. 4.6, for the fast case. The characters a-d in this figure correspond to the subfigures in Fig. 4.7.

At the moment the velocity starts to increase at the jet exit, a "mushroom"-shaped vortical structure is formed just above the nozzle. These structures are commonly observed in starting jets [80, 81, 82, 83, 86, 87]. As the lobes of the "mushroom" encounter the relatively slow coflow, long thin structures with a high seeding density are created on either side of the jet. The velocity field near the tip of the starting jet is shown in Fig. 4.7a. The laminar jet propagates upward with minimal spreading. As the jet accelerates and the Reynolds number increases, flow instabilities start to occur. Initially, the jet is stable at the bottom, but unstable at a height of around 60 mm, fluctuating in position but remaining thin. This is depicted in Fig. 4.7b. At a certain moment, the flow in the pipe becomes turbulent, leading to the emergence of turbulent structures at the fuel jet exit (Fig. 4.7c). At the jet exit, the velocity profile suddenly switches from that of a laminar pipe flow to that typical for a turbulent pipe flow: the velocity decreases in the centre and increases somewhat near the edges. This results in a rapid drop in centreline velocity (see also Fig. 4.6, from b to c). At heights above 30 mm, this sudden transition is accompanied by an instantaneous decrease in the density of the jet seeding, evidence of the strong mixing in the turbulent regime. The slow case also exhibits this transition from laminar to turbulent, although the sequence of events takes place more gradually.

The times of transition to turbulence (defined to lie midway between the time of the fast decay of the velocity in the centre of the nozzle and the time when the velocity in the centre of the nozzle reaches its turbulent value, see points "b" and "c" in Fig. 4.6) are 61 ms for the fast case and 103 ms for the slow case. The reproducibility of this transition time is estimated at $\pm$ 0.5 ms for the fast case, and $\pm$ 1.0 ms for the slow case. Within a time span of a few milliseconds, the unstable jet evolves to a fully turbulent state as the turbulent

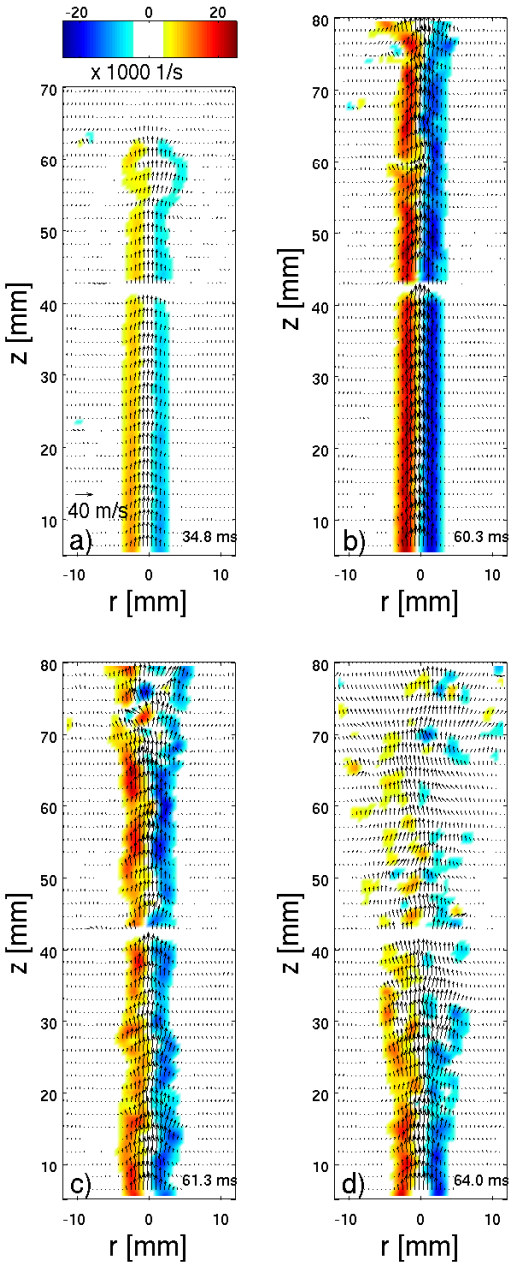

Figure 4.7: Instantaneous velocity fields for the fast case. The colour scale indicates the magnitude of vorticity. The vertical resolution of the vector grid has been decreased by a factor of three for visual purposes. The upper and lower parts of each of the four subfigures are taken from different runs at identical times after the solenoid valve trigger.

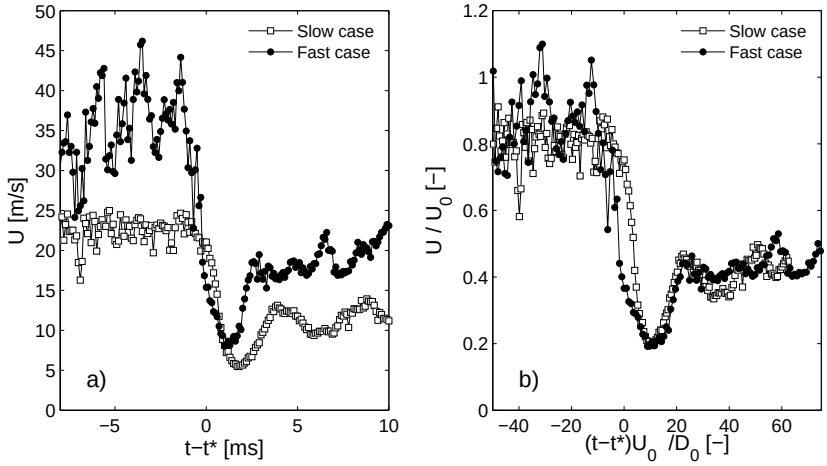

Figure 4.8: The drop in axial velocity on the centreline after the transition to a turbulent state, from the PIV measurements at 10 kHz at z/D=16 (obtained by averaging the vectors between z=66 and z=78 mm). The right plot shows the results with the time axis normalised with the jet time scale, and the velocity axis with the jet velocity. The velocity in the centre of the jet nozzle just after the transition is taken as characteristic jet velocity.

structures from the jet exit are convected downstream rapidly (Fig. 4.7d). The centreline velocity inside the considered domain indeed approaches its steady state turbulent value quickly, as shown in Fig. 4.8a. When the time and velocity axes are rescaled, it is seen that in both cases the centreline velocity reaches its steady state value (of $U/U_0 \approx 0.45$ at z/D=16, [77]) after about 25 integral jet time scales, Fig. 4.8b. This value cannot be directly compared to the correlations of jet penetration theory, as jet penetration is usually defined using jet fluid mass fractions and applies to axial distances exceeding 20 nozzle diameters [81]. Nonetheless, it is interesting to note that the time delay is of a similar order of magnitude as predicted by that theory (32 jet time scales at $x/D = 16$).

The initial laminar phase is rather specific for a laboratory setup, with lower Reynolds numbers than those found in industrial setups. The laminar jet however hardly interacts with the coflow, and the sudden transition toward a turbulent state occurs when the mass flux through the jet is close to its steady value. In this respect, a highly impulsive transient is generated. There is a noteworthy difference between the transient generated here and the transient studied in Fast et. al [85]. In the latter experiments the initially injected fluid was N_2, allowing the jet to develop first, after which the switch from N_2 to DME was made. By doing so, the transient response of the velocity field was decoupled from the injection of DME, allowing specific focus on the chemistry and mixing time scales. In the current study, the effect of the response of the flow field to the transient jet is however also included.

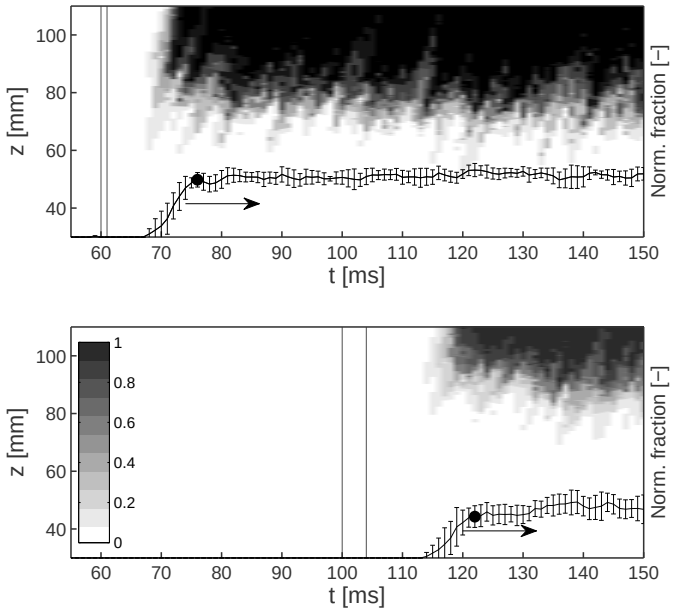

Figure 4.9: Ensemble-averaged ignition sequence for the fast (top) and slow (bottom) cases. The grayscale levels indicate the fraction of the realisations that have flame structures present, as a function of axial height z and time t. The lines corresponding to the right axes indicate the (arbitrarily scaled) vertically integrated value. The errorbars have a length equal to the variation of these values between the realisations (standard deviation of the ensemble). The two vertical lines indicate the times of the start of the rapid decay and the steady turbulent state of the velocity at the jet nozzle (Fig. 4.6, points b and c).

4.4 Ignition sequence

Now that the sequence of events in the flow field during a cycle has been mapped, ignition events can be related to the flow field. To study ignition events the flame luminescence was monitored with the intensified high-speed camera at 1 kHz such that a useful statistical ensemble, resolving the ignition stage, could be obtained. Ten ignition sequences were recorded for both cases. The data processing (background subtraction, spatial filtering and boundary detection) was done as described in [68]. The flame luminescence was sampled each millisecond, as was the LED light indicating that the solenoid was triggered, resulting in an absolute timing uncertainty of one millisecond. With a sample size of ten, this amounts to a 95% confidence interval for the mean ignition delay due to the limited resolution of the timing of $\pm$ 0.3 ms. Thus, the reproducibility of the transition itself is normative.

Results are presented in Fig. 4.9. The graytone indicates the presence of flame pockets as a function of height z and cycle time t. For instance, a graytone of value 0.5 indicates that in five out of ten realisations, a flame structure was recognised at that time at that axial

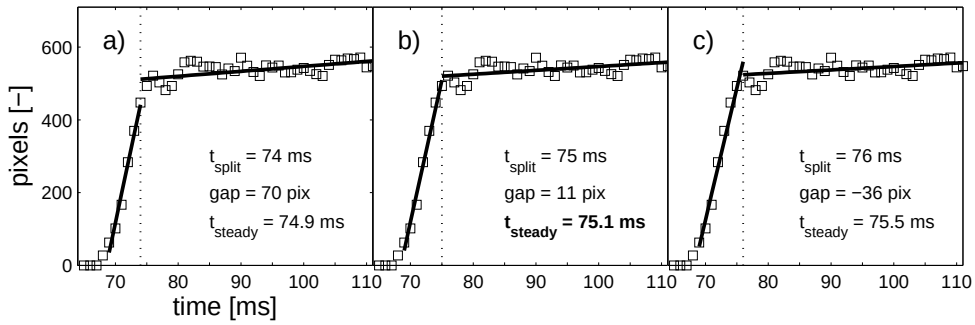

Figure 4.10: The procedure by which the time at which a steady burning state is reached is determined, shown for the fast case. In Figs. a to c, the trial split between the rising edge and the steady-state is made at t=74 ms, 75 ms and 76 ms, respectively. The gap between the two linear fits left and right of the split is smallest in Fig. 4.10b. The division at t=75 ms is therefore chosen, and the time when a steady state is reached is determined from the crossing point between the two fits, at t_{steady} =75.1 ms.

height.

After the jet has become turbulent, the flame structures as they are observed in the steady-state flame, typically at a height of z=70 mm and up, are not present immediately. That the ignition and stabilisation process is delayed is not surprising. Not only will there be some chemical delay, the important process of entrainment of coflow fluid needs a turbulent and developed jet. Nevertheless, in terms of jet time scales, the delay is very long: even though after 25 jet time scales (3 and 4 ms for the slow and fast case, respectively) the jet is turbulent and the centreline velocity has reached its steady value, there is not yet any sign of reactions.

In the fast case, ignition kernels start to appear at t=70 ms (9 ms after the transition to turbulence at the jet nozzle) and in the slow case at t=117 ms (14 ms after the transition to turbulence). The standard deviation of the time of their first appearance is approximately 2 ms, larger than the reproduciblity of the transition times and the sampling interval of the luminescence but the sample size is too small to deduce an accurate value of the true rms of the ignition events. The ensemble averaged value of the presence of flame pockets approaches its steady state in both cases somewhat later, making the total delay 15 ms for the fast case and 19 ms for the slow case. The moment that a steady-state situation is reached is indicated by the black dots in the error bar plots in Fig. 4.9.

This steady state time is determined by fitting a two-piece linear spline, and determining the crossing point, as illustrated in Fig. 4.10. The left point of the first part coincides with t_{ign}, the right point of the second part is $t_{\mathrm{ign}} + 40$ ms. The optimal split time can be determined based on minimisation of the vertical gap between the left and the right fit, or on a least squares criterion. For the current data, this yields identical results. When applied to computer generated random data with similar rms values and sample size, a

trend break (which is where the expectational value has a discontinuous derivative) could be detected with an accuracy of 0.1 ms, and a 95% confidence interval of ± 1.1 ms. It is important to note that the gradual transition from first ignition to the steady state situation over several milliseconds is a property of the individual ignition events, and is not due to statistical scatter of individually instantaneous transitions. The timing of the flow- and ignition events is summarised in Table 4.1.

Case	t_{trans} [ms]	t_{ign} [ms]	t_{steady} [ms]
Fast	61.0 [$\pm$0.5]	69.9 [$\pm$1.0]	75.1 [$\pm$1.1]
Slow	103.0 [$\pm$1.0]	117.0 [$\pm$1.6]	121.6 [$\pm$1.1]

Table 4.1: Summary of flow- and ignition events, expressed in times relative to the solenoid valve trigger. The values between brackets for t_{ign} indicate the 95% confidence interval for the mean (estimated with the t-distribution). The values between brackets for t_{steady} indicate the 95% confidence interval for the technique of applying linear splines as outlined in Fig. 4.10, determined by applying it to similar computer generated data

.

In the slow case, the first signs of flame structures appear before the transition from laminar flow to turbulent flow. Straight contours of faint luminescence (not recognised by the image processing routine) are seen now and then at $t \approx 90$ ms, at a height of around z=100 mm and up. This kind of flame is also seen when a steady laminar fuel flow is injected. The flame structures are long, and have a relatively stationary but very faint boundary at their trailing edge, unlike the "flame pockets" encountered when the fuel flow is turbulent. With the simultaneous PIV and OH-PLIF measurements, these flame structures are observed more clearly. Fig. 4.11a shows such a faint flame, enclosed in the dashed box, 10 ms before the transition towards turbulence, around a jet that is still laminar at the bottom but somewhat unstable higher up.

The flame structure seems to be the product of a steady autoignition process: a steady stream of fuel/coflow mixture is formed in the low-velocity coflow, ready to ignite at some downstream location that changes only slowly in time. Its maximum radial thickness, judged from the OH-PLIF image, is 3.5 mm. To study the velocity field in the neighbourhood of the flame, the PIV data was first convoluted with a 2-D Gaussian kernel with a width of 1.5 times the vector separation (σ=0.9 mm, thus much smaller than the flame thickness) to reduce noise, after which the spatial derivatives were calculated. In the region where the flame is seen in Fig. 4.11a the velocity field is virtually free from vorticity (the spatially averaged vorticity is 80 s^{-1}), in agreement with the undisturbed appearance of these flame structures. The absolute value of the principle strains is lower than 120 s^{-1}. At the same radial and axial distance at the right side, where no flame is seen, similar values are found. Compared to strain rate values at extinction events measured in flames with non-preheated reactants (1500 s^{-1} [49] or even an order of magnitude higher [88]) this is very low, whereas the preheating typically increases the extinction strain rate, or makes

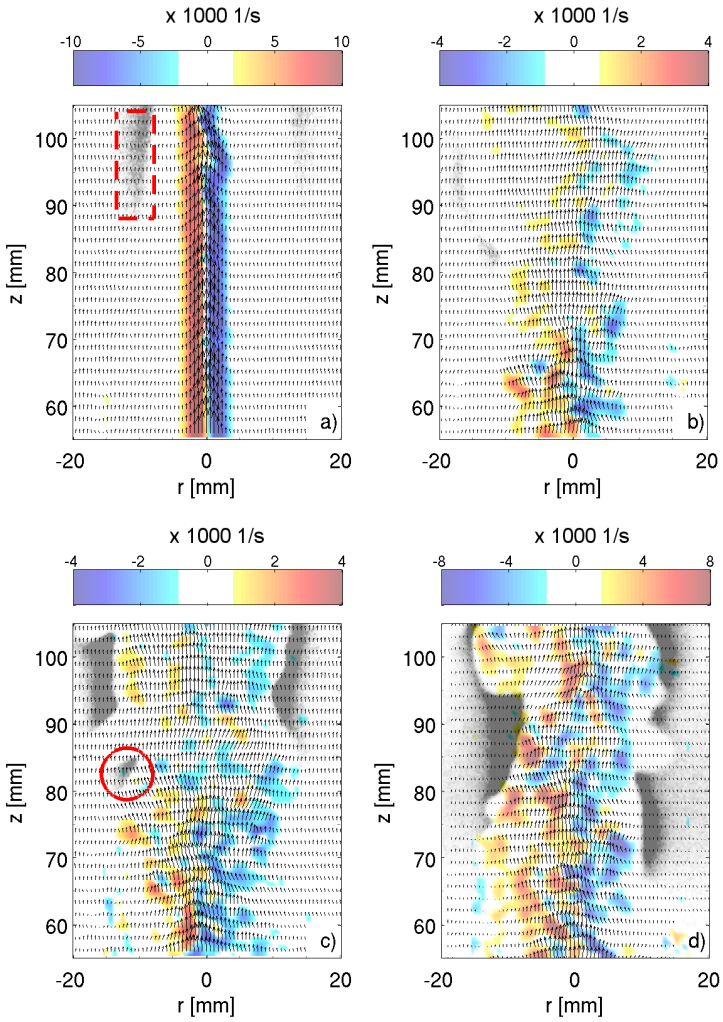

Figure 4.11: Four simultaneous PIV/OH-LIF snapshots, a) to c) from the slow case, d) the fast case. Vorticity contours transparently plotted on OH-PLIF images, the colorbars corresponding to the vorticity contours are displayed on top. Velocity vectors are again vertically reduced by a factor of 3. a): Faint flame contour in the slow case t=93.4 ms. b): Turbulent jet, 12 ms after transition, slow case t=115.4 ms. c): Slow case, steady state. Note the small encircled flame pocket at (r, z)=(-12,84). d): Fast case, steady state.

the conventional sharp extinction limit disappear altogether [89]. Given this result, their appearance and disappearance is likely not related to the action of strains imposed by the turbulent field (low strains enabling their ignition or high strains promoting their extinction), but to temporal variations in coflow temperature or in the large-scale convection and diffusion processes that bring the jet fuel and hot coflow together, influencing the sensitive process of auto-ignition.

Fig. 4.11b shows the situation some twenty milliseconds later, twelve milliseconds after the transition to turbulence. No clear sign of any reaction is seen, consistent with the flame luminescence observations. A snapshot of the steady state situation of the slow case is depicted in Fig. 4.11c. A small flame pocket is encircled, at (r, z)=(-12 mm,84 mm), likely ignited shortly before. The steady state of the fast case, shown in Fig. 4.11d, shows reactions taking place at lower heights. Note the disconnected reaction zone on the right. In the turbulent cases, the flames also reside in portions of the flow with low vorticity and low axial velocities, typically around 5 m/s. This is in agreement with the convective velocities of the flame pockets determined earlier, obtained by analysing high-speed flame luminescence recordings [68].

Two different time intervals related to the ignition process were examined, namely an ignition delay t_{ign} and a time interval until a steady state is reached t_{steady}. There are at least two reasonable hypotheses on the origin of these delays.

One possibility is that the delay is mainly due to chemical time scales. In that case, the properties of the scalar field are identical to those in the developed turbulent situation. Reactive mixtures are then immediately present, and the time between transition and ignition is the ignition delay of the most reactive mixture. This was the nature of the delay as observed in the experiments reported in [85], where ignition delays were not significantly influenced by jet velocities. Additionally, the turbulent mixing time could be involved, determining how fast homogeneous mixtures of favourable scalar properties are formed. A comprehensive review on this subject can be found in [45].

The second possibility is that the timescales are related to the development of the entrainment process. This seems plausible, given the important role of entrainment on the flame stabilisation due to the radial temperature gradient in the coflow [77]. In this case the scalar field is *not* that of the steady-state turbulent situation, but it has to develop first. The dynamics of this large scale entrainment process are elaborated on in the next section.

4.5 Transition to turbulent entrainment

The common meaning of "entrainment" when applied to turbulent jets is the process in which irrotational fluid surrounding the jet becomes turbulent. In fluids with Schmidt numbers close to unity, the material interface lies close to the fluctuating vorticity interface [90]. This implies that, as soon as coflow material becomes part of the turbulent jet, it mixes rapidly with the jet fluid. The temperature gradient of the coflow adds an extra dimension to the problem. For the hotter part of the coflow from larger radii to be entrained

by the jet, it has to be transported radially inwards first. The rate of entrainment strongly influences the axial height where reactions begin to occur, in an opposite manner as observed in normal lifted flames: higher jet velocities result in lower heights of first reactions and lower lift-off height [77]. The evolution of the entrainment of hot coflow toward the mixing layer is therefore of critical importance.

Although the temperature field has not been measured in a time resolved manner, the transport of temperature can be investigated using the PIV data. Because the turbulent fluctuations of temperature and velocity in the coflow are small compared to their mean values, the heat of the coflow is transported approximately passively [77]. A fluid parcel found somewhere in the coflow therefore still carries information on the temperature from its "injection" (or labeling) point (where it is assumed to be given as a boundary condition), which can be traced back through its pathline.

Because of the nature of the problem, a Lagrangian viewpoint is most natural. Using the notation of Bennett [91], the position of a Lagrangian particle at time t, labeled with its position $\mathbf{x_0}$ at time s is denoted with $\mathbf{x}(\mathbf{x_0}, s \mid t)$. The streakline $\mathcal{S}(\mathbf{x_0}, t)$ is now defined as the set of locations reached by Lagrangian particles that were labeled at point $\mathbf{x_0}$ in some finite time interval: $t_0 \leq s \leq t$. In a stationary situation, a streakline $\mathcal{S}(\mathbf{x_0})$ is aligned with the streamline through $\mathbf{x_0}$. In an unsteady situation, this will not be the case. Unlike streamlines, fluid particles need to get convected by the velocity field itself.

If the flow field switches instantaneously from one stationary state to another, the evolution of the streaklines can be expressed explicitly. To this end, define the streakline at $t < t^*$, where t^* is the moment of transition to turbulence, as $\mathcal{S}_L$ (omitting the dependence on time and labeling point for brevity). The streakline at $t > t^*$ is the locus of points belonging to two different sets, one originating from $\mathcal{S}_L$ and one originating from $\mathbf{x_0}$, after the transition:

$$\mathcal{S}(\mathbf{x_0}, t) = \{ \mathbf{x}(\mathcal{S}_L, t^* \mid t) \cup \mathbf{x}(\mathbf{x_0}, t^* \leq r \leq t \mid t) \}, \tag{4.1}$$

with $s < t^* < t$.

Therefore, even when the transition of the velocity field is instantaneous, it will take a certain time for the streaklines to reach their steady state. This time is needed to transport the fluid particles pertaining to the old situation $\mathcal{S}_L$ out of the considered domain, and is therefore equal to the ratio of the domain size and the convective velocity in the corresponding direction.

The evolution of the streaklines in the coflow for the fast case is demonstrated in Fig. 4.12, by the red dots. These dots represent virtual fluid particles, that were injected each frame (0.1 ms separation), starting from t_0=-9 ms, relative to the transition time, with a simple forward integration scheme of the interpolated PIV fields. The streak- and streamlines are clearly aligned initially, detach at the time of the laminar-turbulence transition and realign again, as qualitatively described by Eq. 4.1. The in-plane velocity component cannot be measured with the 2-D PIV-system. Due to axisymmetry of the flow the tangential velocity component is however not important to the argumentation. Furthermore,

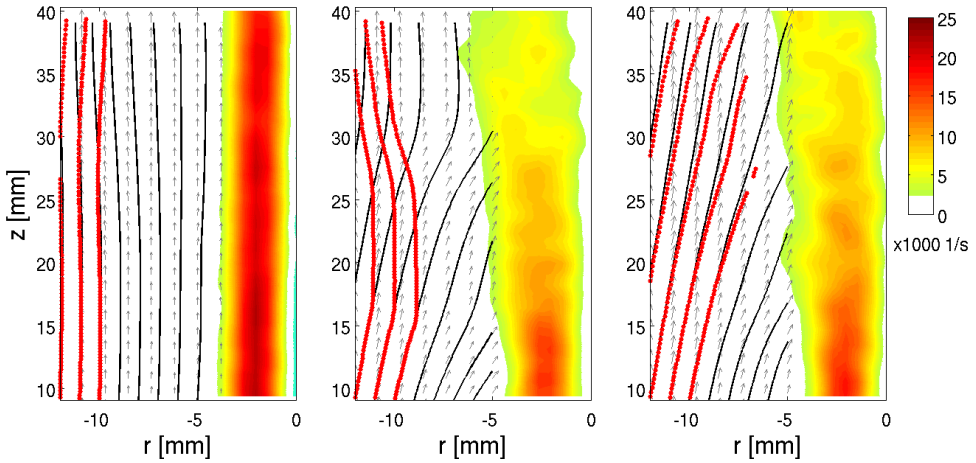

Figure 4.12: Streamlines (black lines) and Lagrangian particles (red dots), injected in the coflow starting 9 ms before the transition to turbulence, fast case. Left: 1 ms before transition to turbulence (jet still laminar), middle: 3.2 ms after the transition, right: 13.0 ms after the transition. The color levels indicate the vorticity magnitude, averaged over 21 frames (from -1 to +1 ms, relative to the snapshots).

the change in mean radial velocity is more than four times larger than the rms of the radial velocity such that the evolution can be examined from a single realisation.

The response times of both the streaklines and streamlines of the coflow within the field of view of the PIV recordings, which lies roughly between z=5 and z=40 mm, can be quantified using this data. To this end, the radial location of streak- and streamlines that emerge from $\mathbf{x_0} = (-14\mathrm{mm}, 9\mathrm{mm})$ were monitored at an axial height z=38 mm. The resulting values are displayed in Fig. 4.13. An approximate time until steady-state of the streaklines is in both cases 8 ms. Extrapolating this value to the location where the reaction process were first observed by OH-PLIF and high-speed imaging (roughly z=60 mm for the fast case and z=70 mm for the slow case), approximate delays to the steady state of 12 ms and 14 ms (fast and slow case, respectively) are expected. Keeping in mind that mixing and ignition processes take additional time, these values are in line with the observed values of 14 ms and 19 ms.

The time needed for the streaklines to realign with the vector field is thus of great influence for the delay, but the response time of the vector field itself can not be neglected either. The response of the velocity field surrounding the jet is much faster than that reported in the experiments of Cossali et al. [83]. Interestingly, the time scales for the response of the vector field and the scalar field in the coflow have different origins. As discussed in Section 1, the adaptation of the vector field is governed by jet time scales. From Fig. 4.12 it is however evident that the coflow velocity determines how fast the scalar field reaches its steady state. For transient flames, igniting in inhomogeneous surroundings, these two

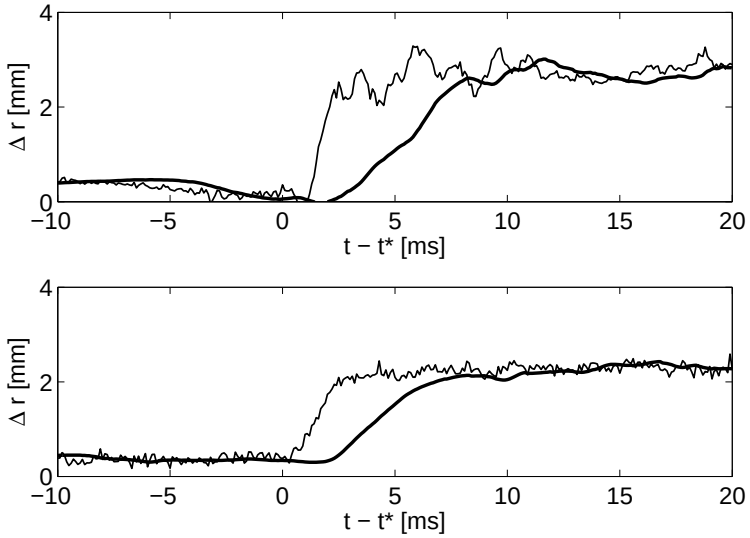

Figure 4.13: Radial displacements at z=38 mm of streamlines (thin lines) and streaklines (thick lines) starting at $\mathbf{x_0} = (-14\mathrm{mm}, 9\mathrm{mm})$, fast case (upper) and slow case (lower graph). Time is relative to the start of transition to turbulence.

time scales are therefore of relevance. When this insight is applied to furnaces, this means that when large scale inhomogeneities are present, instationary behaviour might be of a duration multiple times longer than that expected on the basis of jet time scales.

4.6 Conclusions

Time resolved flow- and ignition processes in the near field ($z/D < 22$) of transient jets of natural gas in a hot coflow were studied, using LDA, PIV, combined PIV/OH-PLIF and flame luminescence. The electronic control system yielded reproducible velocities, such that results from the different measurement techniques could be combined to form a coherent picture of the observed events. Two cases were considered, differing in jet acceleration and velocity, hence their labels “slow” and “fast”.

A specific fluid dynamic behaviour, characterised by an initial laminar phase followed by a sudden transition toward a turbulent phase, was observed in both cases. No significant amount of combustion took place during the initial laminar phase. After the transition to turbulence, the velocity field adapted itself relatively fast in both cases (in 3 ms and 4 ms, or around 25 jet time scales), but significant additional delays until ignition and steady state combustion were observed. The average delay times to ignition were 9 ms and 14 ms for the fast and the slow case, respectively. A steady combustion was in both cases achieved 5 ms later. Flame structures were seen to reside in regions where the velocity is close to that of the coflow, in correspondence with earlier findings on the convective velocity of the

flame pockets.

The ignition delays were shown to be not merely a function of autoignition chemistry, or the response of the velocity field. Whereas the velocities in the surrounding fluid adapt themselves in time scales governed by the jet diameter and jet velocity, the actual transport of the surrounding coflow fluid to the region where reactions take place occurs on a timescale that is equal to the ratio of the axial distance of this region to the nozzle and the coflow velocity. The observed contribution of these (relatively large) time scales to the ignition delay therefore complements earlier findings on ignition delays and fluid dynamic response of transient jets. An additional variation in coflow temperatures, which could in principle shed more light on the influence of chemistry, was not undertaken. As a change in coflow temperature leads to a change in lift-off height, the role of chemistry is however always coupled with that of the studied transport processes.

Although the present research was conducted on a specific, laboratory-scale setup with relatively small Reynolds numbers, the observed phenomenon seems to be of general nature, and is therefore expected to apply to large-scale setups as well. With respect to regenerative furnaces, one can therefore conclude that transient processes may be significant during a relative large fraction of the cycle time, depending on the presence of large-scale inhomogeneities.

CHAPTER 5

Conditional flow field statistics

In this chapter the velocity field in a relatively small planar region, conditional on flame presence, is detailed. This information was obtained by the simultaneous application of two laser-optical techniques: planar laser-induced fluorescence of the OH radical (OH-PLIF) and Particle Image Velocimetry (PIV). An important result is that the conditional velocity field (conditional on the presence of OH) is very different from the non-conditional velocity field at the same location. The flame zones experience virtually no vorticity, but they are weakly strained by the jet. The average conditional strain perpendicular to the flame surface is neither compressive nor extensive due to the orientation of the principle strains and that of the flame interface. One millimetre inward to the jet, from the edge of the fuel-rich side of the OH contours, the average strains do become compressive, and the pdf of normal strain becomes considerably wider.

5.1 Introduction

Flames created by the injection of a gaseous fuel in hot, low-oxygen surroundings have received considerable attention in the past decade. This is due to the relevance of these flames to novel, clean combustion techniques in which a strong recirculation of flue gases and heat regeneration are employed. A frequently addressed issue is the role of autoignition and/or flame propagation in the flame stabilisation. For instance, Gordon et al. [32] used the convection, diffusion and reaction terms of species budgets to distinguish numerically between autoignition and flame propagation and applied this criterion to three flames of the Cabra burner [37] with increasing coflow temperature, to find that all three were likely stabilised mainly by autoignition processes. The sequence of CH_2O radical build-up, OH kernel formation and steady flame formation identified in later experiments [28] supports this view. Markides et al. [21] observed several different regimes in their Confined Turbulent Hot Coflow setup, one of which is the so-called "Random Spots" regime. Autoignition processes occur in isolated locations, and initiate flame propagation. Autoignition delay times were shown to increase with jet velocity, indicating that turbulence affects the autoignition delay times, in agreement with DNS calculations [53]. A comparable process of ignition kernel formation was identified in the DJHC burner [68], which is also the object of study in this paper. Using high speed flame luminescence recordings, ignition kernels

Submitted to *Combust. Flame*

were seen to form regularly below the mean flame base. This random process combined with the subsequent flame growth was identified as a stabilisation mechanism. Yoo et al. [44] performed DNS of a hydrogen flame in a heated coflow, and reported a more complex stabilisation mechanism, with autoignition processes occurring at the flame base in a cyclic motion, imposed by large coherent structures. Similar to [32], a diffusive flux of insufficient magnitude to balance the reaction source term was considered to be a marker for autoignition.

The experimental studies intended to probe the nature of the flame stabilisation have often elaborated the chemical aspects, by providing datasets of concentrations of chemical species [37, 19] or by planar imaging of selected species relevant to autoignition [28, 26]. The flow field has perhaps been somewhat underexposed, and where available, velocity information has been limited to one-point, non-conditional statistics [27, 77]. In the following, detailed conditional velocity statistics will be discussed, that were obtained by the simultaneous application of Particle Image Velocimetry (PIV) and Planar Laser Induced Fluorescence measurements of the OH radical (OH-PLIF). This is an established combination of techniques applied to both premixed [92] and unpremixed [93] flames, and it has recently been extended to high repetition-rate measurements [94, 49]. Nevertheless, to the author's knowledge, it has not yet been applied to hot-coflow flames.

The aim of this article is to provide new insights into the local flame structure of laboratory jet-in-hot-coflow flames. This insight can help in judging the applicability of the different combustion models that are available, and in understanding the nature of the turbulence-chemistry interaction in these flames. Additionally, the suitability of these setups to the study of industrial sized burners will be discussed.

5.2 Experimental setup

5.2.1 DJHC burner

In this paper, flames are studied that were generated with the Delft jet-in-hot-coflow (DJHC) burner. The main element of this setup is a secondary burner, enclosed by a steel outer tube, that generates a hot, oxygen deficient coflow stream into which a fuel jet is injected centrally. Fig. 5.1 shows the geometry of the setup, along with the window where measurements were taken (except for the measurements reported in Section 5.4.2, where the observation window is moved up by 10 mm), corresponding to the region in space where reactions start to emerge. A (z, r)-coordinate system is used with its origin at the centre of the fuel pipe exit, the z-direction pointing upward. This is referred to as the "global" coordinate system.

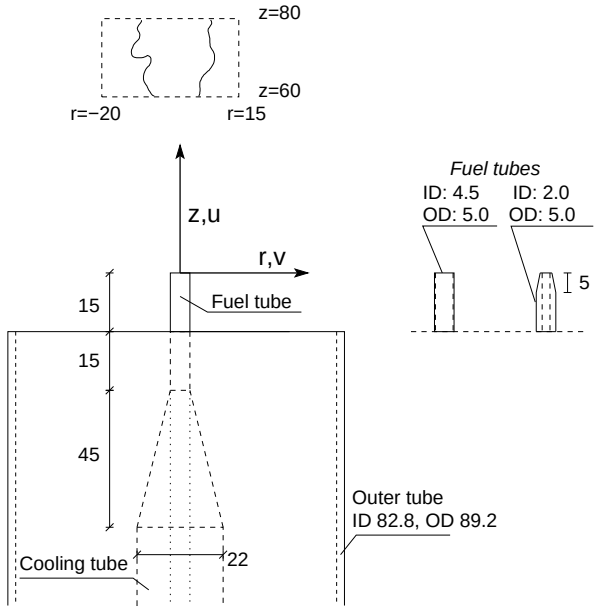

Figure 5.1: The geometry of the upper part of the DJHC burner. Dimensions are given in mm. The field of view is indicated with the dashed box. The geometries of the two fuel tubes that were used are shown at the right.

5.2.2 Case description

The coflow properties (temperature, velocity and oxygen mass fraction) were kept constant in the cases studied. The characteristics of the coflow correspond to the DJHC-I case which is addressed in more detail in [77]. These are summarised in Fig. 5.2.

The results are divided into a section in which LDA and PIV measurements are compared (Section 5.3), a section in which *conditional* velocity statistics are studied (Section 5.4), and a section devoted to the *conditioned* velocity field (Section 5.5). "Conditional" data are presented as a function of the global coordinates. The conditioned statistics are presented in a local coordinate system (introduced in Section 5.5) to study the flow field in the neighbourhood of the flame zones.

Flow field study

The results of Section 5.3 are based on a single fuel jet setting. A mass flux of 16.1 nl/min is supplied through the standard 4.5 mm diameter nozzle, resulting in a mean centreline velocity at the nozzle exit of 34 m/s, and a jet Reynolds number of 4,100. It thus corresponds to the DJHC-I, $\mathrm{Re_{jet}}$=4,100 case described in [77]. The reason for using a lower Reynolds number case for comparison with earlier obtained LDA measurement data is that the centreline velocity could be well resolved with PIV. The case $\mathrm{Re_{jet}}$=8,800 case, described in the next section, had too many spurious vectors close to the centreline for validation of the

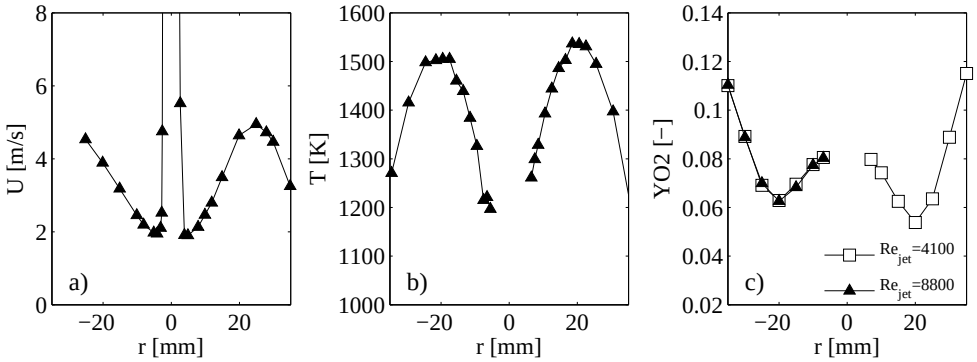

Figure 5.2: The coflow characteristics at z=3 mm, of the DJHC-I case with $\mathrm{Re_{jet}}$=8800 and the standard 4.5 mm fuel pipe. Shown are the mean axial velocity as determined with Laser Doppler Anemometry (LDA) (a), the mean temperature, as determined with Coherent anti-Stokes Raman spectroscopy (CARS) (b) and the mean oxygen mass fraction, determined with a flue gas analyser (c). In figure 5.2c, the results for $\mathrm{Re_{jet}}$=4100 were also included.

Case name	Fuel	Nozzle diam. [mm]	Vol. flow [nl/min]	$\mathrm{Re_{jet}}$ [-]	ξ_{st} [-]	$U_{\mathrm{jet;70}}$ [m/s]	$r_{\mathrm{jet;70}}$ [mm]
DNG 4.5	DNG	4.5	30	8800	0.019	28.2	11.1
premix 4.5	air+DNG (3:1)	4.5	32	9000	0.168	35.6	10.2
DNG 2.0	DNG	2.0	11	5900	0.019	27.9	11.1

Table 5.1: Overview of the test cases for the conditional and conditioned velocity statistics. The fuel ratio given in the second column is volumetric. The stoichiometric mixture fraction ξ_{st} is based on the injected fuel and the coflow properties at (z, r)=(3,20) mm. The maximum equilibrium flame temperature of the premixed fuel is 2023 K, instead of the 1950 K for the DNG flame.

jet region.

Conditional and conditioned velocity study

For the conditional and conditioned velocity statistics, three different fuel jets were considered, with a variation in fuel composition (achieved by premixing of the fuel with air) and in nozzle diameter (2.0 mm inner diameter instead of 4.5 mm).

The different test cases for the conditional velocity statistics are given in Table 5.1. Case DNG 4.5 corresponds to the DJHC-I, $\mathrm{Re_{jet}}$=8,800 case, as studied earlier [77]. The reported jet Reynolds numbers for the premix 4.5 and the DNG 2.0 cases where determined with the temperature of the fuel jet estimated at 360 K and 470 K, based on earlier determined temperatures with similar jet mass flow rates. The premixing of the fuel (case

premix 4.5) was done to study the effect of the stoichiometric mixture fraction, which is roughly 8 times higher than that of Dutch natural gas (DNG), with the coflow composition at (r, z)=(20,3) mm taken as characteristic for the oxidiser stream. The molar composition of DNG is 81.3% methane, 14.4% nitrogen, and some 4% of higher alkanes. The molar composition of the premixed fuel, 3 volumetric parts air on 1 volumetric part DNG, is 20.4% methane, 63.0% nitrogen, 15.8% oxygen and 0.9% of higher alkanes. The last two columns describe the centreline velocity and the radius of the jet of the jet at z=70 mm. The method to determine the jet radius is described in Section 5.5.2.

To investigate how premixing affects the ignition process, calculations were done with the SENKIN program [95] (as a constant pressure reactor) using the GRI-MECH 3.0 mechanism [96]. The properties for each mixture fraction were obtained by linearly interpolating the compositions between calculated mixture fractions (with the equilibrium chemistry program FLAME, with reactions turned off). The ignition delay time was defined as that time, where the temperature increase exceeded 50 K. Results from this study are shown in Fig. 5.3. It is seen that the premixing enlarges the mixture fraction with the shortest delay time by roughly five times when the ratio air/DNG is 3:1. The delay time itself is, however, hardly affected. Additionally, the autoignition delay time was calculated with a temperature increase criterion of 20 K, as shown by the grey curve.

The calculated values displayed in Fig. 5.3 should be interpreted with care. The steep rise of the curves towards lower values of the mixture fraction is because the difference between the equilibrium and mixing temperature approaches the chosen threshold. This introduces arbitrariness in the ignition times and in the estimate for the most reactive mixture fraction [74]. This issue can not be resolved by choosing the maximum heat release rate as criterion. The delay time until maximum heat release becomes progressively shorter with decreasing mixture fraction until a mixture fraction as low as 0.001, and it is doubtful whether the tiny accompanying temperature increase is relevant. It is concluded from Fig. 5.3 that the ignition delay time is in the order of a millisecond for both pure and premixed DNG. A one-dimensional calculation, including diffusion, would have to be considered for more accurate values and to obtain an estimate for the most reactive mixture fraction.

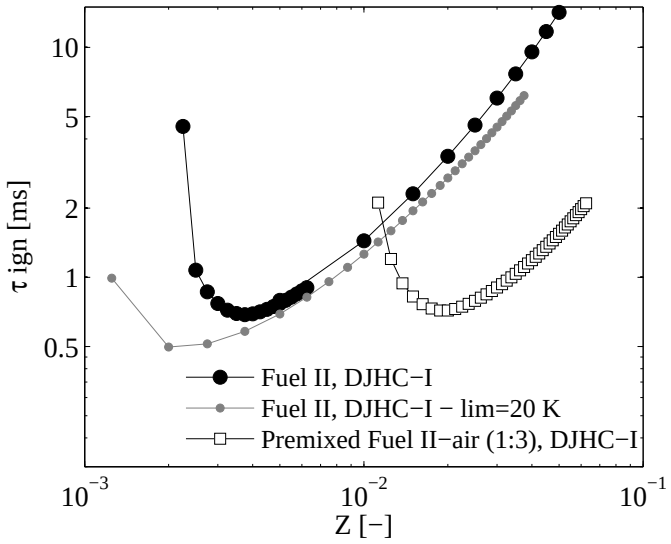

Figure 5.3: Autoignition times for a mixture approximating pure DNG and DNG premixed with air, 1:1 and 1:3 (ratios are volumetric), for a range of mixture fractions. The oxidiser stream properties are T_{co}=1500 K and $Y_{O2;co}$=6.3%.

5.2.3 PIV system and data processing

The coflow and the jet stream were both seeded with Al_2O_3 particles, with a nominal diameter of 1 μm. The particles were illuminated by a laser light sheet that was produced by a Nd:YLF laser (Quantronix Darwin Duo 80-M). The optical setup that combines the PIV and OH-PLIF systems is outlined in Fig. 5.4. The PIV laser sheet was approximately 40 mm high and 0.8 mm thick. Images were generally taken at 100 Hz, which is the lowest operational repetition rate of the Nd:YLF laser. A 200 mm Nikkor ED lens was used to collect scattered light, the imaged size of one pixel corresponds to 43 μm. At a 32×32 pixel interrogation window with 50% overlap, this resulted in a vector spacing of 0.69 mm. This suffices to resolve the longitudinal and transversal Taylor length scales (which are between 1 mm and 2 mm at z=60 mm for the Reynolds numbers considered) but not for the Kolmogorov length scale in the jet which is estimated at 0.1 mm [77]. The time interval between the two laser pulses was 30 μs at a jet Reynolds number of 4100, 20 μs for the DNG 4.5 case and 18 μs for the other two cases.

Davis 7.4 was used for the image acquisition and the post-processing. Processing of the raw images was done with multiple cross-correlation passes (3 times at a 64x64 window, 2 times at the final 32x32 window). A reference velocity field of +6 m/s was given to aid in the post-processing. A median filter was applied to detect and replace outliers. The rms of the error in axial velocity in the coflow is roughly 0.35 m/s at a shot interval of 30 μs and 0.5 m/s at a shot interval of 18 μs (based on the known rms values from LDA measurements, which are much lower). These values correspond to 0.1 and 0.15 pixel

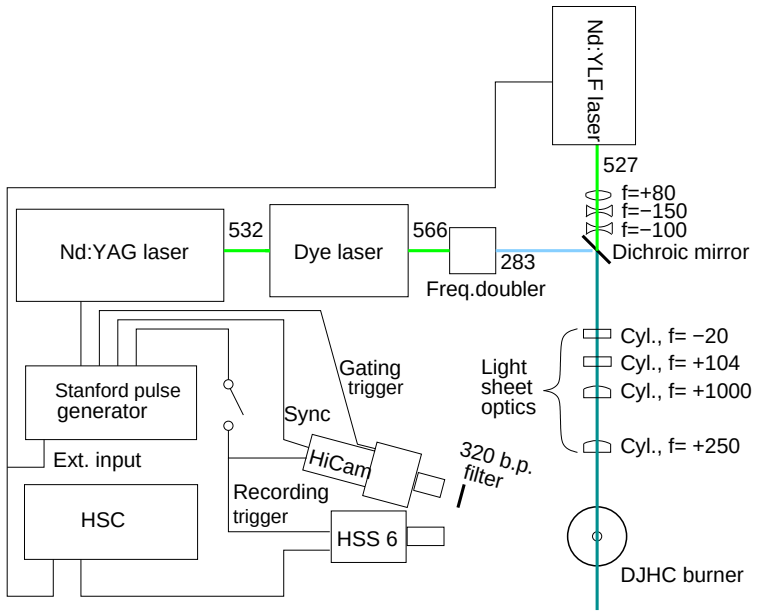

Figure 5.4: Schematic overview of the optical setup for the combined PIV and OH-PLIF measurements.

displacements, a reasonable value for PIV measurements ([97], p.164-176). The strains and vorticity were calculated with a central differencing scheme. For the vorticity and normal strains, the error level is estimated at around 350 $1/s$ and 500 $1/s$ for the longer and shorter interval, respectively. For the comparison between LDA and PIV (Section 5.3) and the conditioned data (Section 5.5), no smoothing was applied. Smoothing with a 3×3 kernel was however applied for the conditional flow properties (Section 5.4), to reduce variances and statistical error in the coflow region, because of the smaller size of the conditional data. The PIV measurements that were used to determine correlation functions in the coflow were done at 500 Hz repetition rate with a 200 μs exposure interval time. This resulted in a noise level (the ratio of the variance due to random error and that due to real fluctuations) of smaller than 10%, judging from spatial correlations.

Uncorrelated vectors were occasionally observed in the PIV fields, despite the outlier detection applied in the Davis software. For the conditioned statistics (Section 5.5), spurious data removal was applied as a post-processing step, outside of the PIV software. The conditioning of the PIV data on the boundary location strongly reduces scatter due to intermittency and generates data with a more symmetric distribution. After removing the unvalidated vectors from the data set, data points with a distance of more than three standard deviations from the median were removed. Generally, statistics (mean and variance) were only calculated for data sets of which less than 10% was removed (because of unvalidated vectors or outliers) to avoid statistical bias. The conditioned data set sizes were in the order of several thousand values per local coordinate points.

In principle, in a flow with temperature gradients, thermophoresis has an effect on small particles, such that the particle velocity is not equal to the flow velocity. This was elaborated on in Hasselbrink et al. [98], who concluded that in the presence of temperature gradients of 2000 K/mm, seeding particles such as used here can experience a differential velocity of 0.15 m/s. As the mean temperature gradients in the coflow are more than an order of magnitude smaller, and the temperature difference between burnt and unburnt gases is in the range of several hundred Kelvin, the effect is not relevant compared to that of the error in the PIV data in this study.

5.2.4 OH-PLIF system and data processing

OH-PLIF images were taken simultaneously with the PIV recordings but at 10 Hz. Therefore, only one out of ten PIV fields could be used for conditional statistics. The OH-PLIF laser pulse was temporally centred between the two PIV pulses. The UV-light was generated by a Spectra Physics PRO250-10 Nd:YAG laser, pumping a Syrah PrecisionScan dye laser at 532 nm. The dye laser was operated with Rhodamine 590, generating light at 565.8 nm which was frequency-doubled to 282.9 nm, to excite the $Q_1(6)$ line of the $A^2\Sigma^+$ - $X^2\Pi$ (1,0) transition. The pulse energy at 282.9 nm was 10 mJ. The sheet was made 40 mm high with a thickness of 0.6 mm by the same optics as those of the PIV system, see Fig. 5.4. Overlapping of the LIF sheet with the PIV sheet was done with a dichroic mirror. A Semrock narrow pass filter was used to block elastic scattering. Fluorescence was collected through a 105 mm Nikkor UV lens, and recorded by a Lambert Instruments HI-CAM CR camera, with a resulting imaging resolution of 85 μm per pixel. More details on the optical configuration of the PIV and OH-PLIF system are provided in [99]. A background image (with identical settings but no laser pulse) was subtracted from the images, and the pictures where smoothed with a Gaussian kernel with a FWHM of 8 pixels ($\sim$ 0.7 mm). Per case, 270 simultaneous OH-PLIF and PIV images are recorded for conditional statistics. The full PIV dataset is ten times larger, containing 2700 fields, which are used for unconditional statistics.

5.3 Flowfield and length scales

5.3.1 Velocity profiles

The velocity field has previously been measured with LDA. These results are described in detail in [77]. For comparison with these data, the results from the PIV measurements at z=60 mm are shown together with the previous LDA results in Fig. 5.5. Both the mean axial velocity field and the Reynolds stresses are in good agreement with earlier obtained LDA data. On the centreline, deviations between the PIV and the LDA values for the mean axial velocity and the velocity variances are 5% or less. In the coflow region (r between 10 mm and 20 mm), the mean axial velocity differs by less than 5%, and the mean radial

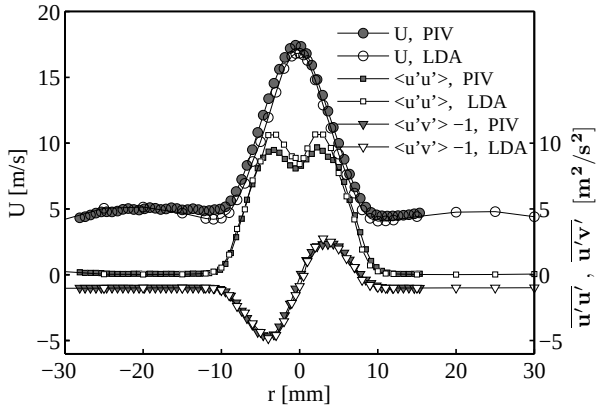

Figure 5.5: The mean velocity U and the Reynolds stresses $\overline{u'u'}$ and $\overline{u'v'}$ at z=60 mm, at a jet Reynolds number of 4100, as obtained with PIV (closed symbols) and LDA (open symbols). Note that 1 m^2s^{-2} was subtracted from the values of $\overline{u'v'}$ for clarity.

velocity by less than 25%.

5.3.2 Length scales

The length scales of the flow field have been determined previously with LDA, by taking autocorrelations of long time series and applying Taylor's hypothesis [77]. These are compared here with spatial correlation functions that are computed from the PIV data. This was done by correlating axial velocities at z with those at $z + \Delta z$ and normalising these with the square root of the product of the local variances:

$$\frac{\overline{u'(z)\, u'(z+\Delta z)}}{\sqrt{\overline{u'(z)^2}}\,\sqrt{\overline{u'(z+\Delta z)^2}}}\,. \tag{5.1}$$

Spatial and temporal separations were converted into each other using the local mean velocity, again using Taylor's hypothesis. The results at (z, r)=(60,0) mm are shown in Fig. 5.6 (top). The agreement between the two correlations is very good.

At (z, r)=(60,-11) mm, Fig. 5.6 (bottom), the deviations are much larger. The LDA measurements do not indicate a strong increase in length scales compared to the centreline, unlike the PIV values. It is remarkable that the correlation in the PIV measurements is higher than that in the LDA measurements, despite the higher noise level of the PIV measurements. The origin of the differences is not completely clear, a possible explanation might be found in the strong intermittency (at the mean jet interface, the flow alternates between being highly rotational and nearly irrotational), invalidating Taylor's hypothesis. Consider for instance a straight interface that separates two homogeneous regions and fluctuates in the opposite direction of the flow in an irregular manner. The streamwise spatial

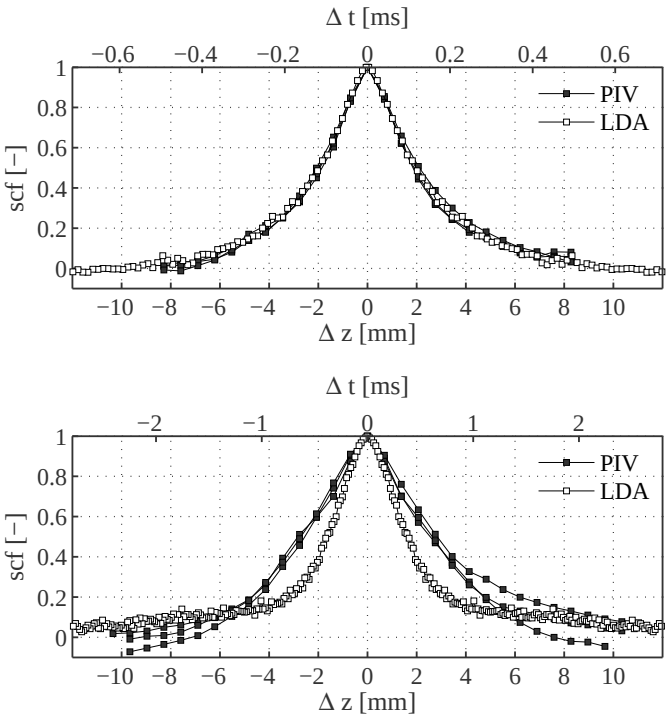

Figure 5.6: Spatial and temporal correlation as determined with LDA and PIV at z=60 mm. Top figure: r=0 (the 3 curves of the PIV data correspond to r=-0.5 mm, 0.2 and 0.9 mm), bottom figure: r=-11 (the 3 PIV curves correspond to r=-11.6, 10.9 and 10.2 mm. The conversion of temporal to spatial separations and vice versa was done using the mean axial velocity (Taylor's hypothesis).

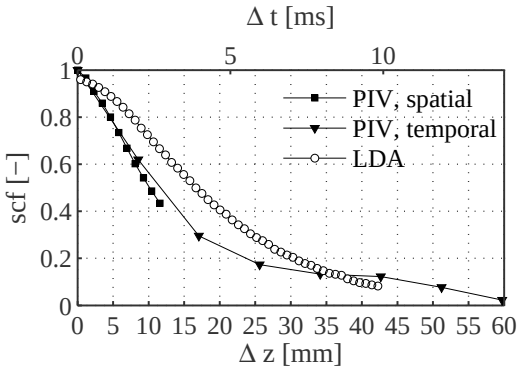

Figure 5.7: Spatial and temporal autocorrelation functions in the coflow as determined with LDA at (z, r)=(30,15) mm and PIV at (z, r)=(25,-15) mm. The PIV correlations were determined by calculating spatial correlations, and by calculating temporal correlations.

correlation would still be perfect, whereas the temporal correlation on the mean interface location is not.

The length scales at (z, r)=(25,-15) mm were also determined from the PIV data, using two different methods. Firstly, by calculating the temporal autocorrelation in a single point (measurements were taken at 500 Hz) and converting this autocorrelation to a spatial correlation, and secondly by determining the spatial correlation directly from Eq. 5.1. These two methods result in similar values. The agreement with the LDA data (taken at (z, r)=(30,-15) mm) is qualitatively reasonable, as shown in Fig. 5.7, but not very close. The autocorrelation functions taken from the PIV measurements do however vary strongly as a function of where they are determined in the coflow, and are not identical for positive and negative radial locations. This might also be a consequence of the relatively short measurement time of 4 s. The differences between LDA and PIV are therefore rather due to non-perfect reproducibility than due to measurement error. The correlation length exceeds the typical dimension of the geometry, implying fluctuations of an instationary nature, rather than the action of turbulent eddies.

The Taylor-scale Reynolds number Re_λ of the coflow in its centre region at z=3 mm is close to unity (based on the rms of the axial velocity fluctuations, $\sim$ 0.10 m/s, a kinematic viscosity of approximately 200×10^{-6}m^2/s and a Taylor length scale in the order of ten mm). The coflow stream can therefore not be classified as truly turbulent. For instance, in grid turbulence the normalised dissipation rate achieves a steady value above Re_λ=50 but has an inverse relationship with Re_λ for $\mathrm{Re}_\lambda < 10$ [100].

5.4 Conditional velocity statistics

5.4.1 OH-PLIF signal strength as flame indicator

In this paper, the OH fluorescence intensity is used to determine whether a region in space is chemically reactive or not. For this purpose, a range of radical species can be probed, each with their own specific relation to the flame. For instance, the formaldehyde radical H2CO indicates earlier stages of autoignition in hydrocarbon fuels, and its co-existence with OH has been suggested as a measure for the local reaction rate [101, 56]. The CH radical forms an indicator of fuel decomposition reactions on the rich side of the flame. Its contours are found to be narrower than that of OH, and are observed to lie very close to the OH contours, but on the fuel-rich side [92, 102]. The OH radical is not only present in regions with high reaction rates, as it survives relatively long in the post-flame region. Because the focus in this study is on the region where flame pockets are first formed, the OH radical will nevertheless provide a clear distinction between regions where no reaction has occurred yet and regions where conversion of the reactants takes place or has taken place. A quantitative measurement of the OH number density is not undertaken here. Conversion of the camera signal count into OH number densities requires careful consideration of, amongst others, laser light sheet intensity, temperature dependence of transitions, quenching effects, and the sensitivity of the imaging setup [103]. A recent study [104] shows that the latter is not trivial when an intensified high-speed camera is used. For instance, the time- and temperature dependent and non-linear response should be dealt with.

For the limited purpose of flame detection the demands on the OH measurements are less strict. Spatial inhomogeneity of the laser light sheet was minimized in this study by making the light sheet approximately twice as high (in z-direction) as the region of interest. Thresholding was applied to distinguish the flame regions from non-flame regions. To investigate which threshold level might be appropriate, the distribution of OH signal counts was studied. Figure 5.8 shows the complementary cumulative density function CCDF, (which is defined as the probability that a value is exceeded) plotted logarithmically against the number of counts. It is linear over a large extent indicating an exponential distribution. A break in the slope is seen at a count level of roughly 15. The part below this value corresponds to the weak OH-PLIF signal in the hot coflow. The part above this value is related to the presence of flame zones. An OH signal count of 30 was chosen as the default threshold value to distinguish reactive from non-reactive regions. This threshold results also in a satisfactory visual division between “flame” and “no-flame” zones. In fact, any threshold value between 25 and 40 can be chosen, with negligible impact on the conditional and conditioned velocity and vorticity profiles. For convenience, regions with OH-levels exceeding the threshold value will be called “flame zones”, although the OH-rich regions do not cover the entire zone where reactions take place.

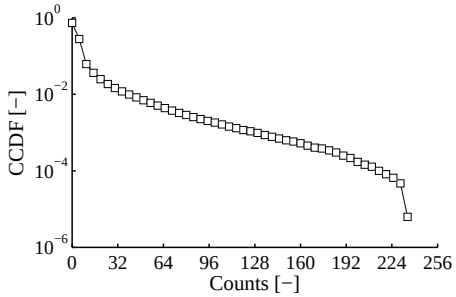

Figure 5.8: The CCDF of the number of counts of the OH signal, for all OH statistics at z=70 mm, case DNG 4.5.

5.4.2 Visual and OH-PLIF observations

Although a somewhat crude indicator, the seeding particle density can be used to indicate the material interface of a jet. The position of the flame zone relatively to the jet can thus be visualised when the raw PIV images are overlaid on the OH-PLIF images. For this purpose, recordings were made with a strongly seeded jet and a barely seeded coflow. The resulting images are shown in Fig. 5.9. It is seen that OH-rich regions (flame zones) are located outside the regions where seeding particles, originating from the fuel jet, are found.

Figure 5.10 shows superimposed, simultaneous seeding- and OH-PLIF images in greater detail. The spatial separation between the flame and the seeding regions is again evident.

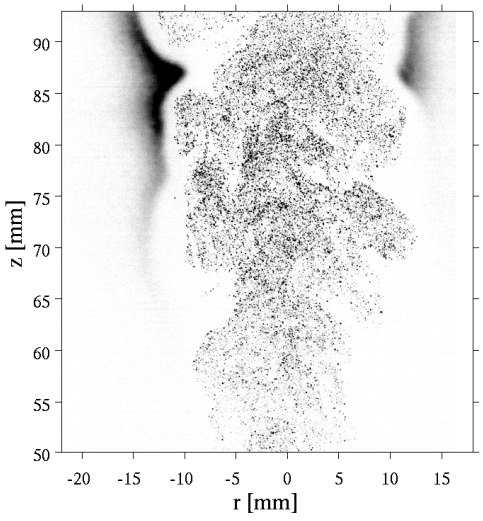

Figure 5.9: The raw image from the PIV camera superimposed on the PLIF image, DNG 4.5 case ($\mathrm{Re_{jet}}$=8800). The PLIF sheet is somewhat higher for visualisation purposes.

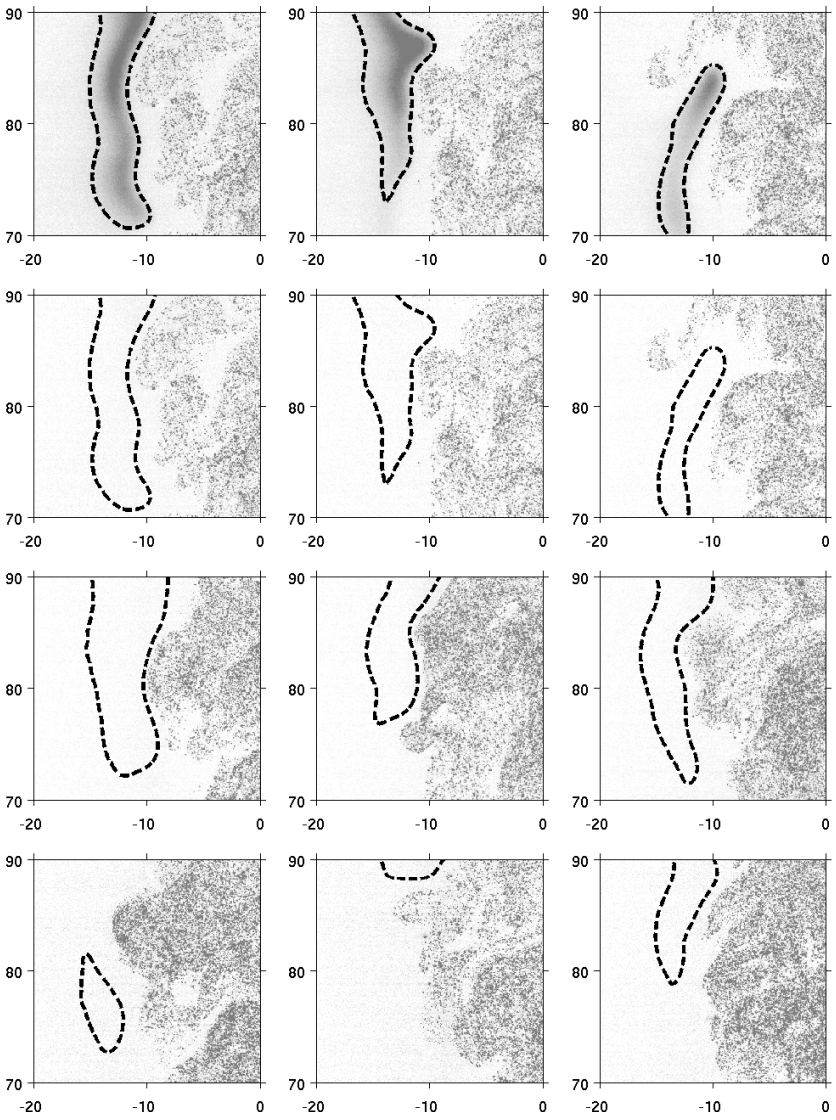

Figure 5.10: Nine simultaneous OH-PLIF and seeding snapshots. The upper three figures have the OH-PLIF and seeding images superimposed, to illustrate how the threshold criterion functions to detect flame zones. Below, only the detected flame contours are shown, to make the distinction between the seeding and flame zones more clearly. The upper row and the second row from the top represent identical images. Note that the flame zones are folded closely to, but always outside, the seeded part of the jet.

5.4.3 Conditional and unconditional flow field

The mean axial and radial velocities, both unconditional and conditional on flame presence, are compared in Fig. 5.11. The conditional statistics are plotted with error bars, that have a total length of two times the rms divided by the square root of the number of data points, to indicate the statistical uncertainty. The flame probability (the fraction of images that contains an identified flame at z=65 mm as a function of r) is also shown in Fig. 5.11a. Note that the case DNG 4.5 suffers from some left-right asymmetry.

The axial velocity is somewhat smaller when conditioned on flame presence, but the largest differences are seen in the radial velocities. Regions with strong OH signals move laterally inward faster than regions without, close to the centreline. This is due to the entrainment at the jet interface: ambient fluid is carried toward the jet, whereas the fluid that is part of the jet moves outward rather than inward, causing spreading of the jet. This strong correlation between radical species concentration and radial velocity is directly related to the turbulent scalar flux of the species concentration, and to that of the mixture fraction. Note that the error bars in Fig. 5.11b are relatively large, because of the small mean radial velocity and smaller conditional sample size. The conditional and unconditional mean vorticity is shown in Fig. 5.12. A drastic difference is seen here. Conditional on flame presence, the magnitude of the vorticity remains close to the low values of the coflow, apparently unaffected by the jet.

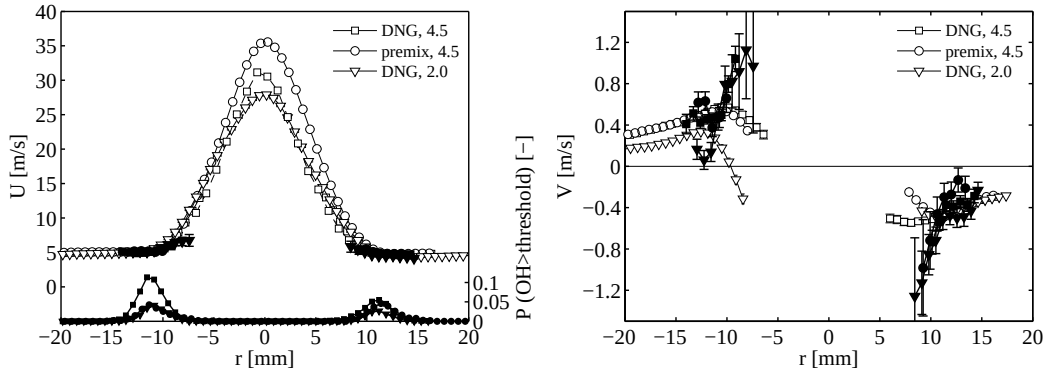

(a) Mean axial velocity and flame probability at z=65 mm.

(b) Mean radial velocity.

Figure 5.11: Unconditional (open symbols) and conditional (solid symbols) axial and radial velocities, at z=65 mm. The lower graphs in Fig. 5.11a correspond to the right axis and indicate the probability of flame presence at z=65 mm. For the DNG 4.5 case, LDA measurements at z=60 mm were added.

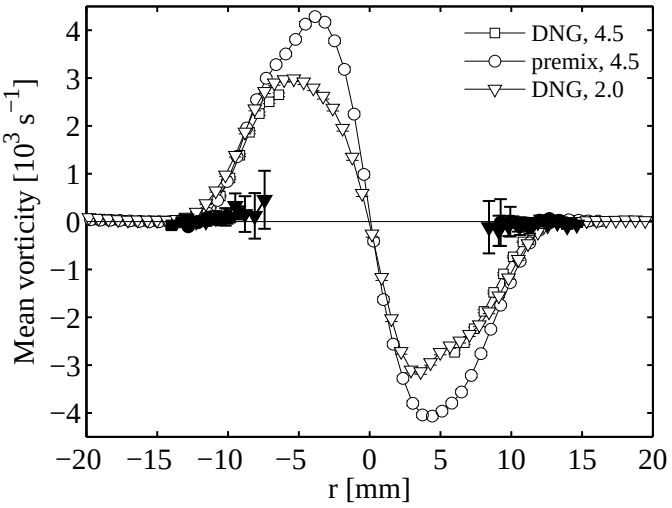

Figure 5.12: The mean vorticity at z=65 mm, unconditional (open symbols) and conditional (solid symbols).

5.5 Conditioned velocity field

In this section, the flow field in the neighbourhood of flame zones is investigated by introducing local coordinate systems attached to the instantaneous flame zones. The reason for this approach is that both the flame zones and the velocity field get transported by the same large turbulent structures. Therefore, by conditioning on the flame zone location, the "smearing" effect due to large scale turbulent motions is undone, and a sharper picture of the local velocity field emerges even when this velocity field is averaged. The orientation and the origin of the local coordinate systems are determined based on the OH-PLIF images, as elaborated in the following.

5.5.1 Methodology

In addition to intermittently appearing strong OH signals from flame zones, a certain minimum level of OH appears to be always present in the coflow. This is caused by the high temperatures, such that the equilibrium concentrations are sufficiently high to be detected. Whereas this "background" OH signal is found throughout most of the coflow, it drops sharply to a near-zero value close to the jet/coflow interface. Apparently, the OH radicals in the coflow fluid are destroyed very quickly as this fluid is entrained, which is due to the chain terminating reactions occurring in fuel-rich regions [105]. This is confirmed by the disappearing of the sharp interface between the coflow and jet fluid when air is supplied through the central jet instead of methane or natural gas. The interface is therefore an indicator for the material interface of the jet, separating low- and high mixture fraction regions. Due to its sharpness, it provides a convenient reference frame for the conditioning.

The OH-PLIF data is thus used not only to identify the flame region, but also to identify the jet boundary. This is done with a much lower threshold level (11 counts) that was chosen based on visual inspection. The resulting boundary is indicated by the dashed line, in the top figure of Fig. 5.13. The arrays of r- and z-coordinates that describe the interface are each smoothed using a rectangular window with a length of 11 pixels ($\sim$ 1.0 mm) to reduce the effects of the pixel quantisation. A material interface is detected in each image, both near to and far from regions with high OH-PLIF intensities.

A problem of using this interface directly for the conditioning is that the location of the interface is influenced by the presence of nearby strong OH signals due to blurring of the image intensifier and, to a lesser extent, by the image smoothing. This is confirmed by inspection of statistics conditional on the presence and the absence of flame zones at a height of 70 mm. The interface is seen to be located on average 1.5 mm more radially inward conditional on flame presence. Despite the disturbing effect of strong OH signals on the location of the perceived interface, the orientation of the interface appears nevertheless to be well correlated with that of the OH contours. The direction of the normal to the interface is therefore used as a coordinate axis for the conditioning, its origin is however not based on the location of the interface, but on the OH profile along the normal.

This is done by first normalising the OH-PLIF values along the normal between zero and one. The origin is shifted such that the normalised intensity value of 0.5 is located at s=0. The non-integer shift is accomplished by performing interpolation along the profiles. This normalisation procedure is shown in Fig. 5.14. The regions of the flame zone closest to the jet (roughly from s=-1 mm to 1 mm) lie very close together, such that s=0 forms a good measure for the fuel-rich edge of the flame-contour. The white dots in the bottom figure of Fig. 5.13 indicate s=0 for the shown profiles. Finally, arrays of global coordinates are calculated (the dots in the lower two figures of Fig. 5.13) that correspond to points on an axis s, onto which the OH and PIV values are interpolated linearly. Values of s increase from the oxidiser side toward the fuel side.

Note that the reported thicknesses and distances are *projected* thicknesses and distances. In measurements on non-reacting turbulent jets, actual (three-dimensional) thicknesses were shown to be on average around 20% smaller than the measured two-dimensional counterparts [106]. The real thickness of the OH-contours is thus expected to be smaller than the displayed thickness, not only due to the effect of smearing but also due to the fact that the sections through the OH-structures do not always follow the shortest path.

Summarising, a hybrid approach is used to generate local coordinate systems, combining the spatial information on both a low-level OH signal threshold (which can be interpreted as the material interface, albeit possibly shifted due to stronger OH signals) to give the orientation, and on a higher-level threshold, that determines the origin of these local coordinate systems. The benefit of this combination is that it avoids directional ambiguity (the perceived interface always runs from the bottom to the top of the image thereby separating the jet region from the coflow region, whereas the identified flame contours do not). Furthermore, the wrinkling of the flame contours is captured, providing a more realistic

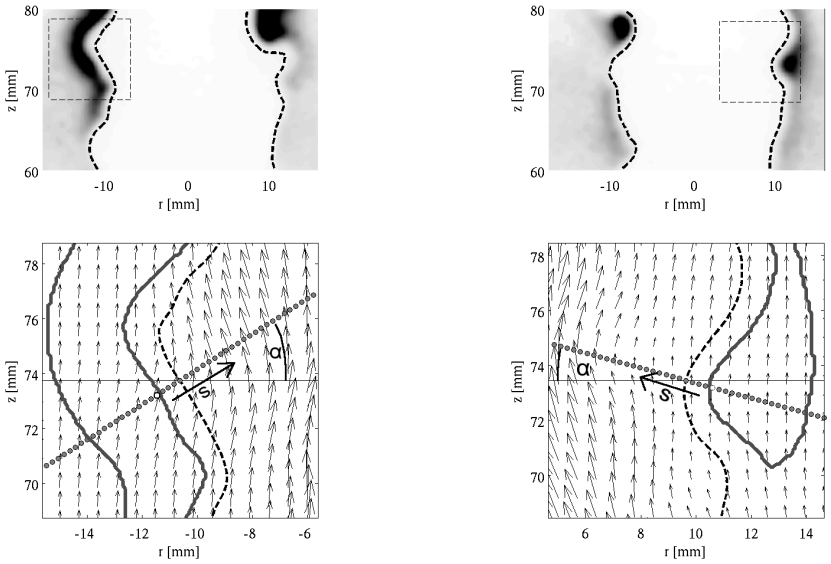

(a) (b)

Figure 5.13: Top two figures: instantaneous OH-PLIF images, with the jet boundary indicated by the dashed line. The region in the box is enlarged in the two lower figures, showing the velocity vectors, the jet boundary (dashed line) and the region which is recognised as a flame zone (grey thick line). The grey dots indicate the local coordinate s which is directed normal to the jet boundary, with 0.25 mm increments. This is the grid upon which the velocity field is interpolated to study the local velocity statistics (the conditioned velocity field). The origin of s is indicated by the white dots, the positive direction of s runs towards the side of the jet. The positive direction of angles in this local coordinate system is indicated by the angle α.

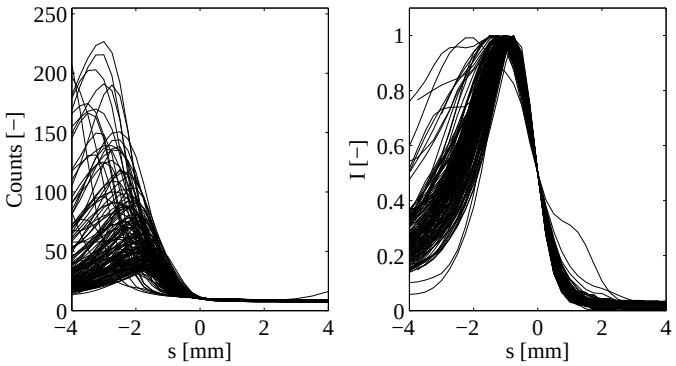

Figure 5.14: The OH-PLIF profiles of 150 curves in the local coordinate s, before (left) and after (right) normalisation.

measure for the distance from the flame zone boundary.

5.5.2 Interface statistics

Statistics of the material interface can be obtained by only considering the interface, i.e., conditionally on the *absence* of a strong OH signal, such that it is not disturbed by blurring of nearby strong signals. For the statistics to be valid for the (unconditional) jet-coflow interface, the presence of flame zones should be uncorrelated with the statistics of this interface. The absence of correlation cannot be verified, but the statistics briefly discussed in this section are all based on this assumption. The mean jet radii, as given earlier in Table 5.1, were determined by taking the conditional mean of the interface, at z=70 mm. By determining mean radii at several heights, the spreading rate of the jet could be determined, which was in all cases close to 0.14. As a comparison, the value of the spreading rate of jets (based on scalar measurements) is approximately 0.11, for a wide range of density differences [107]. In these experiments, the jet half-width was however calculated as the point where the mean scalar concentration is half of that on the centreline.

The mean slope conditional on the *presence* of detected flame zones is strongly different from the previously determined slope, and is even slightly negative at approximately -0.02 to -0.05. This is caused by the fact that the OH statistics vary within the observation window (probability of detecting a flame zone increases with z), and that therefore the probability of finding a trailing edge of a flame within the considered height is larger than that of finding a leading edge.

An interesting characteristic of the interface is its wrinkledness, that is, the mean path length of the interface, compared to the length of the mean interface. This cannot be calculated by conventional methods (i.e., following the entire interface curve for each frame), because of the distorting effect of the strong OH signals in the flame zones. It can however be reconstructed from the conditional interface statistics, by looking at the scatter of the orientation vectors. Visually, this would be done by placing all interface orientation vec-

tors of unit length head-to-tail, and dividing their cumulative length through the number of vectors. Mathematically, this can be written down succinctly using complex notation. The "alignment" of vectors is then given by

$$\alpha' = \mathrm{abs}\left[\overline{\exp(i\,\alpha_{no})}\right] \ , \tag{5.2}$$

where α_{no} indicates the surface angle that is determined conditional on the absence of strong OH signals along s. α' has value one when all vectors point in the identical direction, and is zero when the angles are divided evenly. The estimated wrinkledness is $1/\alpha' = 1.10$ for all cases. In agreement with observations, the interface is not corrugated strongly. For a fractal structure, the total length is, up to a certain point, dependent on the level of detail with which the curve is observed. In this case, the smallest physical details appear to be in the order of one millimetre, i.e., further zooming in will not increase the wrinkledness.

5.5.3 Local velocities

The axial and radial velocities determine for a large part the mean transport of scalars. The axial velocity is of particular relevance to the downstream transport of newly formed flame pockets. The radial velocity determines the entrainment of coflow fluid, which brings hot oxidiser toward the fuel stream. These velocities, conditioned on the distance from the normalised OH profile, are shown in Fig. 5.15. The axial velocity at the peak of the OH contour is hardly influenced by that of the jet. The radial velocity is seen to be directed toward the centre line, and peaks at the fuel-rich side of the flame region (s>0). This peak is not as high as that of the conditional mean radial velocity (Fig. 5.11). The radial velocity thus depends more strongly on the radial location of the flame zone, than on the relative location within the flame zone. The axial velocity is almost constant within the complete flame region, assuming the value of the coflow velocity. When normalised with the local jet centreline velocity, the coflow velocity and the mean jet radius, the profiles become very similar. It is seen that the profiles of the premixed flame lie somewhat closer to the flame. It is tempting to attribute this to the different stoichiometry of the fuel. The difference is however rather small (~ 0.5mm).

5.5.4 Vorticity and enstrophy

Fig. 5.16a shows the conditioned vorticity field, as a function of the distance s. The vorticity is positive in the direction of positive angles in the local coordinate system (see α in Fig. 5.13), such that the counter-clockwise rotation for the global coordinate $r < 0$, and a clockwise rotation at $r > 0$ are both counted as positive. It is seen that in all three cases, the mean vorticity near the centre of the flame zones is identical to that further into the coflow, with a value very close to zero. When normalised with the local jet width and the centreline velocity, the profiles again become comparable, the premixed case being again somewhat closer towards the flame region. Note that the curve of the mean vorticity of case

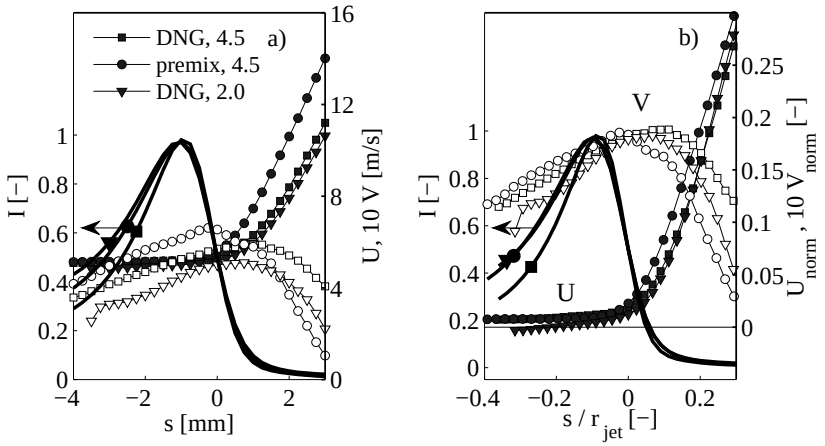

Figure 5.15: The radial and axial velocities, for the three cases. The thick line indicates the mean normalised OH profile. The open symbols correspond to the radial velocity V the closed symbols correspond to the axial velocity U. In the figure at the right hand side, the velocities are normalised. The normalisation of V is $V_{\rm norm} = V/U_{jet}$, U is normalised as $U_{\rm norm} = (U - U_{co})\,(U_{jet} - U_{co})^{-1}$.

DNG 2.0 in Fig. 5.16b, is partially obscured by that of case DNG 4.5. Comparing with the non-conditioned vorticity profiles (Fig. 5.12), the conditioning is successful in reducing the smearing effect of the large scale structures: the mean vorticity profile is around four times steeper when conditioned on the location of the flame zones.

The conditioned enstrophy (here taken as the mean square of the vorticity fluctuations) is very small for $s < -0.5$ mm (typically $160 \times 10^3 \mathrm{s}^{-2}$ without smoothing and $60 \times 10^3 \mathrm{s}^{-2}$ with smoothing), whereas it increases strongly for $s > 0$ (to over $8 \times 10^6 \mathrm{s}^{-2}$ at s=3 mm in all cases without smoothing, $6 \times 10^6 \mathrm{s}^{-2}$ with smoothing). Since the smallest scales of the turbulent flow are not resolved, the values in the turbulent jet can be considered to be lower estimates.

5.5.5 Strain rates

The local strain rate is a key quantity in chemistry-turbulence interaction. Strains that are compressive in the direction of the scalar gradients, act to augment these gradients. In the infinitely fast chemistry limit, the instantaneous reaction rate is proportional to the square of the mixture fraction gradient [108]. On the other hand, when the chemistry time scales are of the same order of magnitude as the diffusive time scales (commonly expressed as the inverse of the scalar dissipation rate), extinction might occur. Also, autoignition might be inhibited by large strains, as was first derived by means of an asymptotic analysis by Liñan et al. [109]. Of interest to the studied flames is therefore the local strain rate, i.e.,

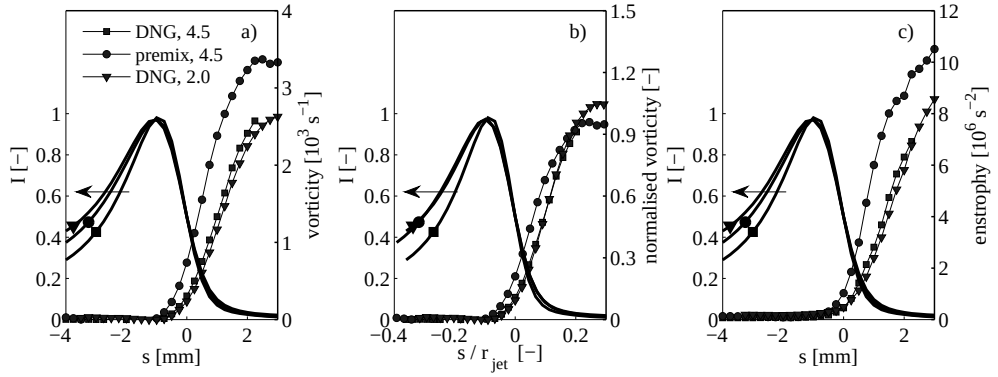

Figure 5.16: The mean conditioned vorticity (a), the normalised mean vorticity (b) and the enstrophy (c), along with the normalised mean OH signal. The vorticity was normalised with the local centreline jet velocity and the mean radial distance of the material interface: $\omega_{\mathrm{norm}} = \omega\, r_{\mathrm{jet}}/U_{\mathrm{jet}}$.

the compression or extension of the flame surface. To facilitate the analysis of the local flow field, the symmetric part of the instantaneous velocity gradient tensor (the strain rate tensor) is diagonalised, such that instead of three strains in the laboratory coordinates (e_{xx}, e_{xy} and e_{yy}) two principle strains (ϵ_1 and ϵ_2) and the angle θ_1 of the largest principle strain are obtained. Next, the diagonalised strain tensor can be rotated in the direction of the normal of the interface over an angle $\phi = \alpha - \theta_1$ to obtain the value of the strain normal to the interface, e_{11}. The intermediate step (resulting in the principle strains and the direction of the most extensional strain) is useful, because of the clear physical interpretation of the difference between the two angles α and θ, as the alignment between the direction of flow deformation and the gradient of the scalar field.

As a first step of the analysis, the statistics of the principle strain angle are examined. When dealing with the statistics of the principal axes, standard methods of averaging will not work because of the circular periodicity. That is, the average of a set of angles is in general dependent on the choice of the reference angle. For instance, the average of the two angles 10° and 350° would be calculated as 180° instead of 0°. This problem can be solved by adding the vectors corresponding to the angles and calculating the angle of the resulting vector. In this case the periodicity of the principal axis over 1 π radians must also be taken into account. This is achieved by the following operations on the angle θ. First, the angular values are evaluated modulo π and stretched to the full unit circle:

$$\tau = 2\,(\theta \bmod \pi)\ , \tag{5.3}$$

after which the vectors are averaged. Written as an averaging operation in the complex plane (as was done earlier in Eq. 5.2), two quantities can be obtained:

$$\overline{\tau} = \arg\left[\overline{\exp(i\,\tau)}\right] \qquad \text{and } \tau' = \mathrm{abs}\left[\overline{\exp(i\,\tau)}\right]\ . \tag{5.4}$$

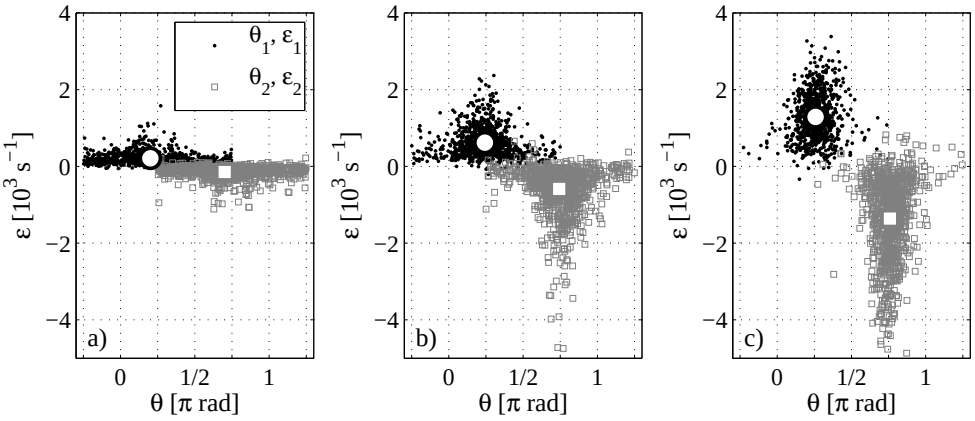

Figure 5.17: Scatter plot of θ_1 with ϵ_1 and θ_2 with ϵ_2, at s=-3 mm, 0 mm and 2 mm. The large markers indicate the mean values. θ_1 is plotted modulo π, centred around $\pi/4$. Values of θ_2 (the angle of the most compressive direction) are, by definition, shifted by $\pi/2$ with respect to θ_1. Case DNG 4.5.

The first term is the angle of the average vector in the complex plane. The second term can be interpreted as a measure for the angular scatter, as explained earlier. As a final step, $\overline{\theta}_1$ is calculated from $\overline{\tau}$ by division by two. The statistics of θ and the principle strains are shown in Fig. 5.17, for three values of s. The largest extensional strain is on average directed obliquely into the jet (the principal direction θ_1 is within 10% of $\pi/4$), which is a pure shear deformation in the original (r, z) coordinate system. The variation is relatively small, especially for $s > 0$ (the value of τ' in Eq. 5.4 equals 0.8 at s=2). The larger scatter in θ_1 for $s < 0$ is attributable to a larger relative error in the PIV measurements. The deformation of the flame interface is thus mainly a shearing deformation.

The variation of the principal angle and principal strains for the three cases, as a function of s is displayed in Fig. 5.18. Note that the strain curves of DNG 4.5 and DNG 2.0 lie on top of each other in the left figure, obscuring the results of case DNG 4.5.

For the flame zone, naturally, the local statistics of the stretch or compression are relevant. Rotation of the strain tensor from the principal angle to the normal of the interface α will yield the local normal strain:

$$e_{11} = \epsilon_1 \cos^2(\phi) + \epsilon_2 \sin^2(\phi) = \sin^2(\phi)\,(\epsilon_2 - \epsilon_1) + \epsilon_1\ , \tag{5.5}$$

with ϕ the difference between θ_1 and α. Because of the linearity of the squared sine function around $\pi/4$, and the small fluctuations in the angles, this can be approximated by: $\overline{e_{11}} \approx 0.5\,(\overline{\epsilon_2} + \overline{\epsilon_1})$. For axisymmetric, incompressible problems, continuity requires that the sum of the normal stresses plus the term V/r is zero (see for instance [110], pg. 78). The latter term is found to be an order of magnitude smaller that the normal stresses. Ignoring the relatively small density differences in the continuity equation, it follows that the absolute value of e_{11} is much smaller than the absolute values of e_1 and e_2.

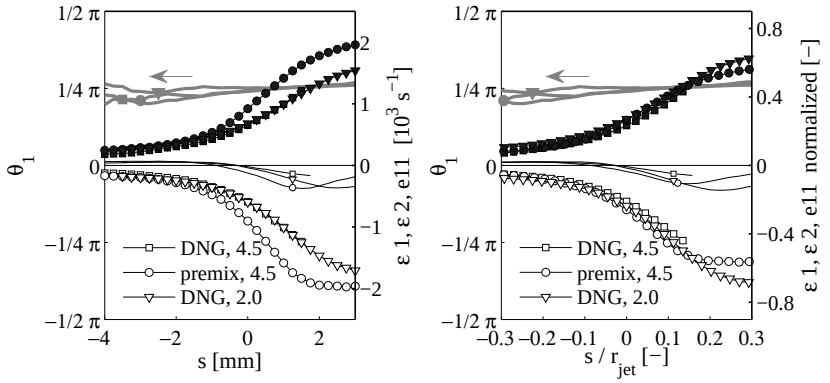

Figure 5.18: The mean of the principal angle θ_1 (solid grey line, left axis) and the mean value of the principle strains ϵ_1 (closed symbols) and ϵ_2 (open symbols). The mean conditioned normal strain is indicated by the thin lines. In the right figure, the distance is normalised, and the strains are normalised by $\epsilon_{\rm norm} = \epsilon\, r_{\rm jet}/U_{\rm jet}$.

That the mean normal strain is very small compared to the principal strains is confirmed by the thin lines in Fig. 5.18. Only for larger values of s, does the normal strain on average become compressive. The maximum average compressive stress is 380 s^{-1} at s=1.5 mm, for the case premix 4.5. The mean deformation in the direction of the interface at $s < 0$ is thus neither strongly (compared to the magnitude of the normal stresses) compressive nor extensional. The normalised correlation between α and θ peaks in all cases at s=2.75 mm, and is rather moderate, between 0.16 (case DNG, 2.0 mm) and 0.23 (premixed case). The probability distribution of the normal strain is rather symmetric around zero normal strain, and becomes much wider for larger values of s. The pdf's of the strain normal to the flame surface, at three different values of s, are shown in Fig. 5.19. Comparing with Fig. 5.17, the stronger extremes in principal strain are due to an increase in normal strains, whereas the scatter in principal angle actually decreases. At s=0, the 10^{th} percentile of the compressive strain lies between $-1 \times 10^3\ s^{-1}$ (case DNG 4.5) and $-1.5 \times 10^3\ s^{-1}$ (case premixed 4.5).

To investigate the influence of spatial resolution, the normal strains were also computed for the smoothed PIV fields, and compared with the presented, non-smoothed results. The ratio of the rms of normal strain determined with the non-smoothed and smoothed data has a minimum at s=0, with a value of 1.2. There are two reasons that smoothing reduces variance in strain fields. Firstly, noise resulting from the random error is reduced and secondly, strains occurring on smaller length scales are filtered out. Taking into account the sharp division of the flow field left and right from s=0, it is expected that the rms of the normal strain of the non-smoothed data are somewhat overestimated for $s < 0$ due to noise (the smoothed fields result in a 35% lower mean value of ϵ_{11} at $s = -1$). In the direction toward the jet, it could both be over- and underestimated, depending on the relative contribution of the noise and the cut-off of the dissipation spectrum due to the

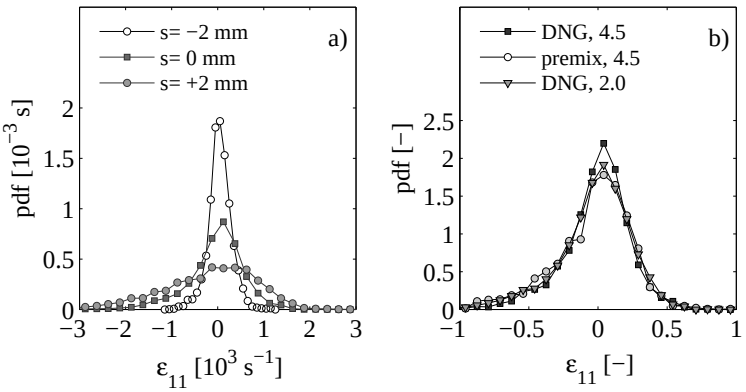

Figure 5.19: Pdf's of the value of the strain normal to the flame contour (negative strain is compressive), at three locations, case DNG 4.5 (a), and pdf's of the normalised normal strain at s=0, three cases (b). The strain is again normalised by $\epsilon_{\mathrm{norm}} = \epsilon\, r_{\mathrm{jet}}/U_{\mathrm{jet}}$.

limited spatial resolution. At $s = 2$, smoothing results in a reduction in the mean value of ϵ_{11} of 25%.

5.5.6 Evaluation and discussion of the results

In this section, velocity statistics were explored in a local coordinate system with distances relative to the OH signal profile. Despite variations in fuel composition and nozzle diameter, the results for all cases were very similar.

The statistics within the flame zone differed strongly from those closer to the jet. For $s < 0$, the vorticity was very small compared to that a mere one millimetre (around a tenth of the mean jet radius) further into the jet region. Related to this, the axial velocity is constant for $s < 0$, but increases quickly for $s > 0$. Apart from the principle strains, that are clearly influenced by the jet for $s < 0$, the flow field at the observed flame contours is governed by that of the coflow. The fuel-rich side of the OH contours ($s > 0$) therefore coincides with a boundary that sharply divides the instantaneous flow field between a turbulent, jet-influenced region and a quasi-laminar, coflow-influenced region.

The fact that the vorticity field changes more steeply than the strain rates from the flame region toward the jet, can be understood from the transport equation of vorticity for constant density flows. Vorticity can diffuse and be intensified by vortex stretching, but not be produced by pressure fluctuations, unlike momentum [111]. Indeed, it is well known that the material interface of a gaseous jet (i.e., a jet with a Schmidt number equal to or below unity) lies outside of the shear layer [90].

The principal strain axis was found to be at an angle of $\pi/4$ radians, or 45 degrees, with a direction radially inward and axially upward. The flame is alternatively compressed and stretched with roughly equal magnitude and probability. At the fuel-rich edge of the flame zones (s=0), compressive strains exceeding $0.5\ U_{\mathrm{jet}} r_{\mathrm{jet}}^{-1}$ (about 1300 s^{-1} in the DNG 4.5

case) are rare, with probabilities below 10 percent.

Although the term "flame zones" was used to indicate regions with strong OH signals, the OH radical does not cover the entire flame zone. Fuel decomposition reactions take place in more fuel-rich regions, where for instance the CH radical is found. Despite the gap between the OH and the CH radical being small (Donbar et al. [102] mention a gap size of 0.5 mm in a conventional non-premixed flame of methane/nitrogen), a strong difference between velocity statistics conditional on OH and CH contours has been reported on the same setup. For instance, at $z/D \approx 17.5$, the vorticity at the OH contours was on average near zero, whereas the mean vorticity at the CH contours was $1.2\ U_{\rm jet}/\delta$ [112]. Here, δ is the full jet width at half the centreline velocity, which is roughly comparable to $r_{\rm jet}$ used here. Also, the CH zones were not aligned with the compressive strain axes at that height, this did however occur at higher locations. The current results are thus very much in line with these previous findings, although they originate from a quite different setup.

Another region of the flame, possibly not covered by the OH regions, is that where autoignition occurs. It is a generally accepted view that this happens at very lean mixture fractions when the oxidiser is heated [37, 45, 56, 44]. Though this might be true for laminar or two-dimensional calculations, it is not clear whether this is always the case in a three-dimensional situation. For instance, the experiments of Gordon et al. [28] show early stages of ignition (i.e., presence of formaldehyde without OH) relatively close to the centreline. Based on their 3D-DNS calculations of a H_2 flame in a heated coflow, Yoo et al. [44] conclude that autoignition nominally occurs on the fuel-lean side but occasionally originates from fuel-rich pockets. Whether the autoignition process in these flames is affected by turbulent small-scale strains or only by the large-scale deformations in the quasi-laminar region, is therefore debatable.

However, considering the steep changes at s=0, it is likely that the fuel rich side of the flame zone is influenced by stronger strains than the lean side. This would explain the observed extinction of flame pockets at higher Reynolds number in the DJHC-V flame [68]. Although not commonly recognised as an extinction mechanism, the shear strain (as opposed to the normal strain) could be responsible for extinction, carrying away the fuel-rich part of the flame faster downstream than the fuel-lean part.

Considering the similarity between enstrophy and dissipation [111], the region where high levels of OH are found, is not the region where turbulent kinetic energy is dissipated, and hence this region is not expected to be governed directly by the local value of the turbulent dissipation rate. Furthermore, the concept of local well-stirredness is not justified: a most characteristic feature is the strong intermittency between the turbulent jet region and the irrotational coflow. Whereas the technique of employing a turbulent timescale to provide a closure for the mean reaction rate based on mean quantities [113, 36] could be questioned for its general applicability, applying it to these flames does not seem a valid approach.

5.6 Implication for scaled flameless combustion experiments

The nature of the reaction zones in the DJHC burner is thus seen to be quite different from that as expected in a furnace operating in flameless combustion mode. In this section, some considerations on the scaling of such a combustion system are discussed.

To stand model for a larger combustion system, some relevant non-dimensional parameters have to be roughly preserved in a scaled combustion experiment. In regime diagrams of non-premixed combustion, usually time and length scales of the flow are considered, and compared with those of the chemistry.

Here, the regime diagram of Law ([22], pg. 511) will be used, which is based on the Reynolds and integral Damköhler number. In the convention of [22] these are named Re_0 and Da_0, with Da_0 the ratio between the integral and the chemical time scale: $Da_0 = \tau_0/\tau_c$. The integral Damköhler number is related to its small-scale counterpart as $Da_0 = \sqrt{Re_0} Da_L$. We will pay attention only to the jet, the length scale of the problem is therefore the nozzle diameter D. Say that the experiment is scaled by a factor S (where a smaller S implies a smaller experiment), but the kinematic viscosity stays constant. Fulfilling geometric similitude, both experiments would be comparable at a height z/D if the integral Reynolds number and integral Damköhler would be similar. To conserve the jet Reynolds number, the jet velocity has to be scaled by a factor $1/S$. To keep the integral Damköhler number identical, the chemical time scale has to be scaled with S^2, i.e., become quadratically smaller compared to the nozzle diameter. The Mach number forms a restraint: roughly at a value of 0.3, compressibility effects become important. Furthermore, buoyancy effects will become much less important as simultaneously, the length scale decreases, and the velocity increases. The requirements for the scaling can be loosened up if the purpose is merely to preserve the combustion regime. For flameless combustion, which presumably operates at $Da_0 \approx 1$ [1] and thus in the distributed reactions regime [15], this would be achieved by scaling down the jet diameter D and keeping the velocity roughly equal (assuring that the jet stays turbulent), since this would make the integral Damköhler number even lower.

The previous arguments were based on the assumption that the relevant flow scales depend on the jet. As seen in the conditional velocity statistics, the length and velocity scales of the coflow stream are most relevant to the flame. In a furnace, the oxidiser stream that surrounds the fuel stream originates from strong coaxial hot air jets and recirculating

[1] Note that a single Damköhler number does not suffice to describe the effects of a change in chemical time scales as a result of preheating and diluting the oxidiser stream. For instance, Oberlack et al. [24] studied a homogeneous flow reactor subject to stochastic Damköhler number variations. They derived the classical "S-curve", that gives the solution for the temperature as a function of the Damköhler number. Aside from the Damköhler number, two additional parameters arise: the non-dimensionalised heat of combustion and the non-dimensionalised activation energy. Small values of both these parameters result in a disappearing of the branching points. Then, no hysteresis occurs and the sharp distinction between reacting and non-reacting disappears. This is achieved by diluting and increasing the temperature of the reactants, in other words, by operating in flameless combustion. This qualitative change can not be expressed using by one parameter, nevertheless this (important) detail will be ignored in the discussion.

furnace gases, and the difference in flow scales between fuel jet and flame zone may be not so large. The velocity of the surrounding air jets typically even exceeds that of the fuel jet [114].

In the DJHC flames, the flow time scale is not small enough to distribute or break the flame structures, as these are observed to be smooth and connected. This contrasts OH-PLIF results in flameless conditions (see e.g. [13], Fig. 2.21) and the notion of flameless combustion as being "volumetric" [17]. Clearly, the quasi-laminar coflow results in much larger Damköhler numbers than those encountered in flameless combustion applications. This raises questions on the applicability of this and similar setups to the study of flameless combustion.

That the coflow stream is quasi-laminar is almost unavoidable in laboratory setups. With typical coflow velocities, dimensions and the kinematic viscosity at elevated temperatures, a global Reynolds number of merely a few thousand is achieved. In the DJHC setup, the Reynolds numbers (based on the tube diameter, a velocity of 5 m/s and a kinematic viscosity of $200 \times 10^{-6}\mathrm{m}^2/\mathrm{s}$) is about 2,000. To generate a turbulent coflow, a higher velocity and/or wider coflow stream would be needed. Furthermore, a mean shear is needed in the coflow to produce turbulent kinetic energy and generate a truly turbulent stream, rather than decaying grid turbulence.

The DJHC flames are thus characterised by a strong external intermittency. Intermittency is known to be relevant whenever a turbulent stream mixes with irrotational surroundings [115]. Modifications of turbulence models based on the intermittency factor, describing which fraction of time the flow is turbulent at a given point, have therefore been introduced [116]. Therefore, despite being different from the common perception of flameless combustion, the intermittent nature could be of interest to certain combustion situations.

5.7 Conclusions

Detailed conditional (i.e., conditional on the presence of flame zones) and conditioned (i.e., considered in locally introduced coordinate systems relative to the flame zones) velocity data obtained with simultaneous PIV and OH-PLIF measurements were shown, for three different flames in the Delft jet-in-hot-coflow burner. These flames differed in jet diameter (and thereby in normalised axial distance) and level of premixedness (and thereby in stoichiometry). Despite these differences, the results were qualitatively similar, and almost identical after normalisation. The main results for the three flames can therefore be discussed as one single case.

The velocity data conditional on flame presence differed strongest from the unconditional data for the radial velocity and the mean and variance of vorticity. The conditional radial velocities are directed more strongly inward, indicating the entrainment and turbulent transport at the jet edge. The values of the conditional mean and variance of vorticity were orders of magnitude smaller than those in the shear layer of the jet. The conditioned

data shows a very steep increase in shear and vorticity, a mere millimetre from what was defined to be the flame edge. This result could be misinterpreted (especially in point measurements) as a "preference" of the flame for regions with low strains, but that would imply an incorrect causality. The correct explanation is that at the low mixture fractions where the OH radical is present the vorticity field originates from the coflow, rather from that of the jet. This view is corroborated by the overlaid seeding- and OH-PLIF images, in Section 5.4.2.

The finding that the OH contours exist in a region with negligible mean vorticity is not new. Kothnur et al. [112] found the same in their conventional non-premixed flame experiment, but saw significant vorticity on the CH contours. It can thus not be concluded that the *entire* reaction zone is laminar in the DJHC flames, but at least a very substantial part, at the lean side.

When modelling these flames numerically, these findings have to be considered. In its lift-off region, the flame is highly intermittent, alternating strongly in mixture fraction (as evidenced by the seeding images, and the OH-PLIF images) and in turbulence structure, between being highly rotational to being nearly irrotational. These effects can only be captured with a RANS model that has a physically sound statistical basis, e.g., a model that solves for the transported joint velocity-scalar-frequency pdf [117], or a model that solves for statistical averages and higher moments conditional on mixture fraction [118].

The emerging picture of the flame structure is in contrast with industrial flameless burners, where the delaying effect of strong turbulent strains is considered to be the key to let mixing occur before combustion. It therefore appears that conclusions on turbulence-chemistry interaction drawn from these and similar laboratory flames cannot be generally projected onto industrial-sized flameless combustion burners, at least not without a careful analysis.

CHAPTER 6

Stabilisation mechanisms of non-premixed, autoigniting flames

6.1 Autoignition and flame propagation

In Chapter 2, it was concluded that the flame propagation speed is insufficient to stabilise the DJHC flames by flame propagation alone. A regular supply of autoignition kernels is thus necessary, while at the same time, flame propagation is responsible for the growth of the initially millimetre-sized kernels. In principle, flame propagation is not a necessary ingredient for flame stabilisation in the presence of autoignition events. The flame could also burn steadily by successive autoignition alone. In this chapter, it is investigated which parameters determine which stabilisation mechanism occurs, i.e., whether flame propagation has an important share in determining the lift-off height or not. Furthermore, the location where autoignition events start to occur in the presence of a radial temperature gradient in the coflow, as a function of jet velocity, is analysed.

6.1.1 Autoignition delay time statistics

For the autoignition time scale, an Arrhenius-like dependence is taken:

$$t_{\text{ign}} = B^{-1} \exp\left[T_a/T_0\right] \ , \tag{6.1}$$

with T_0 a representative temperature.

We will be looking at a situation in which T_0 fluctuates (in time, or space, or both). It is therefore interesting to look at the statistics of t_{ign}, given the statistics of T_0. To shorten notation, the dimensionless temperature $\theta = T_0/T_a$ is introduced. The cumulative density functions (cdf's) of temperature and ignition delay are related simply as

$$P_{t_{\text{ign}}}(t) = 1 - P_\theta(t_{\text{ign}}^{-1}(t)) \ , \tag{6.2}$$

with $t_{\text{ign}}^{-1}(t)$ giving the value of θ corresponding to $t_{\text{ign}} = t$. The two probabilities are complementary because $t_{\text{ign}}(T_0)$ is monotonically decreasing.

If θ is normal, $\theta \sim \mathcal{N}\left(\overline{\theta}, \sigma_\theta^2\right)$, with $\sigma_\theta \ll \overline{\theta}$, then θ^{-1} is also approximately normal, with $\mu = 1/\overline{\theta}, \sigma = \sigma_\theta/\overline{\theta}^2$. Expressed in the original dimensional variables,

$$\sigma = \frac{T_0' \, T_a}{\overline{T_0}^2} \ , \tag{6.3}$$

where the prime after T_0 indicates the rms of its fluctuation. Inspection of Eq. 6.1 learns that the logarithm of $\tilde{t}_{\rm ign} = Bt_{\rm ign}$ is then approximately normal (where the non-dimensional time scale $\tilde{t} = Bt$ is introduced). As a result, the cdf of $\tilde{t}_{\rm ign}$ approximates the cdf of a lognormal distribution:

$$P_{\tilde{t}_{\rm ign}}(\tilde{t}) = \frac{1}{2}{\rm erfc}\left[-\frac{\ln(\tilde{t})-\mu}{\sigma\sqrt{2}}\right] . \tag{6.4}$$

This can be simplified by introducing the non-dimensional time scale $\tau = t/t_{\rm ign;ref}$, with $t_{\rm ign;ref} = t_{\rm ign}(\overline{\theta})$:

$$P_{\rm b;ign}(\tau) = \frac{1}{2}{\rm erfc}\left[-\frac{\ln(\tau)}{\sigma\sqrt{2}}\right] , \tag{6.5}$$

which equals $1/2$ at $\tau = 1$. The probability that autoignition has occurred is now denoted with $P_{\rm b;ign}$. For "typical" values ($T_a = 24,000$, $\overline{T_0} = 1400$, $T_0' = 100$), $\sigma = 1.22$, and the lognormal distribution has a considerable tail ($\tau(P_{\rm b;ign} = 0.9)$ is almost five times larger than $\tau(P_{\rm b;ign} = 0.5)$).

6.1.2 Ignition in a space with a fluctuating initial temperature field

The previous result of the statistics of the autoignition delay time will be applied to a situation in which both autoignition and flame propagation can lead to ignition. The deflagration wave can propagate through the same space (that could be one-, two- or three-dimensional) in which autoignition takes place. The burning state can thus be achieved by two different events:

1. The local occurrence of autoignition
2. The proximity (in time and space) to an autoignition spot

The problem will in this section be considered in the form of an initial value problem, that is, a random initial temperature distribution is imposed onto an undisturbed reactor. Thus, initial temperatures determine the ignition delay time as in Eq. 6.1. The probability that autoignition has occurred locally is equal to the probability that $t > t_{\rm ign}$, as described in Eq. 6.5. This equation suffices to describe the local autoignition process. To study the process of flame propagation, an other viewpoint is adopted: autoignition kernels are assumed to grow only due to flame propagation. In this viewpoint, autoignition is a point event: at a location and time $(\mathbf{z}, t)$, it triggers flame propagation from that point onward. The probability that the burning state is achieved due to this process is called $P_{\rm b;prop}$. The two mechanisms are sketched in Fig. 6.1

An ignition event (i.e., the formation of an ignition kernel, see the solid dots in Fig. 6.1) at $(\mathbf{z}', t')$ is characterised by:

$$\tau|_{(\mathbf{z}',t')} = 1 \ , \ \left.\frac{\partial\tau}{\partial z_i}\right|_{(\mathbf{z}',t')} = 0 \ \text{ and } \ \left.\frac{\partial^2\tau}{\partial {z_i}^2}\right|_{(\mathbf{z}',t')} < 0 \ , \ \ i = 1..N \ . \tag{6.6}$$

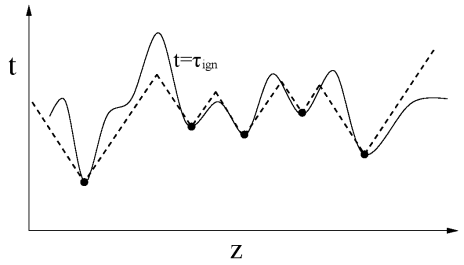

Figure 6.1: The two considered processes that lead to ignition: autoignition (solid line), and flame propagation originating from local autoignition events (dots and dashed lines). At time t all locations z for which t is above either the solid or the dashed line are ignited, according to the respective process.

where N denotes the number of dimensions of $\mathbf{z}$, and τ denotes the local normalised time scale $t/t_{\mathrm{ign}}(\theta(\mathbf{z}))$. The first requirement is obvious, the second and third requirements assure that locally, a new autoignition spot is formed.

We will consider a spatially homogeneous (in a statistical sense) system, with N dimensions. The two requirements for the formation of a new ignition kernel, as a function of the the initial temperature field, are $\theta = \left(\ln\left(\tilde{t}\right)\right)^{-1}$, $\partial_{z_i}\theta = 0$ and $\partial^2_{z_i}\theta < 0$, in all directions. This probability is given by the $N+1$-dimensional joint-pdf of θ, $\partial_{z_i}\theta$ and $\partial^2_{z_i}\theta$. To make further analysis manageable, statistical independence of the variables is assumed:

$$p\left(\theta;\nabla\theta\right) = p\left(\theta\right) \times p\left(\frac{\partial\theta}{\partial z_1}\right) \times \ldots \times p\left(\frac{\partial\theta}{\partial z_N}\right) \ , \tag{6.7}$$

and a similar independence is assumed for higher derivatives. This assumption is not as far-fetched as it may seem, it is for instance satisfied if the random field is generated by filtering white noise, a common procedure to construct spatial random fields [119].

Because of this statistical independence, the number of ignition kernels that are formed in a domain in a small time interval is equal to the product of

- the fraction of the domain where the ignition delay time lies within the time interval, and
- the number density of the event that, simultaneously, the derivatives of θ equal zero and the second derivatives all are negative.

Let us relate the reference length scale to the frequency with which $\partial_{z_i}\theta$ equals its mean value of zero, and satisfies $\partial^2_{z_i}\theta < 0$, for $i = 1 \ldots N$:

$$l_\theta^N \equiv \frac{1}{f(\partial_{z_i}\theta = \mathbf{0}, \partial^2_{z_i}\theta < 0)} \qquad [m^N] \ . \tag{6.8}$$

Note that f denotes the number density of the event between parentheses, not a pdf.

The expected number of locations per domain size where θ is within a certain interval, $\partial_{z_i}\theta$ equals zero and $\partial^2_{z_i}\theta < 0$ is thus:

$$f(\theta^* < \theta \leq \theta^* + d\theta, \partial_{z_i}\theta = 0, \partial^2_{z_i}\theta < 0) = p_\theta(\theta^*)d\theta \, \frac{1}{l_\theta^N} \qquad [m^{-N}] \, . \tag{6.9}$$

We are of course actually interested in the density of such events per time, the pdf of θ will therefore replaced with that of the ignition time, which results in:

$$f(t^* < t_{\text{ign}} \leq t^* + dt, \partial_{z_i}\theta = 0, \partial^2_{z_i}\theta < 0) = p_{t_{\text{ign}}}(t^*)dt \, \frac{1}{l_\theta^N} \qquad [m^{-N}] \, . \tag{6.10}$$

Thus, the number of ignition events per time per domain size (length, area or volume) is

$$f_{\text{ign}} = p_{t_{\text{ign}}}(t^*) \, \frac{1}{l_\theta^N} \qquad [m^{-N}s^{-1}] \, . \tag{6.11}$$

Here, $p_{t_{\text{ign}}}$ is the derivative of Eq. 6.5, i.e. the probability density of autoignition per time time per domain size at time t^*.

The flame probability originating from ignition events and flame propagation with propagation speed v_f alone is given by a convolution back in time. This is somewhat similar to the convolution as discussed in Section 2.3.6, but due to the statistical spatial homogeneity of a simpler form:

$$P_{\text{b;prop}}(t) = 1 - \exp\left[-k_s v_f^N \int f_{\text{ign}}(t')(t-t')^N dt'\right] \, . \tag{6.12}$$

Here, k_s is a shape factor, equal to two in one dimension (linear expansion), π in two dimensions (circular expansion) and $4/3\pi$ in three dimensions (spherical expansion). The flame propagation speed is thus considered to be a separate parameter of the problem. Note that a deterministic flame propagation speed is not necessary for the analysis: the parameter can also be used to quantify the expectation of the flame growth, as discussed in Section 2.3.6.

To enable a more insightful and simpler analysis, this relation can be written as a function of non-dimensional variables. To this end, $t_{\text{prop}} = l_\theta / v_f$ is introduced, which is to be compared with the reference time for autoignition $t_{\text{ign;ref}}$ defined earlier. Note that this reference autoignition time corresponds to that time where half of the domain size has autoignited, due to the assumed normal distribution of θ. Now the flame probability due to flame propagation originating from ignition events can be written down elegantly as:

$$P_{\text{b;prop}}(\text{z}, \tau) = 1 - \exp\left[-k_s \left(\frac{t_{\text{ign;ref}}}{t_{\text{prop}}}\right)^N \int p_{\tau\text{ign}}(\tau')(\tau-\tau')^N d\tau'\right] \, , \tag{6.13}$$

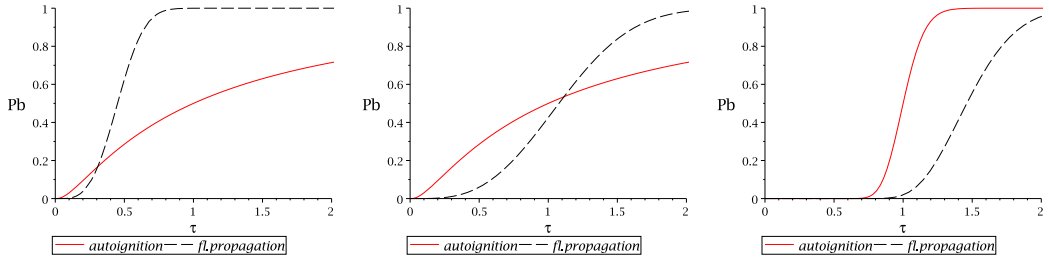

(a) $t_{\text{prop}}/t_{\text{ign;ref}} = 0.25$, $\sigma = 1.22$ (b) $t_{\text{prop}}/t_{\text{ign;ref}} = 1$, $\sigma = 1.22$ (c) $t_{\text{prop}}/t_{\text{ign;ref}} = 1$, $\sigma = 0.122$

Figure 6.2: Flame probability P_b as a function of τ due to successive autoignition (solid lines, according to Eq. 6.5), and due to flame propagation originating from autoignition events (dashed lines, according to Eq. 6.13). The number of dimensions N is two.

with $p_{\tau\text{ign}}$ the pdf of the normalised ignition time $\tau_{\text{ign}} = t_{\text{ign}}/t_{\text{ign;ref}}$. Only if the term between square brackets in Eq. 6.13 is of magnitude one or more, the presence of flame propagation will reduce the ignition time. This requires a reference flame propagation time in the order of one or less, and sufficient variance in ignition delay. The results for three different combinations σ and $t_{\text{prop}}/t_{\text{ign;ref}}$ are shown in Fig. 6.2, for a two-dimensional case. In Fig. 6.2a, the propagation time is short enough such that flame propagation reduces ignition time by more than 50%. In Fig. 6.2b, both mechanisms are of the same importance at $\tau = 1$, whereas in Fig. 6.2c, flame propagation is of no relevance due to the small variance in initial temperature.

It should be realised, that two extreme cases are compared, namely that of no flame propagation at all, and that of growth only due to flame propagation as shown in Fig. 6.1. In the cases shown in Figs. 6.2a and 6.2c, these extremes are encountered. However, in Fig. 6.2b, the real ignition time will be shorter than that according to either of the extremes.

6.1.3 Ignition on a convective interface

The situation that is considered in this section is that of a surface along which flame pockets are convected, on which flow- and/or ignition time scales can possibly change in time and/or space, and which is not necessarily statistically homogeneous. This is considered to be a model for an iso-mixture fraction surface, on which ignitions take place and along which the flame can propagate. The surface is a simple, periodic plane that spans a z_1- and a z_2-coordinate axis. The z_1-axis follows the downstream direction of the jet and is possibly statistically inhomogeneous (for instance, the flow time scale or ignition time scale might vary in this direction). The z_2-axis is assumed to span to infinity. The autoignition criterion is formulated as

$$Da \equiv \frac{t_{\text{flow}}}{t_{\text{ign}}} > 1 \,, \tag{6.14}$$

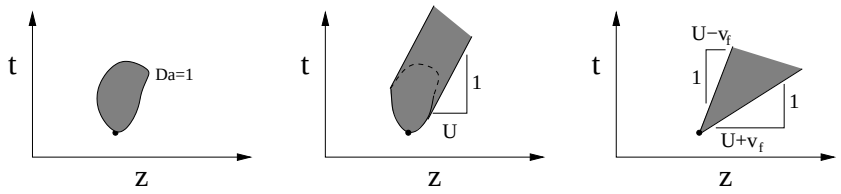

Figure 6.3: The three considered mechanisms, on a one dimensional space. The gray hatching indicates the evolution of flame pockets in time. The left figure shows the autoignition criterion $Da(z,t) \geq 1$ as a criterion for combustion. The flame pocket will disappear where $Da < 1$. The formed flame pocket in the middle figure is however persistent, and does not extinguish. The right figure shows the mechanism of flame propagation originating from local autoignition events, similar to that described in the previous section.

where t_{flow} is some local flow time scale. Da is thus a locally defined variable, in general changing in time and space. Whenever Da exceeds unity, autoignition occurs immediately.

An important difference with the situation of the previous section is that Da can decrease at a given location, whereas τ could not. Depending on the mechanism by which chemical reaction is sustained or propagates, extinction might occur. In the following analysis, three possibilities will be taken into account:

1. Flame pockets are only seen when locally, $Da \geq 1$
2. Flame pockets are created when $Da \geq 1$ and do not extinguish when $Da < 1$
3. Flame pockets are only formed by autoignition events and flame propagation

Mechanisms one and three are similar to the two possibilities investigated in the previous section, but mechanism two is new. It excludes the possibility of extinction of an established flame pocket, and can be compared with the behaviour of an unsteady flamelet without extinction: once ignited, the reaction is sustained locally. Thus, flame pockets are persistent but non-growing.

The three mechanisms are explained in Fig. 6.3. Here, they will be compared for the case of a statistically stationary and homogeneous surface. As a boundary condition, P_b equals zero at $z_1 = 0$.

Mechanism 1 The flame probability of the first mechanism follows easily as:

$$P_{\text{b;ign1}}(z) = P(Da \geq 1) = 1 - P_{Da}(1) \; . \tag{6.15}$$

If we consider that variations in Da are only due to variations in θ (that is, t_{flow} is constant), we can again define a temperature at which ignition occurs: $\theta_{\text{ign}} = (\ln(Bt_{\text{flow}}))^{-1}$. The flame probability can then also be written as

$$P_{\mathrm{b;ign2}} = 1 - P_\theta(\theta_{\mathrm{ign}}) \tag{6.16}$$

If additionally t_{ign} is again lognormal, this probability follows by replacing t by t_{flow} in Eq. 6.5:

$$P_{\mathrm{b;ign1}} = \frac{1}{2}\mathrm{erfc}\left[-\frac{\ln(t_{\mathrm{flow}}/t_{\mathrm{ign;ref}})}{\sigma\sqrt{2}}\right] . \tag{6.17}$$

Mechanism 2 The calculation of the flame probability of the second mechanism requires taking into account the spatial correlation of the Da-field. Specifically, the probability of finding a flame pocket at $(\mathbf{z}, t)$ equals the probability that along a path back through time and z_1, Da at least once exceeded one. This is the complement of the probability that Da never exceeded one:

$$P_{\mathrm{b;ign2}}(z_1', t') = 1 - P(Da(z_1, t' - Uz_1) < 1), \;\; \forall z_1 \left[0 \leq z_1 \leq z_1'\right] . \tag{6.18}$$

We are thus dealing with the statistics of the function $Da\,(\mathbf{z}, t)$ along a line through time and space. Considering that the fluctuations in Da are only due to fluctuations in θ, and that these fluctuations originate from a statistically homogeneous, isotropic surroundings ("coflow") that is being entrained, the temporal fluctuations can be expressed as a function of the spatial fluctuations. This requires the introduction of a relation that describes how fast the temperature field changes on the considered surface. To develop this relation, some simplifications are needed, that are based on experimental observations. Firstly, the temperature in the coflow stream is considered to be frozen, and is thus convected passively toward the jet. The entrainment process is considered to be steady, i.e., the location where a streamline originating from the coflow is entrained does not change with time. Finally, the surface close to stoichiometry (i.e., the region where strong OH-signals are seen) moves in the z_2-direction with a velocity that equals the axial velocity of the coflow U.

Changes experienced by a virtual particle moving on the surface with a velocity U in z_1-direction then originate from gradients in the coflow field in the in-plane direction z_3:

$$\frac{D\theta}{Dt} = U_e \frac{d\theta}{dz_3} , \tag{6.19}$$

where U_e is the entrainment velocity, i.e., the radial velocity which is counted positive when directed toward the centerline. The probability as described in Eq. 6.18 is then equal to the probability of finding a normalised temperature θ exceeding the ignition temperature $\theta_{\mathrm{ign}} = (\ln(Bt_{\mathrm{flow}}))^{-1}$ along a randomly chosen path through the surrounding coflow with length $s = z_1 \frac{U_e}{U}$. Naturally, if this path is very short compared to the lengthscale of the fluctuations of the coflow temperature, this probability equals that of 6.16. If, on the other

hand, this path gets longer, the probability will tend to one. As discussed in Appendix C, the probability of encountering a value for Da exceeding one along such a path is approximated by

$$1 - P_{Da}(1) \exp\left[-s \frac{1 - P_{Da}(1)}{l_\theta}\right] , \tag{6.20}$$

where the constant of proportionality k (see Appendix C) is omitted. The length scale l_θ is an integral length scale. Expressed in the normalised temperature θ, and inserting the equation for s, the flame probability is

$$P_{\mathrm{b;ign2}}(z_1) = 1 - P_\theta(\theta_{\mathrm{ign}}) \exp\left[-\frac{z_1}{l_\theta}\frac{U_e}{U}\left(1 - P_\theta\left(\theta_{\mathrm{ign}}\right)\right)\right] . \tag{6.21}$$

The term between brackets thus acts as a normalised length scale, that determines whether the solution is closer to that of $P_{\mathrm{b;ign1}}$ or to unity.

Mechanism 3 The flame probability due to flame propagation originating from ignition events follows here again from a convolution with the ignition frequency density. This time the convolution kernel is three-dimensional, spanning the z_1 and z_2 directions, and time. The sections through this conical kernel are circular in the (z_1,z_2)-plane, the sections in the (z_1,t)-plane are however not circular nor elliptical. To avoid geometrical complexities, the section of the convolution kernel at a distance Δz_1 is approximated as an ellipse with width $2\Delta z_1 v_f/U$ and height $\Delta z_1 \Phi$:

$$P_{\mathrm{b;prop}}(z_1) = 1 - \exp\left[-\frac{\pi \Phi\, v_f}{2\, U} \int_0^{z_1} (z_1 - z_1')^2\, f_{\mathrm{ign}}(z_1')\, \mathrm{d}z_1'\right] , \tag{6.22}$$

with $\Phi = 1/(U - v_f) - 1/(U + v_f)$, where v_f is the flame propagation speed along the surface. Although Φ is presented as a deterministic parameter, it can also be used to describe a stochastic flame propagation speed (that is, varying flame speeds, or even flame extinction), as discussed in Section 2.3.6. The product of Φv_f is $2(U/v_f - v_f/U)^{-1}$, which can be approximated by $2v_f/U$ for $v_f \ll U$ (the error is $(v_f/U)^2$).

Although the situation is now more complex, the criteria of the formation of a local autoignition event are similar to those formulated previously (see Eq. 6.6):

$$Da|_{(\mathbf{z}',t')} = 1 \ , \quad \left.\frac{\partial Da}{\partial z_i}\right|_{(\mathbf{z}',t')} = 0 \ \text{ and } \ \left.\frac{\partial^2 Da}{\partial {z_i}^2}\right|_{(\mathbf{z}',t')} < 0 \ , \ \ i = 1, 2 . \tag{6.23}$$

Expressed in the non-dimensional temperature θ, these criteria are:

$$\theta|_{(\mathbf{z}',t')} = \theta_{\mathrm{ign}} \ , \quad \left.\frac{\partial \theta}{\partial z_i}\right|_{(\mathbf{z}',t')} = 0 \ \text{ and } \ \left.\frac{\partial^2 \theta}{\partial {z_i}^2}\right|_{(\mathbf{z}',t')} < 0 \ , \ \ i = 1, 2 . \tag{6.24}$$

The frequency of simultaneous occurrence of θ being equal to its mean value $\overline{\theta}$, the first derivatives of θ being zero and the second derivatives being negative is taken to be governed by the integral scales:

$$f(\theta = \overline{\theta}, \partial_{z_i}\theta = 0, \partial^2_{z_i}\theta < 0) = \frac{U_e}{l_\theta^3} \qquad [m^{-2}s^{-1}] \,. \tag{6.25}$$

Because of the absence of correlation between θ and its derivatives,

$$f_{\text{ign}} = \frac{U_e}{l_\theta^3}\frac{p_\theta(\theta_{\text{ign}})}{p_\theta(\overline{\theta})} \,. \tag{6.26}$$

Combining this with Eq. 6.22, integrating and omitting the term $\pi/3$ results in:

$$P_{\text{b;prop}} = 1 - \exp\left[-\frac{p_\theta(\theta_{\text{ign}})}{p_\theta(\overline{\theta})}\frac{\Phi v_f}{2}\frac{Ue}{U}\left(\frac{z}{l_\theta}\right)^3\right] \,. \tag{6.27}$$

Comparison of the three mechanisms The complements of the flame probabilities of the three mechanisms are now compared, with the parameters organised such that they form non-dimensional groups

$$1 - P_{\text{b;ign1}} = P_\theta(\theta_{\text{ign}}) \tag{6.28}$$

$$1 - P_{\text{b;ign2}} = P_\theta(\theta_{\text{ign}}) \exp\left[-\frac{z_1}{l_\theta}\frac{U_e}{U}\left(1 - P_\theta(\theta_{\text{ign}})\right)\right] \tag{6.29}$$

$$1 - P_{\text{b;prop}} = \exp\left[-\left(\frac{z}{l_\theta}\right)^3 \frac{Ue}{U}\frac{\Phi v_f}{2}\frac{p_\theta(\theta_{\text{ign}})}{p_\theta(\overline{\theta})}\right] \tag{6.30}$$

The exponential decay of the complement of $P_{\text{b;prop}}$ goes with z/l_θ cubed, which quickly leads to a dominance of growth due to flame propagation for $z/l_\theta \gg 1$. A second difference is that only the cdf of θ at θ_{ign} matters for mechanisms 1 and 2 (purely autoignition), whereas the flame propagation mechanism, mechanism 3, is dependent for the pdf at θ_{ign}. This is because an autoignition event will only occur when the local value of Da changes from below one to above one. Therefore, the specific value θ_{ign} must be accessed frequently enough by θ.

In Fig. 6.4, some results for different combinations of parameters are shown. In Fig. 6.4a, the flow time scale is larger than the ignition time of the mean temperature, and the fluctuations are small ($\sigma = 0.122$). Therefore, autoignition takes place immediately. In Fig. 6.4c, the probability of $Da > 1$ is very small, but autoignition events are nevertheless frequent due to the larger variance in temperature ($\sigma = 1.22$). Therefore, flame propagation from these local autoignition events is dominant.

Note that the scaling of z/l_θ to the third power in the expression for $P_{\text{b;prop}}$ will not hold for large values of z/l_θ, if the z_2 axis stands for the circumference of a turbulent jet. After a

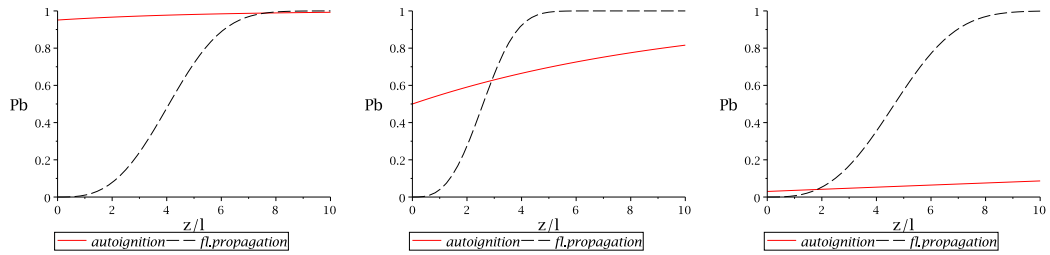

(a) $\frac{t_{\text{flow}}}{t_{\text{ign;ref}}} = 1.5, \sigma = 0.245$ (b) $\frac{t_{\text{flow}}}{t_{\text{ign;ref}}} = 1, \sigma = 1.22$ (c) $\frac{t_{\text{flow}}}{t_{\text{ign;ref}}} = 0.1, \sigma = 1.22$

Figure 6.4: Flame probability P_b as a function of z/l_θ for purely autoignition and flame propagation from ignition events ($P_{\text{b;ign2}}$ and $P_{\text{b;prop}}$, solid and dashed lines, respectively). The flow time scale normalised with the ignition delay time of the mean temperature ($t_{\text{flow}}/t_{\text{ign;ref}}$) and the normalised fluctuation of temperature (σ) are varied. U_e/U and $\frac{v_f}{U}$ are both kept constant at 0.2.

distance of $z \approx \pi r_{\text{jet}} U/v_f$, flame pockets will have grown along the entire circumference, and the scaling will go with z/l_θ to the power of two.

As in the previous section, the combination of mechanisms one and three (or two and three) were not considered due to its mathematical complexity. A combination can be expected to be relevant, when two mechanisms predict an increase in P_b of the same magnitude.

The effect of mean gradients, or variation in t_{flow} were not taken into account, but these possibilities can be analysed qualitatively. The flame probability $P_{\text{b;ign}}$ (both variations) is a direct function of P_θ. A stepwise increase in the temperature, or more generically, a stepwise increase in $P_{Da}(1)$, will therefore directly result in an increase in $P_{\text{b;ign}}$. Furthermore, as an autoignition event requires that the first derivative of Da equals zero, a steep gradient of the mean value of Da, in comparison to the rms of the gradient of the fluctuations of Da, will make the probability of dDa/dz being zero very small. In an extreme case, where Da does not fluctuate at all but at a certain point becomes larger than one, a steady autoignition front will be present and no flame pockets are formed. It can thus be stated that steep increases in Da favour autoignition as flame stabilisation mechanism.

Discussion The Damköhler condition for autoignition (Eq. 6.14) enabled a straightforward analysis of the problem. A more general approach would involve taking into account the gradual build-up and simultaneous depletion of the radicals and temperature (by reaction and diffusion processes), necessary to initiate autoignition. The currently used autoignition criterion sets no minimum limit on the duration of $Da > 1$, which implies that the reactive and diffusive terms are balanced. Diffusion and reaction time scales are thus considered to be much smaller than the time scales of changes in the temperature θ, and of convection through the considered domain. This condition is not necessarily satisfied

in the DJHC flames. In flameless combustion the convection time scale is even expected to be relatively short compared to the time needed for autoignition, possibly leading to a very different regime. The previous analysis is therefore meant as a first exploration of the proposed stabilisation mechanism, and further (perhaps numerical) analysis is absolutely required for a general classification of stabilisation mechanisms under the combined presence of autoignition and flame propagation.

An obvious and important question is what causes the randomness in autoignition events in the DJHC flames. Despite the many different measurements on the flames, an answer can not be given with certainty. The CARS measurements (Chapter 3) indicate considerable temperature fluctuations (rms of approximately 100 K) which should cause a significant scatter in autoignition delay times. The conditional velocity field (Chapter 5) revealed a roughly equal probability of compressive and extensional strain normal to the flame interface. The data does however not reveal whether the presence of ignition kernels is accompanied by low strains. The rather stationary flame contours seen in a laminar fuel jet in the DJHC flames (see Fig. 4.11a) indicate that in the absence of flow time scale fluctuations, the ignition process is not very random on short time scales, despite the temperature fluctuations. This might indicate that the temperature fluctuation length scales are long, at least in axial direction. The randomness caused by the turbulence therefore seems to be at least partially responsible for the randomness in autoignition. The issue might be resolved with knowledge of the mixture fraction field and its gradient, simultaneous with an indicator for ignition events, as could be obtained from OH- or CH2O imaging. The mixture fraction would provide an appropriate quantity for conditioning: by plotting flow-related quantities such as vorticity or strain against mixture fraction, these quantities can be compared for reacted and non-reacted fluid.

In the light of the results in this section, the flame stabilisation mechanism of autoignition events that initiate flame propagation might be of relevance to industrial devices, where the ratio of length scales is large and the fluctuations in Da are expected to be strong. On the other hand, flame propagation might be severely hampered by the large convective velocities and stronger wrinkling of the flame front as compared to the DJHC-flames. Furthermore, the assumption that the chemistry instantly adopts to a local Damköhler number might not apply to flameless combustion situations. Only the application of detailed (laser)-optical techniques on such devices, followed by a rigorous analysis, can provide the answer.

6.2 The effect of a mean temperature gradient in the coflow

In Chapter 2, the statistics of the stabilisation processes were discussed for several flames. The lift-off height was treated as a function of three parameters, namely

- the location where autoignitions first occur downstream, $z_{\mathrm{b;min}}$,
- the autoignition frequency and the

- flame transfer probability.

For the parameter $z_{\mathrm{b;min}}$, a decreasing trend as a function of the jet exit velocity was observed. This result is in contrast with the common observation that the lift-off height increases with increasing jet velocity, for instance in the Cabra burner [37]. The latter trend has a plausible explanation. Considering the inhibiting influence of turbulent strains on the autoignition process [45], the greater strains associated with a larger jet velocity will postpone autoignition. Furthermore, the downstream transport of fluid parcels while undergoing autoignition is larger with increasing jet velocity. The opposite trend found in the DJHC flames was investigated in Chapter 3. The explanation for the decrease of $z_{\mathrm{b;min}}$ was that the larger entrainment rate at larger jet velocities transports the hotter coflow from larger radii inward faster. Thus, the positive radial temperature gradient at z=0 is responsible. Apparently, the decrease in flow time scale (that is, the inverse of the magnitude of the characteristic turbulent strain magnitude) is not very relevant. These two seemingly incompatible results will be brought together in this section.

Let the onset of autoignition events require that the difference between the reference time scale for autoignition and the reference flow time scale (which could be the inverse of a typical scalar dissipation rate) becomes smaller than a certain limit value. In that case, the probability that simultaneously, the autoignition time is small enough (temperature large enough) and the flow time scale is large enough to initiate autoignition becomes significant. The probability of the rare event of autoignition (in the experimental study in Chapter 2, $z_{\mathrm{b;min}}$ corresponded to a flame probability P_{b2} of 0.25%) is thus assumed to be governed by the distance between the reference time scales for autoignition and flow processes. The difference between the two time scales ($t_{\mathrm{flow;ref}} - t_{\mathrm{ign;ref}}$) is considered to be monotonically increasing with z, which practically implies a positive or zero radial temperature gradient of the entrained coflow with z, since the integral time scale of an ideal turbulent jet and thus $t_{\mathrm{flow;ref}}$ increases with axial distance.

The corresponding axial height where, occasionally, mixtures are formed that will after some time autoignite, is thus given by:

$$z^0_{\mathrm{ign}} = z\left(t_{\mathrm{flow;ref}} - t_{\mathrm{ign;ref}} = t'_{\mathrm{crit}}\right) \ , \tag{6.31}$$

with t'_{crit} depending on the strength of the fluctuations in the reference flow and ignition time scales $t_{\mathrm{flow;ref}}(z)$ and $t_{\mathrm{ign;ref}}(z)$. t'_{crit} is assumed to be no function of z or U_{jet}. To shorten notation, the extension ";ref" will be omitted in the following.

The height at which autoignition events are first observed occasionally, is

$$z_{\mathrm{ign}} = z^0_{\mathrm{ign}} + U_{co}\, t_{\mathrm{ign}}(z^0_{\mathrm{ign}}) \ . \tag{6.32}$$

The additional distance $U_{co}\, t_{\mathrm{ign}}$ is due to the convective transport during the autoignition process. The difference between the reference ignition time and the actual ignition time (presumably somewhere in between the reference ignition and flow time scales) is ignored for the sake of simplicity. With this formulation, the analysis can be limited to that of the

changes in the reference time scales. The ignition time scale is supposed to be a function of the coflow temperature alone, which is convected passively.

The validity of the assumption that the temperature is convected passively along streamlines in the jet was validated numerically in [120]. Within the coflow region, temperatures were shown to collapse on a single curve when plotted against the stream function Ψ. Thus, the ignition time scale is a function of the streamline coordinate Ψ, see also Section 3.7, Fig. 3.16. The dependencies of both reference time scales are:

$$t_{\text{ign}} = f(\Psi(U_{\text{jet}}, z)) \qquad \text{and} \qquad t_{\text{flow}} = f(U_{\text{jet}}, z)\ , \tag{6.33}$$

such that

$$\left.\frac{\partial t_{\text{ign}}}{\partial U_{\text{jet}}}\right|_{z^0_{\text{ign}}} = \left.\frac{dt_{\text{ign}}}{d\Psi}\frac{\partial \Psi}{\partial U_{\text{jet}}}\right|_{z^0_{\text{ign}}} \quad \text{and} \quad \left.\frac{\partial t_{\text{ign}}}{\partial z}\right|_{z^0_{\text{ign}}} = \left.\frac{dt_{\text{ign}}}{d\Psi}\frac{\partial \Psi}{\partial z}\right|_{z^0_{\text{ign}}}\ . \tag{6.34}$$

The first term after both equals signs is, under the assumptions, a boundary condition imposed by the coflow. The other two terms are properties of the entrainment process. Taking the expression for the totally entrained mass into a turbulent jet as [121]:

$$\dot{M}_e(z) = K_1\ z\sqrt{\rho_{\text{co}}\ \rho_{\text{jet;0}}}\ U_{\text{jet}}\ D_0\ , \tag{6.35}$$

we can deduce that

$$\frac{\partial \Psi}{\partial U_{\text{jet}}} \propto z\ D_0 \qquad \text{and} \qquad \frac{\partial \Psi}{\partial z} \propto U_{\text{jet}} D_0\ . \tag{6.36}$$

At z^0_{ign}, which will generally change when U_{jet} is increased, the changes in autoignition- and flow time scales are equal because of the ignition criterion (Eq. 6.31). Therefore,

$$\begin{aligned} dt_{\text{ign}}\left(z^0_{\text{ign}}\right) &= \left.\frac{\partial t_{\text{flow}}}{\partial U_{\text{jet}}}\right|_{z^0_{\text{ign}}} dU_{\text{jet}} + \left.\frac{\partial t_{\text{flow}}}{\partial z}\right|_{z^0_{\text{ign}}} dz^0_{\text{ign}} \\ &= \left.\frac{\partial t_{\text{ign}}}{\partial U_{\text{jet}}}\right|_{z^0_{\text{ign}}} dU_{\text{jet}} + \left.\frac{\partial t_{\text{ign}}}{\partial z}\right|_{z^0_{\text{ign}}} dz^0_{\text{ign}} \\ &= dt_{\text{flow}}\left(z^0_{\text{ign}}\right)\ . \end{aligned} \tag{6.37}$$

This can be rearranged to yield an expression for the change in z^0_{ign}:

$$dz^0_{\text{ign}} = dU_{\text{jet}}\ \left.\frac{\frac{\partial}{\partial U_{\text{jet}}}\left(t_{\text{ign}} - t_{\text{flow}}\right)}{\frac{\partial}{\partial z}\left(t_{\text{flow}} - t_{\text{ign}}\right)}\right|_{z^0_{\text{ign}}}\ . \tag{6.38}$$

Some interesting conclusions can be drawn from Eqs. 6.37 and 6.38. The denominator in Eq. 6.38 is positive (an increase of t_{ign} with z, which would imply a negative radial

temperature gradient in the coflow, is not considered). The numerator therefore determines whether $z^0_{\rm ign}$ decreases or increases with $U_{\rm jet}$. A decrease in $z^0_{\rm ign}$ is thus a sign that

$$\left.\frac{\partial \Psi}{\partial U_{\rm jet}} \frac{dt_{\rm ign}}{d\Psi}\right|_{z^0_{\rm ign}} < \left.\frac{\partial t_{\rm flow}}{\partial U_{\rm jet}}\right|_{z^0_{\rm ign}} . \tag{6.39}$$

This implies a strong sensitivity of the total entrainment to the jet velocity (i.e., a large z) and/or a large positive radial temperature gradient in the coflow. Furthermore, from Eq. 6.37 it can be concluded that the ignition time scale at $z^0_{\rm ign}$ decreases when $U_{\rm jet}$ is raised. This can be understood from the following reasoning. The first term after the equals sign is negative in both cases (both $t_{\rm flow}$ and $t_{\rm ign}$ decrease at a given z with increasing $U_{\rm jet}$). The partial derivative of $t_{\rm flow}$ with respect to z is positive, whereas that of $t_{\rm ign}$ is negative. The change in $z^0_{\rm ign}$ can in principle be positive or negative. One of the expressions (the one based on $t_{\rm flow}$ or the one on $t_{\rm ign}$) must be negative, and because of the equals sign, so are both. Since the ignition time decreases with Ψ, the total amount of entrained coflow at the point of ignition will increase with the jet velocity, also in the presence of a positive radial temperature gradient.

The change in the observed point of ignition is

$$dz_{\rm ign} = dz^0_{\rm ign} + U_0 \, dt_{\rm ign}(z^0_{\rm ign}) . \tag{6.40}$$

Even in a coflow with a constant positive radial temperature gradient at $z = 0$, the continuous decrease in $|dt_{\rm ign}| / d\Psi$ at $z^0_{\rm ign}$ (since the magnitude of the derivative of the ignition delay time with respect to temperature gets progressively smaller with temperature), will at some point lead to an increase in $z_{\rm ign}$ with $U_{\rm jet}$.

Finally, consider the change in the location $z_{\rm ign}$ as a result of a small change in the autoignition delay time:

$$dz_{\rm ign} = dt_{\rm ign}(z^0_{\rm ign}) \left[U_0 + \left(\frac{\partial}{\partial z} \left(t_{\rm flow} - t_{\rm ign} \right) \Big|_{z^0_{\rm ign}} \right)^{-1} \right] . \tag{6.41}$$

The presence of a negative gradient of the ignition time with respect to Ψ thus makes a flame less sensitive to changes in mean coflow temperature.

To summarise, the most important conclusions of the previous analysis are that:

- If the gradient of the temperature of the entrained coflow in axial direction is large enough, the accompanying negative gradient of the ignition time will result in a negative dependence of $z_{\rm b;min}$ on $U_{\rm jet}$
- If the jet velocity is raised far enough, the reduction in the flow time scale will at a certain point become dominant, and then lead to an increase of the location where autoignition events start to occur

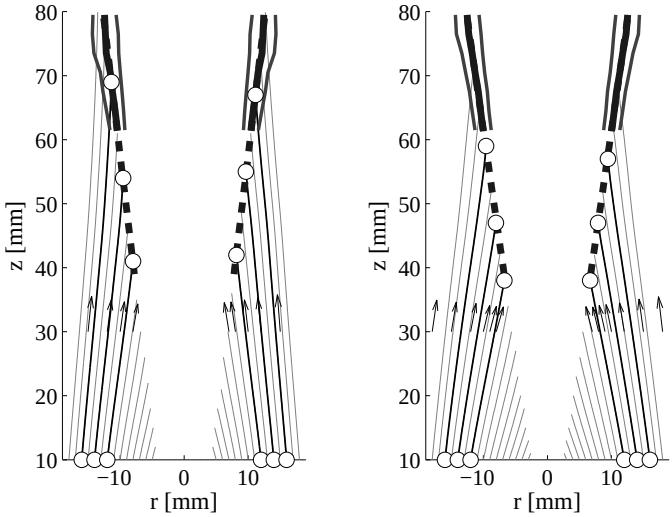

Figure 6.5: Streamlines in the coflow of the DJHC-I flame, $\mathrm{Re_{jet}}$=4100 (left) and $\mathrm{Re_{jet}}$=8800 (right), calculated as an average from 5400 PIV velocity fields. The PIV measurements were made at 500 Hz, with a time interval between the laser pulses of 200 μs. Vectors from LDA measurements are added to show the agreement between the LDA and the PIV measurements. The circles at z=10 mm indicate the origins of the highlighted streamlines, which are $(|r|, z)$=(12,10) mm, $(|r|, z)$=(14,10) mm and $(|r|, z)$=(16,10) mm. Extrapolation to z=3 mm leads for both cases to radial positions of 13 mm, 15 mm and 17 mm, rounded to the nearest millimetre. The thick lines indicate the average position of the jet-coflow interface, as explained in Section 5.5.2.

- A positive radial temperature gradient in the coflow makes a flame less sensitive to changes in the overall temperature

6.2.1 Evaluation of lift-off height trends

The observed dependence of $z_{\mathrm{b;min}}$ (the location where ignition events first occur) with the jet velocity, see Figs. 2.12 and 3.6, are analysed with the previous results in mind. From Fig. 3.6, it is seen that the decrease in $z_{\mathrm{b;min}}$ due to an increase in jet fuel mass flux from 16.1 to 30.0 nl/min is much stronger in the DJHC-I flame (where it goes from z=50 mm to z=42 mm) than in the DJHC-X flame (from z=70 mm to z=69 mm).

From Fig. 6.5, the origin of the coflow streamline that is entrained at different values of z can be derived. In the DJHC-I flame, the entrained coflow at $z_{\mathrm{b;min}}$ for both jet fuel mass fluxes (16.1 to 30.0 nl/min) comes from (z, r)=(3,14) mm. At this point the coflow has a temperature of approximately 1460 K, and has thus not yet reached its maximum temperature of 1540 K at approximately (z, r)=(3,20) mm (reported coflow temperatures are averages from the values for positive and negative r).

In the DJHC-X case with a mass flux in the jet of 16.1 nl/min the streamline that gets entrained at $z_{\mathrm{b;ign}}$ originates from (z, r)=(3,17) mm. At a jet fuel mass flux of 30.0 nl/min it originates from (z, r)=(3,19) mm. The temperatures of the coflow on these locations are 1370 K, and 1395 K, respectively. The latter temperature represents the maximum coflow temperature of the DJHC-X case.

Accounting for the convective displacement between the time of the formation of an self-ignitable mixture and the time of its actual autoignition, the radii will become somewhat smaller. An estimate will require the judicious choice of an appropriate temperature, and calculating an ignition delay time based on that temperature. This will not be undertaken here. However, it is very plausible that the coflow fluid that leads to the first autoignition events originates from larger radii in the DJHC-X case than in the DJHC-I case. Since the temperature gradient flattens at these larger radii, the decrease in autoignition time with Ψ (see also Eq. 6.39) is not as strong in the DJHC-X case as in the DJHC-I case. This result connects very well to the finding in the previous section. The weaker dependence of the ignition time with Ψ makes that the impact of the decreasing flow time scale is stronger, resulting in virtual no decrease in $z_{\mathrm{b;min}}$ in the DJHC-X case.

This is seen even more clearly in the DJHC-V flame with fuel-II, for which $z_{\mathrm{b;min}}$ starts to rise from a jet Reynolds number of 5000 (see Fig. 2.12). At this Reynolds number, the streamline of the coflow that gets entrained at z=90 mm is estimated to originate from (z, r)=(3,20) mm. Here, the coflow temperature reaches its peak, to slowly decrease with increasing Ψ. The decrease in the ignition frequency (see Section 2.3.7, Fig. 2.17) in this case can thus be attributed to a slight decrease in temperature of the entrained coflow. The flame was not studied at a higher jet fuel mass flux because the flame became unstable at that point, i.e., did not ignite regularly anymore. A value for $z_{\mathrm{b;min}}$ at a higher jet Reynolds number is thus not available, but is known to strongly increase beyond this point.

In the previous considerations, heat losses in the coflow due to thermal radiation were not considered. Because the coflow is small and thus optically thin, radiation does not redistribute the heat within the coflow, but acts as a sink term throughout the coflow. From numerical calculations [120], it is estimated that the maximum reduction in temperature in the coflow region at z=90 mm due to radiation is 60 K. An additional heat loss due to radiation contributes to an increase of t_{ign} with Ψ, making the flame more sensitive for blow-off. Thus, thermal radiation is likely partially responsible for the radical increase in $z_{\mathrm{b;min}}$ that was observed in the DJHC-V flame with fuel-I.

CHAPTER 7

Conclusions and recommendations

7.1 Conclusions

Several experimental studies on the Delft jet-in-hot-coflow (DJHC) burner were described in this dissertation, along with a theoretical study to put the results regarding the flame stabilisation mechanism in a broader perspective. The DJHC setup itself is rather academic – that is to say, it is not a practical device or a model thereof – but is nevertheless aimed at gaining understanding of practical, industrial applications. The analysis therefore involves not just consideration of the studied flames, but also of the implication of the findings for industrial combustion devices. The following issues will therefore be addressed here:

- What are the most important characteristics of the studied flames?
- Which generally applicable insights were obtained?
- In how far are these (and similar) experiments suited for model validation?

The following conclusions are grouped into three sections, that aim to answer these questions one by one.

7.1.1 Characteristics of the studied flames

The stabilisation mechanism observed in all of the studied DJHC flames is the random creation of autoignition kernels, and their subsequent growth to larger flame pockets that coalesce to form a persistent flame. The sensitivity of the lift-off height (which was determined from many individual images, instead of from one averaged image) to the composition of the jet fuel is much larger than that of conventional lifted flames: the addition of 5% of ethane to a methane-nitrogen mixture resulted in a decrease in lift-off height of fifteen millimetres or more, whereas this difference was a mere five millimetres or less in a conventional lifted flame. This strong influence of the fuel composition is due to the sensitivity of autoignition processes in natural gas mixtures to the presence of higher alkanes.

A rather uncommon lift-off trend was found in all DJHC-flames: an increase in jet velocity was accompanied by a lowering of the location where autoignition events first take place. This peculiar phenomenon is due to the positive radial temperature gradient in the coflow. At higher jet velocities, the hotter coflow from larger radii gets entrained faster, thus leading to a shift in upstream direction of autoignition events.

The results from transient experiments, in which the fuel jet was impulsively started, were very much in line with the finding that the rate of entrainment is crucial to the lift-off

height. The large-scale temperature gradient in the coflow imposes a substantial additional ignition delay time on the flames. By the injection of virtual Lagrangian particles in the velocity field of the coflow obtained with the time-resolved PIV-system, the development of the streaklines and streamlines was visualised. The ignition delay times were in agreement with the observed adjustment of the streaklines in the coflow. The ignition delay in the DJHC flames is thus governed by an integral time scale, needed to transport hot coflow fluid inward to the jet, several times larger than the time scale needed for the jet flow to develop into its steady turbulent state.

The last experimental study was aimed at probing the velocity field at the location where reactions start to take place. The conditioned flow field data revealed a sharp difference between the velocity field on the OH-structures and the velocity field somewhat further into the jet. The fuel-rich side of the edges of the OH-contours coincides with a very steep increase of vorticity levels, both in their mean and their variance. Within two millimetres, or 0.2 times the jet radius r_{jet}, the vorticity levels rise from near zero toward those typically found in the turbulent jet. The OH-contours themselves however lie within the quasi-laminar coflow. The normal strain on the flame interface is on average very low due to the orientation of the principal strain axes. The 10^{th} percentile of the normal strain on the fuel-rich side of the OH-contours has a magnitude of around -0.5 $U_{\mathrm{jet}} r_{\mathrm{jet}}^{-1}$. The strength of these strains does not drop as steeply as that of the vorticity at the flame edge.

Based on the high-speed flame luminescence recordings discussed earlier, it was concluded that the effective flame propagation speed was insufficient to keep up with the mean convection. A single ignition event (spark ignition, autoignition) does therefore not suffice to keep the flame burning, a continuous supply of ignition events is needed instead. The stabilisation can in principle be realised by autoignition alone, or be strongly enhanced in the presence of additional flame propagation. To find out what parameters determine how important flame propagation is to the stabilisation process, the statistics of autoignition and flame propagation processes were studied theoretically. This was done with a fluctuating temperature field as a starting point to generate randomness in the autoignition process. Autoignition was assumed to take place on the basis of a simple Damköhler criterion. Whenever the fluctuations in the local Damköhler number (which determines whether autoignition takes place or not) are strong, and have short length scales, flame propagation will become the dominant mechanism. Pure autoignition is only relevant in the absence of fluctuations, or in the presence of a strong mean gradient in the Damköhler number, such as would be produced by a steep increase in the flow time scale, or a steep decrease in the autoignition time scale.

Finally, the decreasing trend of the location where autoignition processes start to take place as a function of the jet velocity was analysed, using straightforward arguments. In general, an autoigniting flame in a coflow with a positive radial temperature gradient will have initially a decrease in location of first autoignition due to enhanced entrainment. At a certain point, the flow time scale will become dominant, leading to an increase in lift-off heights. This is in line with the experimental findings of Chapter 2. The effect of

a decreasing flow time scale on the ignition process is seen in the DJHC flames at jet Reynolds numbers exceeding roughly 5,000, as from that point on the decreasing trend stagnates, or even reverses (flame DJHC-V, with fuel-I). In this case, the increase is further enhanced by the quasi-parabolic profile of coflow temperature in radial direction, and likely by heat losses due to radiation.

7.1.2 Insights of general interest

Some phenomena have been observed that are expected to have more general relevance. It is seen that autoignition-stabilised flames are much more sensitive to fuel composition, in particular to the presence of higher alkanes. Also, the consequence of large scale inhomogeneities to the transient ignition behaviour, as discussed in Section 7.1.1, is potentially of interest to combustion applications where regenerators are used which introduce unsteadiness into the system.

The most interesting finding –albeit a more academic one– is perhaps the cooperation between autoignition and flame propagation as a stabilisation mechanism. To quantify the stabilisation process, the variable P_b was introduced, which gives the fraction of time that combustion takes place as a function of height. The value of P_b, which lies necessarily between zero and one, was expressed as the result of a convolution of two quantities: the autoignition density (number of ignition events per time per length or surface) and the flame transfer probability, which gives the probability that an ignition event at a certain location results in a chemically reactive state at another location, at some later point in time. This provides a new description of flame stabilisation, not based on a local equilibrium between chemistry and flow time scales.

In the statistical analysis of Chapter 6, it was concluded that this mechanism will be important, when there are large fluctuations on in the flow and/or autoignition time scales, when these fluctuations occur on smaller length scales and when there is no strong gradient in the mean flow or autoignition time scales. These requirements might be fulfilled in a large-scale setup too. The analysis was however subject to several assumptions, among which the assumption that the chemistry and diffusion processes are happening on much shorter time scales than the convective transport over the integral length scale. In how far the results hold when these assumptions are relaxed, can only be judged from a more detailed analysis. Furthermore, to find out whether the observed stabilisation mechanism also applies to industrial combustion devices would have to be clarified with (laser-)optical measurements.

7.1.3 A reflection on laboratory-scale flameless combustion setups for model validation

Research on laboratory-scale combustion setups is carried out to provide data against which numerical models are validated. Ultimately, these models have to be capable of predicting the performance of large scale industrial combustion systems. One of the reasons for

doing the model validation on laboratory setups instead of directly on industrial combustion systems is that it is very difficult, if at all possible, to do detailed measurements on such devices. It is thus assumed that improved model performance on the one setup implies improved model performance for the other setup. For this assumption to be true, two requirements have to be met.

Firstly, the model has to capture the physics of the laboratory setup. Typically, single-point measurements of quantities such as temperature, velocity etc. form the benchmark for model performance. However, with the limited data that is typically available for validation, and the parameters that can be adjusted freely (or boundary conditions, also due to lack of data), agreement between model and experiment does not necessarily mean that the model is well-suited for the problem at hand. Moreover, the predicate "good agreement" is not subject to any quality standards.

Secondly, the laboratory setup has to be representative in some way for the industrial device: both setups need to operate in a similar combustion regime. Although this speaks for itself, it is not easily guaranteed. As was discovered in the detailed measurements discussed in Chapter 5, the combustion characteristics of the DJHC flames do not comply with those of flameless combustion. One cause for the difference is that the vorticity levels at the flame structures are very low, corresponding with those in the coflow stream, rather than those in the jet. The flame structures are therefore hardly disturbed by the turbulence. In fact, similar laboratory setups might suffer to a certain extent from the same effect, since a fully turbulent coflow stream is difficult to achieve due to the high kinematic viscosity of reaction products at elevated temperatures.

This peculiarity does not make these flames any less interesting from an academic point of view. It does however introduce serious pitfalls for researchers. It is questionable whether a model that is optimised for a laboratory setup will for that reason perform better in predicting an industrial facility. Even worse, if an unsuited model is used for this optimisation, the entire exercise is of little academic or practical value. In relation to the DJHC flames, a physically correct model has to account for the strong intermittency of the velocity- and scalar field, and admit the possibility that mixtures near stoichiometry are in the burnt state only occasionally.

Concluding, the success of model validation depends critically on the correct identification of model performance and on the representativeness of the experimental setup. The latter requirement is not necessarily fulfilled in laboratory burners. Therefore, general statements regarding (the modelling of) flameless combustion based on such setups should be exercised with utmost care.

7.2 Recommendations

In the previous discussion, a gap between the aim of the research and reality was pointed out. Numerical models are validated against experiments that are possibly not fully representative, or against experiments that are representative, but lack detailed data to critically

assess model performance. An obvious recommendation is thus that more detailed experiments be directed toward more realistic setups. This could be approached from two sides.

Firstly, when designing a laboratory sized flameless combustion experiment, special attention has to be given to the flow characteristics of the coflowing oxidiser stream, since this stream is crucial for reaching the low Damköhler numbers associated with flameless combustion. This necessitates generating higher Reynolds numbers in the coflow, and possibly introducing a mean shear to feed the turbulence. From a practical point of view, it might be more efficient to develop a closed combustion chamber with as much optical access as possible. Internal recirculation would make it possible to reach high velocities and thus Reynolds numbers, without paying the penalty of excessive energy demands and heat loads to the laboratory. This would also eliminate the problem of entrainment of cold laboratory air.

Secondly, efforts could be made to push the experimental work on industrial-sized setups beyond the level of probe measurements, towards laser-optical temperature, species and velocity measurements, where possible two-dimensional and time-resolved. An especially interesting option in this respect are semi-industrial-sized combustion devices, such as the MEEC furnace at Delft University of Technology [122]. Although performing (laser-)optical measurements in such a setup is still challenging, knowledge of the flow- and combustion processes inside such a furnace would give specific direction to the research on smaller setups. Specifically, it would be very interesting to see whether a similar mechanism of flame stabilisation is found as in the DJHC flames, despite the differences in combustion regimes.

Another problem signalled in the previous section, is that model performance is perhaps not always evaluated appropriately. Eventually, the ability to reproduce mean quantities constitutes the benchmark for numerical models. However, due to advances in laser technology and (high-speed) imaging, experimental results comprise more than just data sets of mean single-point quantities. This opens up possibilities for a more critical model assessment, paying attention to trends and typical characteristics. For the DJHC flames, these could for instance be the different lift-off trends for different coflow temperatures or the conditional velocity statistics. Furthermore, it would be very interesting to see whether the process of ignition kernel formation and flame propagation can be reproduced, and what different regimes can be identified in the context of the analysis of Chapter 6.

Although many different measurement techniques were applied to probe the DJHC flames, there are some open questions. In particular, the local conditions that favour the autoignition process are yet unclear. Some more information would be especially helpful in addressing this issue. Imaging of the CH- or the CH_2O radical (preferably simultaneously with PIV) would provide more evidence as to whether the flame really only experiences a quasi-laminar flow field, or that the turbulent strains have a large impact on the development of radical species on the rich side of the flame. Two-dimensional Rayleigh

temperature imaging of the coflow field would also be helpful. Although clearly not a replacement for CARS measurements because of CARS' superior accuracy, the spatial information from Rayleigh temperature images might shed some light on the spatial structure of the temperature field, important information considering the sensitivity of autoignition processes to temperature. Finally, mixture fraction imaging would be ideal to determine which factors determine successful autoignition, in particular when performed simultaneously with a technique such as PIV. Accurate mixture fraction imaging is however still a challenging undertaking in reacting flows.

To clear up issues such as the one discussed in the previous paragraph, it would also be helpful to compare results from experimental setups that have different characteristics. For instance, the possibility that only temperature fluctuations are responsible for the randomness in autoignition events could be ruled out if a similar behaviour is observed in a similar burner with a coflow that has very small temperature fluctuations. Combustion experiments located at different laboratories can however in general not be compared fairly, because certain measurement techniques are only available to certain laboratories. Furthermore, measurement data can be processed and presented in many different ways, depending on the creativity or preference of the researcher. To resolve this, one would have to pick a certain aspect to be investigated with a certain measurement technique, and perform this consistently in several setups. This could deliver useful insights into combustion physics and yield guidelines for the development of future combustion experiments.

APPENDIX A

Corrected jet Reynolds numbers

In Chapter 2, jet Reynolds numbers were given based on an estimated, constant jet temperature of 450 K and a resulting kinematic viscosity of ν=1.60 $\times$ 10^{-5}m^{2}s^{-1}. The reference velocity of the cases was based on the measured centerline velocity of one case (not the bulk velocity, as erroneously mentioned in the published article), and linearly scaled with the jet mass flux. In Chapter 3, the jet Reynolds numbers were given with the real temperature of the jet accounted for. Using the centerline- instead of the bulk velocity leads to higher jet Reynolds numbers, which is compensated by the generally overestimated jet temperature, such that the corrected jet Reynolds numbers are not too different.

The following table compares the uncorrected jet Reynolds numbers of Chapter 2 based on those determined in Chapter 3, rounded to the nearest hundred. The corrected Reynolds numbers are interpolated and extrapolated from those determined for the DJHC-I case, for mass flows of 10.7, 16.1 and 30.0 nl/min. Note that the jet Reynolds numbers of the DJHC-V case are somewhat higher for an identical jet mass flux.

The corrected Reynolds numbers have an accuracy estimated at 11%, due to limited accuracy of the mass flow meter (0.3 nl/min, or 3% in the worst case), and due to limited accuracy of the calculated volume flux from the LDA data (estimated at 2.5%, mainly due to limited accuracy of the traversing rig of 0.1 mm). The temperature of the jet is determined through the density, which follows from the ratio of the mass flow and the volume flow determined by integrating the LDA measurements. The error in the temperature also propagates to that in the kinematic viscosity, hence the relatively large inaccuracy. The corrections in jet Reynolds numbers lie thus for a large part within the limits of the accuracy.

Mass flow fuel [nl/min]	Re_{jet} (Chapter 2) [-]	Re_{jet}, corrected [-]
10.7	3000	2500
14.0	4000	3500
16.1	4500	4100
17.5	5000	4600
21.5	6000	5800
25.0	7000	7200
33.5	9000	10,000

Table A.1: Jet Reynolds numbers as reported in Chapter 2, and as corrected for the actual jet temperature.

APPENDIX B

Density weighted nature of transit-time corrected LDA data

Several sources of statistical biasing in LDA data have been recognised, most notably those related to the velocity itself [123]. In flows with varying density, another bias will arise. Intuitively, one can see that a fluid parcel with low fluid density will have a low seeding density and thus a lower probability of detection by the LDA system. Therefore, one might expect the velocity statistics to be affected by these density fluctuations. Goss et al. [124] showed that in their combined CARS/LDA setup, the temperature pdf's, conditional on the presence of a simultaneous LDA measurement (presence of a seeding particle), were very similar to density weighted CARS measurements. In [125], combined LDA and CARS measurements were carried out to investigate velocity-temperature correlations, using the LDA measurements to compute Favre averaged quantities. Nevertheless, not much attention has been given in literature how LDA data in a variable density environment should be interpreted.

The bias in LDA measurements occurs because the data rate $\dot{n}$ (expected number of seeding particles passing through the measurement volume per time) is a function of the value of the instantaneous velocity vector $\underline{U}$, and possibly of other properties such as the density ρ. The joint pdf of the measured velocity vector, $f_{\underline{U};LDA}$ is a function of the original pdf of velocity and the conditional data rate:

$$f_{\underline{U};LDA} = f_{\underline{U}} \frac{\langle \dot{n} \,|\underline{V}\rangle}{\langle \dot{n} \rangle} \tag{B.1}$$

with the averaging operator defined as:

$$\langle \cdot \rangle = \int_{\psi} \int_{\underline{V}} \cdot \, f_{\underline{U}\rho} \, d\underline{V} \, d\psi \; . \tag{B.2}$$

V and ψ form the sample space of the variables U and ρ, respectively. The instantaneous data rate is equal to

$$\dot{n} = \rho c_m \dot{V} \; , \tag{B.3}$$

with $\dot{V}$ the volume flux and c_m the seeding density, $[-/\mathrm{kg}]$ [126]. To eliminate the bias, some kind of correction is necessary. This is realised in practice by applying an appropriate

weighting factor w to the data points. To demonstrate the connection between application of weighting factors on data points and the scaling of the pdf, consider the variable U that has a pdf f_U and is weighted with weight factors w to yield the weighted pdf $f_{U;w}$:

$$\begin{aligned} f_{U;w}(V_k) &= \lim_{N\to\infty}\lim_{\Delta u\downarrow 0}\sum_{m=1}^{M} w_{m,k}\left(\Delta u\ \sum_{}^{N} w_{m,k}\right)^{-1} \\ &= f_U(V_k)\frac{\langle w\,|V_k\rangle}{\langle w\rangle} \end{aligned} \tag{B.4}$$

Here, N is the total number of data points, and M the number of datapoints between $V_k - \frac{1}{2}\Delta u$ and $V_k + \frac{1}{2}\Delta u$. Therefore, if the conditional expectation of the weight factor is inversely proportional to the conditional data rate $\langle \dot{n}\,|\underline{V}\rangle$, application of this weight factor on Eq. B.1 will result in unbiased statistics, since the measured pdf after correction is:

$$f_{\underline{U};LDA^C} = f_{\underline{U}}\,\frac{\langle \dot{n}\,|\underline{V}\rangle\langle w\,|\underline{V}\rangle}{\langle \dot{n}w\rangle} \tag{B.5}$$

Hoesel and Rodi [126] found that, in a constant density flow, the transit time satisfies this criterion. The transit time is a random variable for a given value of $\underline{V}$ (seeding particles pass the measurement volume at arbitrary locations), with expectation :

$$\langle tr\,|\underline{V}\rangle = \frac{V_p}{\dot{V}(\underline{V})} = \frac{V_p\rho c_m}{\dot{n}(\underline{V})} \propto \frac{\rho}{\dot{n}(\underline{V})}\,, \tag{B.6}$$

with V_p the probe volume (which is independent of the flow direction, see the Appendix in [126] for a discussion). The LDA data reported in this study has also been transit-time weighted to avoid the velocity bias. In absence of density fluctuations, unbiased estimates for mean velocities and (co)variances can now be obtained by weighting each measurement with its individual transit time tr_i.

When density fluctuations do occur, the pdf of the measured velocities after weighting is (using $\langle \dot{n}\,|\underline{V}\rangle = \langle \rho\,|\underline{V}\rangle c_m\dot{V}(\underline{V})$ and Eq. B.5):

$$f_{\underline{u};LDA^C} = f_{\underline{U}}\frac{\langle \rho\,|\underline{V}\rangle c_m\dot{V}(\underline{V})\dot{V}^{-1}(\underline{V})}{\langle\rho\rangle\ c_m} = f_{\underline{U}}\frac{\langle \rho\,|\underline{V}\rangle}{\langle\rho\rangle}\,, \tag{B.7}$$

which is the Favre pdf. Therefore, if transit time corrections are applied to LDA data obtained in a flow with uniform seeding density per mass (which is in principle not influenced by thermal expansion due to combustion), density weighted quantities will be obtained, i.e.:

$$\begin{aligned} \sum_{i=1}^{N} u_i tr_i \Big/ \sum_{i=1}^{N} tr_i &= \frac{\overline{\rho u}}{\overline{\rho}}\,, \\ \sum_{i=1}^{N} u_i v_i tr_i \Big/ \sum_{i=1}^{N} tr_i &= \frac{\overline{\rho uv}}{\overline{\rho}}\,, \qquad \text{etc.} \end{aligned}$$

APPENDIX C

Probability that a random variable exceeds a value within an interval

In this appendix a relation is derived for the probability that a fluctuating variable θ exceeds a value θ' within a given interval s. The variable θ has a normal distribution and is given as a function of the coordinate z. The spatial characteristics of θ are summarised by one length scale, l_θ.

Three different probabilities are considered in this section: the cdf $P_\theta(\theta')$, which gives the probability that θ has a lower value than θ', the probability $Pe_\theta(\theta', s)$, which gives the probability that θ exceeds θ' at least once during an interval s and its compliment $Pn_\theta(\theta', s)$.

For very small intervals, $s \ll l_\theta$, the probability $Pn_\theta(\theta', s)$ is equal to $P_\theta(\theta')$. This means that

$$P_{e\theta}(\theta', 0) = 1 - Pn_\theta(\theta', 0) = 1 - P_\theta(\theta') \ . \tag{C.1}$$

For larger values of s, the probability will increase, going to one for s going to infinity. To derive an analytical expression, it is useful to consider the probability that θ does *not* exceed a certain value θ'. This complementary function, $Pn_\theta = 1 - Pe_\theta$, decreases with a rate depending on how often θ exceeds θ'. Denoting this density (average number of times that $\theta > \theta'$ per length) with f_θ, the differential equation for Pn_θ is:

$$Pn_\theta(\theta', s + ds) = Pn_\theta(\theta', s)\,(1 - f_\theta ds) \ . \tag{C.2}$$

The solution to this equation is

$$Pn_\theta(\theta', s) = Pn_\theta(\theta', 0)\exp(-fs) \ , \tag{C.3}$$

which yields

$$Pe_\theta(\theta', s) = 1 - (1 - Pe_\theta(\theta', 0))\exp(-fx) = 1 - P_\theta(\theta')\exp(-fx) \ . \tag{C.4}$$

The density f is expected to be proportional to $1 - P_\theta(\theta')$ and inversely proportional to the length scale:

$$f \propto \frac{1 - P_\theta(\theta')}{l_\theta} \ . \tag{C.5}$$

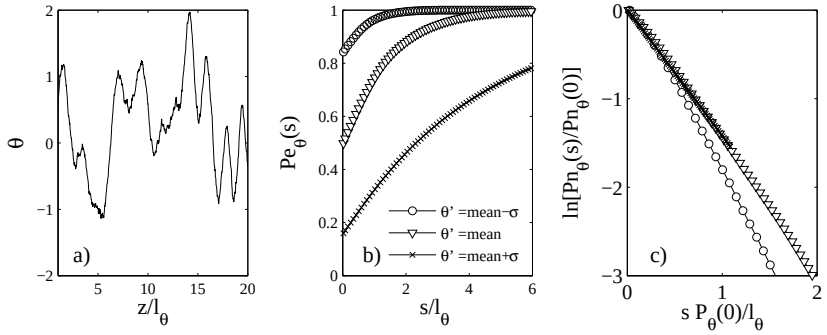

Figure C.1: A sample of the created signal(a), the results for $Pe(\theta')$ (b) and for $Pn(\theta')$ (c), for three different values of θ'.

Given this assumption, the solution is:

$$Pe_\theta(\theta', s) = 1 - P_\theta(\theta') \exp\left(-ks\frac{1 - P_\theta(\theta')}{l_\theta}\right) \ . \tag{C.6}$$

This result can be reformulated as

$$\ln\left(\frac{Pn_\theta(\theta', s)}{P_\theta(\theta')}\right) = -k\frac{s}{l_\theta}\left(1 - P_\theta(\theta')\right) \ , \tag{C.7}$$

which is a convenient expression for plotting purposes. Equation C.6 was tested numerically. The random, correlated signal of θ is created by filtering white noise with a Gaussian kernel. Note that the resulting signal has an autocorrelation proportional to that of the kernel itself [127], which in this case is a Gaussian. The power spectral density is therefore also Gaussian, by the convolution theorem.

The results, expressed according to Eqs. C.7, are shown in Fig. C.1c. The width of the kernel (full width at half maximum, FWHM) is chosen as a representative length scale l_θ. For this random variable, and for $\theta > \overline{\theta}$, the constant k has a value of approximately 1.5.

BIBLIOGRAPHY

[1] Angus Maddison. *The world economy: a millennial perspective*. OECD, 2006.

[2] EIA. Annual energy review 2009. Technical report, U.S. Energy Information Administration, *www.eia.gov/totalenergy/data/annual/*.

[3] EIA. International energy outlook 2010. Technical report, U.S. Energy Information Administration, *www.eia.gov/oiaf/ieo/index.html*.

[4] Shahriar Shafiee and Erkan Topal. When will fossil fuel reserves be diminished? *Energy Policy*, 37(1):181 – 189, 2009.

[5] Innovationsbeirat der Landesreg. (Hrsg.). *Zukunft der Energieversorgung*. Springer-Verlag GmbH, 2003.

[6] D.J.C MacKay. *Sustainable energy - without the hot air*. UIT Cambridge, 2009.

[7] S. Arrhenius. On the influence of carbonic acid in the air upon the temperature of the ground. *London Edinburgh Dublin Philos. Mag. J. Sci.*, 41:237–276, 1896.

[8] J.G. Charney. Carbon dioxide and climate: A scientific assessment. National Academy of Sciences, 1979.

[9] IPCC. IPCC fourth assessment report: Climate change 2007 (AR4), 2007.

[10] IEA. CO2 emissions from fuel combustion, highlights. Technical report, International Energy Agency, *http://www.iea.org/co2highlights/CO2highlights.pdf*, 2011.

[11] J. A. Wünning and J. G. Wünning. Flameless oxidation to reduce thermal NO-formation. *Prog. Energy Combust. Sci.*, 23(1):81–94, 1997.

[12] W.G. Wünning. Flox ®- Flameless combustion. In *Thermprocess Symposium*, 2003.

[13] H. Tsuji, A.K. Gupta, T. Hasegawa, M. Katsuki, K. Kishimoto, and M. Morita. *High temperature air combustion*. CRC Press, 2003.

[14] I. B. Ozdemir and N. Peters. Characteristics of the reaction zone in a combustor operating at mild combustion. *Exp. Fluids*, 30(6):683–695, 2001.

[15] T. Plessing, N. Peters, and J. G. Wunning. Laseroptical investigation of highly preheated combustion with strong exhaust gas recirculation. *Proc. Combust. Inst.*, 27:3197–3204, 1998.

[16] R. Weber, J. P. Smart, and W. von der Kamp. On the (mild) combustion of gaseous, liquid, and solid fuels in high temperature preheated air. *Proc. Combust. Inst.*, 30:2623–2629, 2005.

[17] D. Tabacco, C. Innarella, and C. Bruno. Theoretical and numerical investigation on flameless combustion. *Combust. Sci. Technol.*, 174(7):1–35, 2002.

[18] J.G. Wünning. *Flammlose Oxidation von Brennstoff*. PhD thesis, RWTH Aachen, 1996.

[19] B. B. Dally, A. N. Karpetis, and R. S. Barlow. Structure of turbulent non-premixed jet flames in a diluted hot coflow. *Proc. Combust. Inst.*, 29:1147–1154, 2002.

[20] R. Cabra, T. Myhrvold, J. Y. Chen, R. W. Dibble, A. N. Karpetis, and R. S. Barlow. Simultaneous laser Raman-Rayleigh-LIF measurements and numerical modeling results of a lifted turbulent H2/N2 jet flame in a vitiated coflow. *Proc. Combust. Inst.*, 29:1881–1888, 2002.

[21] C. N. Markides and E. Mastorakos. An experimental study of hydrogen autoignition in a turbulent co-flow of heated air. *Proc. Combust. Inst.*, 30:883–891, 2005.

[22] C.K. Law. *Combustion physics*. Cambridge University Press, 2006.

[23] T. Poinsot and D. Veynante. *Theoretical and numerical combustion*. Edwards, 2005.

[24] M. Oberlack, R. Arlitt, and N. Peters. On stochastic damkohler number variations in a homogeneous flow reactor. *Combust. Theor. Model.*, 4(4):495–509, 2000.

[25] A. Cavaliere and M. de Joannon. Mild combustion. *Prog. Energy Combust. Sci.*, 30(4):329–366, 2004.

[26] P. R. Medwell, P. A. M. Kalt, and B. B. Dally. Simultaneous imaging of OH, formaldehyde, and temperature of turbulent non-premixed jet flames in a heated and diluted coflow. *Combust. Flame*, 148(1-2):48–61, 2007.

[27] Z. J. Wu, A. R. Masri, and R. W. Bilger. An experimental investigation of the turbulence structure of a lifted H-2/N-2 jet flame in a vitiated co-flow. *Flow Turbul. Combust.*, 76(1):61–81, 2006.

[28] R. L. Gordon, A. R. Masri, and E. Mastorakos. Simultaneous Rayleigh temperature, OH- and CH2O-LIF imaging of methane jets in a vitiated coflow. *Combust. Flame*, 155:181–95, 2008.

[29] R. R. Cao, S. B. Pope, and A. R. Masri. Turbulent lifted flames in a vitiated coflow investigated using joint PDF calculations. *Combust. Flame*, 142(4):438–453, 2005.

[30] F.C. Christo and B.B. Dally. Modeling turbulent reacting jets issuing into a hot and diluted coflow. *Combust. Flame*, 142(1-2):117–129, 2005.

[31] S. H. Kim, K. Y. Huh, and B. Dally. Conditional moment closure modeling of turbulent nonpremixed combustion in diluted hot coflow. *Proc. Combust. Inst.*, 30:751–757, 2005.

[32] R. L. Gordon, A. R. Masri, S. B. Pope, and G. M. Goldin. A numerical study of auto-ignition in turbulent lifted flames issuing into a vitiated co-flow. *Combust. Theor. Model.*, 11(3):351–376, 2007.

[33] P. Domingo, L. Vervisch, and D. Veynante. Large-eddy simulation of a lifted methane jet flame in a vitiated coflow. *Combust. Flame*, 152(3):415–432, 2008.

[34] S. S. Patwardhan, S. De, K. N. Lakshmisha, and B. N. Raghunandan. CMC simulations of lifted turbulent jet flame in a vitiated coflow. *Proc. Combust. Inst.*, 32:1705–1712, 2009.

[35] S. Kumar, P. J. Paul, and H. S. Mukunda. Prediction of flame liftoff height of diffusion/partially premixed jet flames and modeling of mild combustion burners. *Combust. Sci. Technol.*, 179:2219–2253, 2007.

[36] I. S. Ertesvag and B. F. Magnussen. The eddy dissipation turbulence energy cascade model. *Combust. Sci. Technol.*, 159:213–235, 2000.

[37] R. Cabra, J. Y. Chen, R. W. Dibble, A. N. Karpetis, and R. S. Barlow. Lifted methane-air jet flames in a vitiated coflow. *Combust. Flame*, 143(4):491–506, 2005.

[38] K. M. Lyons. Toward an understanding of the stabilization mechanisms of lifted turbulent jet flames: Experiments. *Prog. Energy Combust. Sci.*, 33(2):211–231, 2007.

[39] L. Vanquickenborne and A. van Tiggelen. The stabilization mechanism of lifted diffusion flames. *Combust. Flame*, 10(1):59–69, 1966.

[40] G.T. Kalghatgi. Lift-off heights and visible lengths of vertical turbulent jet diffusion flames in still air. *Combust. Sci. Technol.*, 41(1):17 – 29, 1984.

[41] J. Buckmaster. Edge-flames. *Prog. Energy Combust. Sci.*, 28(5):435–475, 2002.

[42] N. Peters and F. A. Williams. Liftoff characteristics of turbulent jet diffusion flames. *AIAA journal*, 21(3):423–429, 1983.

[43] R.C. Miake-Lye and Hammer J.A. Lifted turbulent jet flames: a stability criterion based on the jet large-scale structure. *Proc. Combust. Inst.*, 22:817–824, 1988.

[44] C. S. Yoo, R. Sankaran, and J. H. Chen. Three-dimensional direct numerical simulation of a turbulent lifted hydrogen jet flame in heated coflow: flame stabilization and structure. *J. Fluid Mech.*, 640:453–481, 2009.

[45] E. Mastorakos. Ignition of turbulent non-premixed flames. *Prog. Energy Combust. Sci.*, 35(1):57–97, 2009.

[46] M.J. Tummers and D.M. Passchier. Spectral analysis of biased LDA data. *Meas. Sci. Technol.*, 12:1641–1650, 2001.

[47] E. H. van Veen and D. Roekaerts. Thermometry for turbulent flames by coherent anti-Stokes Raman spectroscopy with simultaneous referencing to the modeless excitation profile. *Appl. Opt.*, 44(32):6995–7004, 2005.

[48] K. M. Lyons, K. A. Watson, C. D. Carter, and J. M. Donbar. Upstream islands of flame in lifted-jet partially premixed combustion. *Combust. Sci. Technol.*, 179(5):1029–1037, 2007.

[49] I. Boxx, C. Heeger, R. Gordon, B. Bohm, M. Aigner, A. Dreizler, and W. Meier. Simultaneous three-component PIV/OH-PLIF measurements of a turbulent lifted, C3H8-argon jet diffusion flame at 1.5 kHz repetition rate. *Proc. Combust. Inst.*, 32:905–912, 2009.

[50] A. R. Masri, R. Cao, S. B. Pope, and G. M. Goldin. PDF calculations of turbulent lifted flames of H-2/N-2 fuel issuing into a vitiated co-flow. *Combust. Theor. Model.*, 8(1):1–22, 2004.

[51] G. A. Richards, M. M. McMillian, R. S. Gemmen, W. A. Rogers, and S. R. Cully. Issues for low-emission, fuel-flexible power systems. *Prog. Energy Combust. Sci.*, 27(2):141–169, 2001.

[52] C. J. Montgomery, C. R. Kaplan, and E. S. Oran. The effect of coflow velocity on a lifted methane-air jet diffusion flame. *Proc. Combust. Inst.*, 27:1175–1182, 1998.

[53] E. Mastorakos, T. A. Baritaud, and T. J. Poinsot. Numerical simulations of autoignition in turbulent mixing flows. *Combust. Flame*, 109(1-2):198–223, 1997.

[54] S. Sreedhara and K. N. Lakshmisha. Autoignition in a non-premixed medium: DNS studies on the effects of three-dimensional turbulence. *Proc. Combust. Inst.*, 29:2051–2059, 2002.

[55] T. Echekki and J. H. Chen. Direct numerical simulation of autoignition in non-homogeneous hydrogen-air mixtures. *Combust. Flame*, 134(3):169–191, 2003.

[56] R. L. Gordon, A. R. Masri, and E. Mastorakos. Heat release rate as represented by [OH] x [CH2O] and its role in autoignition. *Combust. Theor. Model.*, 13(4):645–670, 2009.

[57] S.B. Pope. *Turbulent Flows*. Cambridge University Press, 2000.

[58] M. Flamme. New combustion systems for gas turbines (NGT). *Appl. Therm. Eng.*, 24(11-12):1551–1559, 2004.

[59] C. T. Bowman. Control of combustion-generated nitrogen oxide emissions: Technology driven by regulation. *Proc. Combust. Inst.*, 24:859–878, 1992.

[60] R. S. Barlow. Laser diagnostics and their interplay with computations to understand turbulent combustion. *Proc. Combust. Inst.*, 31:49–75, 2007.

[61] C. Galletti, A. Parente, and L. Tognotti. Numerical and experimental investigation of a mild combustion burner. *Combust. Flame*, 151(4):649–664, 2007.

[62] M. Mancini, P. Schwoppe, R. Weber, and S. Orsino. On mathematical modelling of flameless combustion. *Combust. Flame*, 150(1-2):54–59, 2007.

[63] M. Mortberg, W. Blasiak, and A. K. Gupta. Combustion of normal and low calorific fuels in high temperature and oxygen deficient environment. *Combust. Sci. Technol.*, 178(7):1345–1372, 2006.

[64] S. Orsino and R. Weber. Numerical simulation of combustion of natural gas with high-temperature air. *Combust. Sci. Technol.*, 170:1–34, 2001.

[65] K. N. C. Bray. The challenge of turbulent combustion. *Proc. Combust. Inst.*, 26:1–26, 1996.

[66] R. Cabra and R.W. Dibble. Berkeley VCB CH4/air site. http://www.me.berkeley.edu/cal/vcb/data/VCMAData.html.

[67] R. Cabra and R.W. Dibble. Berkeley VCB H2/N2 site. http://www.me.berkeley.edu/cal/vcb/data/VCHNData.html.

[68] E. Oldenhof, M.J. Tummers, E.H. van Veen, and D.J.E.M. Roekaerts. Ignition kernel formation and lift-off behaviour of jet-in-hot-coflow flames. *Combust. Flame*, 157(6):1167–1178, 2010.

[69] E. H. Van Veen and D. Roekaerts. On the accuracy of temperature measurements in turbulent jet diffusion flames by coherent anti-Stokes-Raman spectroscopy. *Combust. Sci. Technol.*, 175(10):1893–1914, 2003.

[70] J. Warnatz, U. Maas, and R.W. Dibble. *Combustion - Physical and Chemical Fundamentals, Modelling and Simulation, Experiments, Pollutant Formation*. Springer-Verlag GmbH, 2006.

[71] J. L. Lumley. Interpretation of time spectra measured in high-intensity shear flows. *Phys. Fluids*, 8(6):1056–1062, 1965.

[72] H. Fellouah and A. Pollard. The velocity spectra and turbulence length scale distributions in the near to intermediate regions of a round free turbulent jet. *Phys. Fluids*, 21(11):115101, 2009.

[73] W. K. George and H. J. Hussein. Locally axisymmetrical turbulence. *J. Fluid Mech.*, 233:1–23, 1991.

[74] A. Liñán and A. Crespo. Asymptotic analysis of unsteady diffusion flames for large activation-energies. *Combust. Sci. Technol.*, 14(1-3):95–117, 1976.

[75] N. Rajaratnam. *Turbulent jets*. Elsevier Scientific publishing company, Amsterdam, 1976.

[76] D. H. Han and M. G. Mungal. Direct measurement of entrainment in reacting/nonreacting turbulent jets. *Combust. Flame*, 124(3):370–386, 2001.

[77] E. Oldenhof, M.J. Tummers, E.H. van Veen, and D.J.E.M. Roekaerts. Role of entrainment in the stabilisation of jet-in-hot-coflow flames. *Combust. Flame*, 158(8):1553 – 1563, 2011.

[78] H. Zhao and N. Ladommatos. Optical diagnostics for soot and temperature measurement in diesel engines. *Prog. Energy Combust. Sci.*, 24(3):221–255, 1998.

[79] R. D. Reitz and C. J. Rutland. Development and testing of diesel-engine CFD models. *Prog. Energy Combust. Sci.*, 21(2):173–196, 1995.

[80] A. Joshi and W. Schreiber. An experimental examination of an impulsively started incompressible turbulent jet. *Exp. Fluids*, 40(1):156–160, 2006.

[81] P. Ouellette and P.G. Hill. Turbulent transient gas injections. *J. Fluid Eng.*, 122(4):743–752, 2000.

[82] N. Atassi, J. Boree, and G. Charnay. Transient-behavior of an axisymmetrical turbulent jet. *Appl. Sci. Res.*, 51(1-2):137–142, 1993.

[83] G.E. Cossali, A. Coghe, and L. Araneo. Near-field entrainment in an impulsively started turbulent gas jet. *AIAA J*, 39(6):1113–1122, 2001.

[84] J. D. Naber, D. L. Siebers, S. S. Dijulio, and C. K. Westbrook. Effects of natural-gas composition on ignition delay under diesel conditions. *Combust. Flame*, 99(2):192–200, 1994.

[85] G. Fast, D. Kuhn, A. G. Class, and U. Maas. Auto-ignition during instationary jet evolution of dimethyl ether (DME) in a high-pressure atmosphere. *Combust. Flame*, 156(1):200–213, 2009.

[86] I. Iglesias, M. Vera, A. L. Sanchez, and A. Liñán. Simulations of starting gas jets at low Mach numbers. *Phys. Fluids*, 17(3), 2005.

[87] R. P. Satti and A. K. Agrawal. Computational study of buoyancy effects in a laminar starting jet. *Int. J. Heat Fluid Flow*, 29(2):527–539, 2008.

[88] J. Hult, U. Meier, W. Meier, A. Harvey, and C. F. Kaminski. Experimental analysis of local flame extinction in a turbulent jet diffusion flame by high repetition 2-D laser techniques and multi-scalar measurements. *Proc. Combust. Inst.*, 30:701–709, 2005.

[89] D. H. Rowinski and S. B. Pope. Pdf calculations of piloted premixed jet flames. *Combust. Theor. Model.*, 15(2):245–266, 2011.

[90] R. W. Bilger. Turbulent-diffusion flames. *Annu. Rev. Fluid Mech.*, 21:101–135, 1989.

[91] A. Bennett. *Lagrangian fluid dynamics*. Cambridge University Press, 2006.

[92] J. H. Frank, P. A. M. Kalt, and R. W. Bilger. Measurements of conditional velocities in turbulent premixed flames by simultaneous OH-PLIF and PTV. *Combust. Flame*, 116(1-2):220–232, 1999.

[93] K. A. Watson, K. M. Lyons, J. M. Donbar, and C. D. Carter. Scalar and velocity field measurements in a lifted CH4-air diffusion flame. *Combust. Flame*, 117(1-2):257–271, 1999.

[94] B. Böhm, C. Heeger, I. Boxx, W. Meier, and A. Dreizler. Time-resolved conditional flow field statistics in extinguishing turbulent opposed jet flames using simultaneous highspeed PIV/OH-PLIF. *Proc. Combust. Inst.*, 32:1647–1654, 2009.

[95] A. Lutz, R. Kee, and J. Miller. Senkin: A fortran program for predicting homogeneous gas phase chemical kinetics with sensitivity analysis, report no. SAND87-8248.UC-4. Technical report, Sandia National Laboratories, 1987.

[96] G.P. Smith, D.M. Golden, M. Frenklach, N.W. Moriarty, B. Eiteneer, M. Goldenberg, C.T. Bowman, R. K. Hanson, S. Song, W.C. Gardiner, V. Lissianski, and Z. Qin. http://www.me.berkeley.edu/gri_mech/.

[97] M. Raffel, C. Willert, S. Wereley, and J. Kompenhans. *Particle Image Velocimetry*. Springer-Verlag GmbH, 2007.

[98] E. F. Hasselbrink and M. G. Mungal. Transverse jets and jet flames. part 2. velocity and OH field imaging. *J. Fluid Mech.*, 443:27–68, 2001.

[99] E. Oldenhof, M. J. Tummers, E.H. van Veen, and D.J.E.M. Roekaerts. Transient response of the Delft jet-in-hot coflow flames. *Combust. Flame*, 159(2):697 – 706, 2012.

[100] K. R. Sreenivasan. On the scaling of the turbulence energy-dissipation rate. *Phys. Fluids*, 27(5):1048–1051, 1984.

[101] J. E. Rehm and P. H. Paul. Reaction rate imaging. *Proc. Combust. Inst.*, 28:1775–1782, 2000.

[102] J. M. Donbar, J. F. Driscoll, and C. D. Carter. Reaction zone structure in turbulent nonpremixed jet flames - from CH-OH-PLIF images. *Combust. Flame*, 122(1-2):1–19, 2000.

[103] J. W. Daily. Laser induced fluorescence spectroscopy in flames. *Prog. Energy Combust. Sci.*, 23(2):133–199, 1997.

[104] V. Weber, J. Brübach, R.L. Gordon, and A. Dreizler. Pixel-based characterisation of CMOS high-speed camera systems. *Appl. Phys. B Laser Optic.*, 103:421–433, 2011.

[105] R. W. Bilger. Reaction-rates in diffusion flames. *Combust. Flame*, 30(3):277–284, 1977.

[106] K.A. Buch and W.J.A. Dahm. Experimental study of the fine-scale structure of conserved scalar mixing in turbulent shear flows. part 2. *J. Fluid Mech.*, 364:1–29, 1998.

[107] C. D. Richards and W. M. Pitts. Global density effects on the self-preservation behavior of turbulent free jets. *J. Fluid Mech.*, 254:417–435, 1993.

[108] R. W. Bilger. Structure of diffusion flames. *Combust. Sci. Technol.*, 13(1-6):155–170, 1976.

[109] A. Liñán and F. A. Williams. Ignition in an unsteady mixing layer subject to strain and variable-pressure. *Combust. Flame*, 95(1-2):31–46, 1993.

[110] G.K. Batchelor. *An introduction to fluid dynamics*. Cambridge University Press, 2000.

[111] P.A. Davidson. *Turbulence: An Introduction for Scientists and Engineers*. Oxford University Press, 2004.

[112] P.S. Kothnur, M.S. Tsurikov, N.T. Clemens, J.M. Donbar, and C.D. Carter. Planar imaging of ch, oh, and velocity in turbulent non-premixed jet flames. *Proc. Combust. Inst.*, 29(2):1921 – 1927, 2002.

[113] B.F. Magnussen and B.H. Hjertager. On mathematical modeling of turbulent combustion with special emphasis on soot formation and combustion. *Proc. Combust. Inst.*, 16(1):719 – 729, 1977.

[114] B. Danon, E.-S. Cho, W. de Jong, and D.J.E.M. Roekaerts. Numerical investigation of burner positioning effects in a multi-burner flameless combustion furnace. *Appl. Therm. Eng.*, 31(17-18):3885 – 3896, 2011.

[115] S. Corrsin and A.L. Kistler. The free-stream boundaries of turbulent flows. Technical report, NACA report 1244, 1955.

[116] M.K. Cho, J. R. Chung. A k-epsilon-gamma equation turbulence model. *J. Fluid Mech.*, 237:301–322, 1992.

[117] S. B. Pope. Pdf methods for turbulent reactive flows. *Prog. Energy Combust. Sci.*, 11(2):119–192, 1985.

[118] A. Y. Klimenko and R. W. Bilger. Conditional moment closure for turbulent combustion. *Prog. Energy Combust. Sci.*, 25(6):595–687, 1999.

[119] D. Higdon. *Quantitative Methods for Current Environmental Issues*, chapter Space and space-time modeling using process convolutions, pages 37–56. Springer-Verlag GmbH, 2002.

[120] A. De, E. Oldenhof, P. Sathiah, and D.J.E.M. Roekaerts. Numerical simulation of Delft-jet-in-hot-coflow (DJHC) flames using the Eddy Dissipation Concept model for turbulence-chemistry interaction. *Flow Turbul. Combust.*, 87:537–567, 2011.

[121] F. P. Ricou and D. B. Spalding. Measurements of entrainment by axisymmetrical turbulent jets. *J. Fluid Mech.*, 11(1):21–32, 1961.

[122] E. S. Cho, B. Danon, W. de Jong, and D. J. E. M. Roekaerts. Behavior of a 300kwth regenerative multi-burner flameless oxidation furnace. *Applied Energy*, 2011.

[123] D.K. McLaughlin and W.G. Tiederman. Biasing correction for individual realization of laser anemometer measurements in turbulent flows. *Phys. Fluids*, 16(12):2082–2088, 1973.

[124] L. P. Goss, D. D. Trump, and W. M. Roquemore. Combined CARS-LDA instrument for simultaneous temperature and velocity-measurements. *Exp. Fluids*, 6(3):189–198, 1988.

[125] M. J. Tummers, E. H. van Veen, N. George, R. Rodink, and K. Hanjalic. Measurement of velocity-temperature correlations in a turbulent diffusion flame. *Exp. Fluids*, 37(3):364–374, 2004.

[126] W. Hoesel and W. Rodi. New biasing elimination method for laser-doppler velocimeter counter processing. *Rev. Sci. Instrum.*, 48(7):910–919, 1977.

[127] Julius O. Smith. *Spectral Audio Signal Processing, October 2008 Draft*. http://ccrma.stanford.edu/~jos/sasp/, accessed Oct 15 2011. Online book.

DANKWOORD

Met veel plezier kijk ik terug op mijn promotietijd in Delft, een intensieve, leerzame en plezierige periode. Daarvoor ben ik veel mensen dank verschuldigd.

Ten eerste aan mijn promotor, Dirk Roekaerts. Ik was erg enthousiast om onderzoek op het gebied van turbulente verbranding te gaan doen, maar veel kennis over het onderwerp had ik aanvankelijk nog niet. Dirk, bedankt voor het vertrouwen dat ik gekregen heb, en ook voor de vrijheid om het onderzoek zelf in te richten en te sturen. Zo'n mogelijkheid krijg je werkelijk alleen tijdens een promotieonderzoek, wanneer je geluk hebt.

Wanneer het even niet liep, of wanneer ik de behoefte had om even samen met iemand hardop na te denken kon ik altijd terecht bij Mark Tummers. Mark, je praktische instelling en kritische blik waren van grote waarde. Daarnaast bedankt voor het nauwgezet doorspitten van vele lappen tekst, die na jouw redactionele arbeid altijd een stuk helderder uit de verf kwamen.

Eric van Veen wil ik bedanken voor het uitvoeren en verwerken van de CARS-metingen: zonder de temperatuurdata was het onderzoek niet ver gekomen. Met de wispelturigheid van de seeder-laser, de kuren met de traversering (of zijn bestuurder) was het geen eenvoudige taak, we hebben aardig wat uren gemeten in de kelder. Uiteindelijk hebben we de metingen er toch maar mooi doorheen gekregen.

Dankzij Bart Hoek en Piet Verhagen was er daadwerkelijk een brander om metingen aan te verrichten. Bart, je hebt voor veel praktische oplossingen gezorgd, en mij waarschijnlijk voor veel impraktische oplossingen behoed. Piet wil ik bedanken voor zijn vakwerk, en voor het mij bijbrengen van enkele kneepjes van het vak. Met mijn kennis over het verschil tussen een Phillips en Pozidriv® schroef heb ik reeds bij meerdere mensen bewondering geoogst, om van het kunnen tappen van schroefdraad maar niet te spreken.

Erwin de Beus is met zijn Linux- én elektronica-expertise voor zo'n beetje iedere gepromoveerde van MSP onmisbaar geweest, of deze nu numeriek of experimenteel werk verrichtte. Bij heel veel klussen en klusjes heb je geholpen, de meetopstelling voor de transiente experimenten was zonder jouw hulp al helemaal niet tot stand gekomen.

Harm Jonker wil ik bedanken voor de plezierige samenwerking bij het vak "Chaotic processes". Zowel het vak zelf als de manier waarop jij het doceerde waren echt inspirerend.

Maarten van Reeuwijk verdient mijn bijzondere dank. Maarten, jij hebt in grote mate bijgedragen aan mijn keuze om aan een promotie te beginnen, een keuze die mij beroepsmatig op het goede terrein heeft gebracht. Het enthousiasme waarmee jij wetenschap uitoefent en jouw vermogen om dat enthousiasme over te brengen zijn geweldig. Dat je me met squash net iets te vaak hebt ingemaakt reken ik je dan ook niet persoonlijk aan.

Joyce en Angela, bedankt voor jullie daadkrachtige hulp met administratieve zaken. Jos, het door jou en Erwin opgezette PIV-verwerkingssysteem maakte voor mij een experimentele eindsprint mogelijk. Ashoke and Pratap, I thank you both for your work on modelling the flames. Thijs, de nachtelijke koffie/matlabsessies tegen het eind van jouw

promotie hebben mijn circadiane ritme geen goed gedaan, maar hebben in veel matlabcode geresulteerd. Remco, ik ben door jou aardig wat goede muziek en een interesse op duurzaam energie-gebied rijker. Mike, thanks for the discussions on flames, stochastic particles and other interesting things. Steef, I remember some good bebop visits, they are sorely missed! Hugo and Luis, I wish you the best of luck with finishing your research. Christof and Rob, thanks for your great efforts with the measurements we did in Darmstadt.

Dit proefschrift is voor een groot deel onder invloed van overmatige koffieconsumptie tot stand gekomen. Deze consumptie gebeurde aan de Lorentzweg altijd in goed gezelschap. Daarvoor dank aan een grote groep medewerkers en afstudeerders.

The period of finishing the thesis has had more overlap with my time in Stuttgart than originally anticipated. I thank my colleagues at ITLR for the pleasant times during and after work.

Hoewel soms wat marginaal, is er ook als promovendus nog een leven buiten de universiteit. Joke, dank je voor je liefde, en dat je me regelmatig uit mijn onderzoeksgedachtenwereldje gesleurd hebt. Maar ook voor je tekstueel advies, en natuurlijk het ontwerp van de omslag!

Als laatste wil ik mijn ouders bedanken voor hun steun en aansporing, tijdens de promotietijd, en tijdens alles wat er aan vooraf ging.

LIST OF JOURNAL PUBLICATIONS

E. OLDENHOF, M.J. TUMMERS, E.H. VAN VEEN, AND D.J.E.M. ROEKAERTS. Conditional velocity statistics in jet-in-hot-coflow flames, *Submitted to Combust. Flame*.

E. OLDENHOF, M.J. TUMMERS, E.H. VAN VEEN, AND D.J.E.M. ROEKAERTS. Transient response of the Delft jet-in-hot-coflow flames, *Combust. Flame*, **159**(2):697–7061, 2012.

A. DE, E. OLDENHOF, P. SATHIAH, AND D.J.E.M. ROEKAERTS. Numerical simulation of Delft-jet-in-hot-coflow (DJHC) flames using the Eddy Dissipation Concept model for turbulence-chemistry interaction, *Flow Turbul. Combust.*, **87**:537–567, 2011.

E. OLDENHOF, M.J. TUMMERS, E.H. VAN VEEN, AND D.J.E.M. ROEKAERTS. Role of entrainment in the stabilisation of jet-in-hot-coflow flames, *Combust. Flame*, **158**(8):1553–1563, 2011.

E. OLDENHOF, M.J. TUMMERS, E.H. VAN VEEN, AND D.J.E.M. ROEKAERTS. Ignition kernel formation and lift-off behaviour of jet-in-hot-coflow flames, *Combust. Flame*, **157**(6):1167–1178, 2010.

About the author

Ernst Oldenhof, born 10 November 1977, Rotterdam

1990 – 1996	Marnix Gymnasium Rotterdam
1996 – 1997	Student, social geography, University of Utrecht
1997– 2004	Student, civil engineering, Delft University of Technology (MSc.)
2004– 2005	Structural / R&D engineer, Huisman ITREC, Schiedam
2006 – 2010	PhD student, department of Multi-scale physics, faculty Applied Physics, Delft University of Technology
2010	Post-doctoral researcher, department of Multi-scale physics, faculty Applied Physics, Delft University of Technology
2010 – present	Post-doctoral researcher, Institut für Thermodynamik der Luft- und Raumfahrt, Universität Stuttgart